Dissertation
submitted to the
Combined Faculties for the Natural Sciences and for
Mathematics
of the Ruperto-Carola University of Heidelberg,
Germany
for the degree of
Doctor of Natural Sciences

presented by
Oliver Zahn
born in Munich

.

Illuminating the Universe: New Probes of Reionization and Cosmology

Referees: Prof. Dr. Matthias Bartelmann
Prof. Dr. Matias Zaldarriaga (Harvard)

.

Zusammenfassung: Wir modellieren die Epoche der Reionisation des Universums, mittels analytischer und numerischer Methoden. In einer detailierten Analyse unserer Ergebnisse stellen wir eine gute Übereinstimmung zwischen den alternativen Beschreibungen der Morphologie der ionisierten Gebiete fest. Wir verwenden unsere Simulationen, um Vorhersagen fuer Beobachtungsgrößen aufzustellen, die innerhalb weniger Jahre zur Verfügung stehen sollten: der kinetische Sunyaev-Zel'dovich Effekt und Schwankungen in der 21 cm Strahlung aufgrund der Hyperfeinstruktur des neutralen Wasserstoffes. Wir schlagen auch vor, die 21 cm Strahlung zur Einschränkung kosmologischer Parameter (mittels Bestimmung des Materie-Leistungsspektrums) zu verwenden. Desweiteren benützen wir diese Observable als Hintergrund für den Gravitationslinseneffekt aufgrund großskaliger Strukturen im Universum, und entwickeln einen Formalismus, um die Linsenverteilung aus den charakteristischen Eigenschaften des beobachteten 21 cm Feldes zu rekonstruieren.

Abstract: We model the epoch of hydrogen reionisation of the universe, using analytic as well as numerical methods. In a detailed statistical analysis of our results, we find good agreement in the alternative descriptions of the morphology of ionized regions. We use the simulations to make predictions for reionisation observables that should be accessible within a few years years: the kinetic Sunyaev-Zel'dovich effect and fluctuations in the 21 cm spin flip transition of neutral hydrogen. We also propose to use the 21 cm signal to constrain cosmological parameters by probing the matter power spectrum. We also make use of the observable as s source screen for gravitational lensing by large scale structure, and develop a formalism to extract the lens distribution from the characteristics of the lensed 21 cm field.

Chapter 1

Introduction

Within less than two decades, cosmology has progressed from a rather speculative science to one of the most successful fields of physics, through being based on an exemplary interplay between experiment and theory. The measurement of fluctuations at the level of 10^{-5} in the cosmic microwave background (CMB) (e.g. [1, 2, 3]) has suggested a 'standard model' that has stood up against a number of other observations based on independent physics. The challenge of the dawning cosmological paradigm is that it is fundamentally puzzling, and comes with the calling to develop new parts for our scientific toolbox: to explain the fact that the universe looks the same on average in all directions, we need to invoke an epoch of superluminal expansion ('inflation') following the big bang [4, 5]; to understand the haze through which we see the primordial CMB [6, 7], the absorption pattern of emission lines from distant luminous quasars (e.g. [8]), as well as other observations, the epoch of reionization of the universe has to have been more complex than simple models require; to do justice to the observed luminosity-distance relationship of distant Supernovae Ia [9, 10], the clustering of galaxies (e.g. [11, 12], and further observables, one has to postulate a contribution of roughly 75% of negatively gravitating 'dark energy' to the total energy budget of the present universe. Addressing these puzzles directly will require fundamentally new ideas and specifically designed observations, to try to give us more insight into their nature.

This thesis introduces a number of new ways of cosmological exploration. Its central topic, the epoch of reionization (EoR), is a pivotal stage in the process of cosmological structure formation, marking the birth of the first luminous objects, a key landmark as the universe transforms from the relatively smooth state probed by the cosmic microwave background (CMB), to its present day complexity.

First we will establish more accurate predictions for the ionized regions of hydrogen (HII) produced by the first radiative sources. We will achieve this goal in two different ways, using numerical simulations, as well as modeling based on analytic considerations. The close agreement we find between both methodologies gives us confidence that we are beginning to understand the complex physical processes guiding the EoR.

A second goal of this thesis will be to use the models we develop to make concrete predictions for observables that will likely become important probes of the reionization process within the next few years. Current observational constraints on the EoR offer an incomplete picture. They come from Lyα forest absorption spectra towards high redshift quasars (e.g. [8]), from measurements of the high redshift galaxy luminosity function from narrow-band Lyα-emission searches [13], and from measurements of the large scale CMB E-mode polarization [7, 14]. The claimed size of HII regions surrounding individual quasars has also been used to infer limits on the neutral fraction [15]. There has also been an interpretation of the relatively high temperature of the Lyα forest at $z \simeq 2 - 4$ as evidence of an order unity change in the ionized fraction at $z < 10$ [16, 17], although this depends on the properties of He II reionization [18].

While valuable, each of these observational probes has its limitations, and some of the current constraints are relatively meager. Quasar absorption spectra are limited in part by the high Lyα absorption cross section: by $z \sim 6$, even a highly ionized IGM completely absorbs quasar flux in the Lyα forest. The constraints from narrow-band Lyα searches are subtle to interpret (e.g. [19]), and restricted to narrow redshift windows around $z = 5.7$ and $z = 6.5$, where Lyα falls in the observed optical band, and avoids contamination from bright sky lines (e.g. [20]). These observations do not currently allow the interpretation that the ionization state of the IGM is evolving between these windows. The CMB polarization measurements constrain only an integral over the ionization history, and are potentially sensitive to polarized foreground contamination [7].

The study of the EoR may be revolutionized by experiments aimed at detecting 21 cm emission from the high redshift IGM when the phase transition between neutral and ionized occurred. These experiments should provide three-dimensional information regarding the distribution of high redshift neutral hydrogen (HI), constraining the topology of reionization, and its redshift evolution (e.g. [21, 22]). Several low frequency radio telescopes are presently ramping up to detect this signal: the Mileura Wide Field Array (MWA) [1], the PrimeavAl Structure Telescope (PAST), and the Low Frequency Array

---

[1] http://web.haystack.mit.edu/arrays/MWA/

(LOFAR) [2], while another second generation experiment, the Square Kilometer Array (SKA)[3], is in the planning stage. These measurements will be dominated by foreground contamination, but in contrast to the IGM signal, the foregrounds are expected to be smooth in frequency, facilitating their removal [22]. One of our goals in this thesis will be to establish accurate predictions for the 21 cm signal to be expected in these observations.

A different new generation of cosmology experiments is being constructed to target the so-called 'secondary anisotropies' (SA) in the CMB. Its 'primary anisotropy' was created 380,000 years after the Big Bang, when the universe was just 0.1% of its present size. When it had cooled down enough so that most of its atoms had become neutral, it became transparent to the CMB photons while expanding by a large factor. There are two extensively studied ways in which this primordial pattern can get altered: 1) relativistic bending of light rays caused by massive structures such as clusters of galaxies (gravitational lensing); and 2) scattering off hot gas inside dense regions changes the primordial spectrum and Doppler-shifts the photons into the line of sight depending on the motion of the gas (the thermal and kinetic Sunyaev-Zel'dovich (SZ) effects respectively). In this thesis we will predict a third way: regions of ionized gas during the epoch when the first radiative sources were created led to inhomogeneous re-scatterings of the CMB photons.

We will make predictions for how well the upcoming CMB experiments will be able to distinguish different reionization scenarios. In order to do so, we also need an accurate model for the signal component from the nearby universe. Because this contains high density peaks, the $z < 3$ signal turns out to be very large and dominates the overall signal (we will find this component to make up 70-90% of the total). To model this accurately we resort to large volume high resolution gas-dynamical simulations to model the kinetic SZ effect. We will also use our simulations to calculate the thermal component of the effect, which vanishes at 218 GHz, and can be subtracted by multi-frequency fitting.

We will largely assume familiarity of the reader with the basic cosmological paradigm throughout most of this work, but provide basic definitions where they seem crucial to the flow of our argument. We will assume a flat ΛCDM cosmology parameterized by contributions to the total energy density of matter Ω_m, dark energy[4] Ω_Λ, and baryons Ω_b. The local expansion rate will be parametrized by h in $H_0 = 100\,h$ km/s/Mpc, and the shape of the

---

[2] http://www.lofar.org

[3] http://www.skatelescope.org/

[4] assumed to be a cosmological constant with equation of state $w_{\rm eos} = \frac{p}{\rho} = -1$, where p is pressure, ρ is density.

primordial scalar perturbation power spectrum by its slope n_s, as well as a normalization to present day fluctuations on a comoving[5] 8 Mpc/h (Mpc) scale[6] of σ_8. The values of these parameters will be specified at the beginning of each individual chapter, each time in rough agreement with recent experimental constraints (e.g. [23]).

The detailed structure of this thesis is as follows.

Chapter 2 is divided into two parts. We will first discuss the challenges involved in modeling reionization, in Section 2.1. We will review approaches to the problem taken in the past. We will describe a model of the morphology of HII regions based on considerations reminiscent of the extended Press-Schechter/excursion set formalism that has been used to predict the fraction of collapsed objects in the universe.

In the second part of Chapter 2, we will describe the cosmological 21 cm signal from the high redshift IGM. The physics of the underlying spin-flip transition, and its evolution through different cosmological regimes, will be the topic of Section 2.2. The power spectrum of high redshift 21 cm fluctuations will be described in Section 2.3. Because it is observed in redshift space, we find that it can be used to distinguish its astrophysical components from those due to the linear density field. This means that we could improve constraints on the cosmological parameter budget substantially. We will derive cosmological parameter constraints based on planned 21 cm experiments in Section 2.3.

In Chapter 3 we will use the 21 cm signal from the early stages of reionization as a way to measure gravitational structure formation at low redshift. We will make use of the large number of data points provided by the 21 cm signal as a background for gravitational lensing by large scale structure in the universe. Lensing correlates different lines of sight in a unique way, and one can use this to statistically reconstruct the lens distribution from the observed field. We will generalize a quadratic estimator of the lensing field developed for the CMB to this three dimensional observable. We will apply this to survey areas and depths as they should be seen by conceived radio observatories with large collecting areas. We will discuss benefits and disadvantages of 21 cm lensing reconstruction in comparison with the CMB. As the 21 cm signal potentially contains orders of magnitude more information than the CMB, in theory it could be more useful for the reconstruction. In

---

[5] A comoving observer is one who experiences the expanding cosmos as homogeneous and isotropic

[6] We will employ the parsec (pc) as standard measure of cosmological distance throughout this thesis. 1 Parsec = 3.26163626 lightyears =3.08568025 × 10^{16} m. To describe the scales relevant to reionization, we will mostly be using comoving Megaparsec (Mpc)=10^6 parsec

practice the effort will be limited by costs for collecting area and antenna correlation to combat the large foregrounds.

In Chapter 4 we will first utilize the semi-analytic reionization model introduced in Chapter 2 to make predictions for the kinetic SZ effect it produces. The processes driving formation and survival of the first luminous sources are not well constrained at the moment, and we will in this Chapter account for this uncertainty by implementing two different reionization scenarios, which vary in the duration of the partially reionized phase. To gauge the relative importance of the effect of patchy reionization on the CMB, we model the traditional secondary anisotropies (SZ effects and lensing) using a large scale, high resolution cosmological simulation that models the adiabatic gas physics between redshift of reionization and today. This simulation is one of the most sophisticated simulations of the SZ effects to date. We will calculate sensitivities and make predictions for the detectability of the kinetic SZ signals with upcoming ground based CMB experiments. We will also show that neglecting reionization can lead to substantial biases in cosmological parameter constraints if derived from the Planck satellite, which through its precision will be sensitive to the small peak amplitude changes caused by the reionization signal.

In Chapter 5 we will attempt to gain deeper insight into the large scale morphology of the reionizing phase by running a large volume radiative transfer simulation. This simulation takes place in a 100 Mpc volume, representing the cosmological background in which reionization takes place. It is the reionization simulation with the largest number of resolved sources performed to date. We will scrutinize the semi-analytic reionization model introduced earlier in more quantitative detail by comparing it to the radiative transfer simulation. We will find that the analytic model predictions are surprisingly accurate, and agree remarkably well with full simulations, statistically as well as on a side-by-side basis.

With the level of precision increasing, the field of cosmology will become more sensitive to careful modeling of different observables, combining various methods available to us. Analytic models guide our intuition of the seemingly complex processes that drove the reionization of the universe. The robustness of their predictions can on the one hand be seen as confirmation of convergence of our understanding of the process. It also suggests that the methods proposed here will prove useful in future analyses of data from reionization experiments, when the challenge will be to compare a variety of possible parametrizations to the observations.

The measurement of the 21 cm and small scale CMB signals we predict in this thesis, will in the future be supplemented by further quasar absorption spectra (including clues from metal absorption lines: [20, 24]), high redshift gamma ray bursts (e.g. [25, 26]), high redshift galaxy surveys (e.g. [27]). Analyzed in combination, these measurements will provide us with a wealth of data on the EoR. The analytic and numerical models for reionization we developed, will then prove helpful to convert these data into information about the physical mechanisms underlying reionization. Cosmology is awaiting an exciting time of breaking through new frontiers of knowledge, and we hope the results presented here will be useful tools on the way.

Acknowledgments

At this point I would like to thank some of the people who have accompanied me throughout the last three years, and played, directly and indirectly, major roles in accomplishing my work.

First of all I want to thank Matias Zaldarriaga, for being the most fun to work with, and at the same time the most challenging, advisor I could have wished for. Since those months I spent as undergraduate at NYU, he encouraged me to work on quite a diverse range of topics in cosmology, and for sure my contribution to each one of them would have been much smaller without the continuous help of his intuition and knowledge. I am eagerly looking forward to my remaining months at the CfA, and hope that little Marina will let her daddy get enough sleep!

I now want to express my gratitude to Matthias Bartelmann, for the unconditional support he has given me in following my interest to go as a Visiting Fellow to Harvard and collaborate with 'the other Mat(th)ias', for almost the entire PhD phase. My time here has been very fulfilling, and perhaps the biggest drawback was that it did not allow me to interact as much with, and learn from, Matthias. My great hope is that there will be more opportunities to work together in the future.

The major reason, of course, why I did not spend more time in Germany, has not been directly science related! This is were I want to thank Breeze, my love, my wife, for the inspiration and fulfillment she has contributed on a daily basis to my life since the summer of 2004. That our 'world lines' converged, is perhaps the most lucky thing that has happened to me, and astonishingly I didn't even have to leave the CfA to have it happen!

I next want to thank Adam Lidz, for being a close and inspiring coworker. His experience with many of the topics I had just begun to work on sped up and improved my research (and the english language presentation of it!) immensely. It was a great benefit to always be able to peek through his door across the hallway, and discuss one of those stubborn questions that just wouldn't get answered by my student's brain.

I furthermore want to thank Lars Hernquist and Matt McQuinn for their involvement in the projects we worked on together so far, and their readiness to talk about science whenever I wanted to.

Finally I want to thank my parents, Elke and Jochen, for being supportive and helping me advance to this stage of my life. I hope the long distance between us, although it may continue to last for a while, will not hinder us from being close, and partake in each others lives.

Contents

Chapter 2

Reionization models and 21 cm radiation from high redshift

In this chapter we will begin by describing the difficulties encountered in the modeling of reionization. We will discuss different methodologies, including numerical modeling by radiative transfer simulations, and analytic approaches, in Section 2.1. We will introduce a model to describe the morphology of HII regions that is reminiscent of the extended Press-Schechter theory of the halo mass function. In later chapters we will expand upon the version of the model described here. We suggest a novel approach to describe the complex non-spherical clustering of HII regions likely to be expected in the real universe. This approach is based on implementing the analytic model in a Monte-Carlo way on top of realizations of the large scale cosmic web. An advantage of this implementation that we will exploit in chapter 5 to test this model, is that it allows side-by-side comparison of the analytic model with purely numerical methods of modeling reionization.

Perhaps the most promising future probe of reionization is radiation from the 21 cm spin-flip transition of neutral hydrogen in the high redshift universe. In Section 2.2 we will introduce the physics of this cosmological 21 cm signal. The brightness temperature of this line transition depends on a number of physical interactions which make it appear in emission or absorption against the CMB, depending on the epoch. These considerations will be the basis for predictions of the 21 cm power spectrum we will make based on the numerical and analytic reionization models developed in this thesis.

In Section 2.3 we will discuss properties of the 21 cm power spectrum. Redshift space distortions introduce a peculiar line-of-sight anisotropy that can be used to distinguish astrophysical contributions (due to homogeneous radiative processes) from cosmological contributions (imprinted by the linear velocity field). The sensitivity of upcoming reionization interferometers should allow us to use the pre-reionization 21 cm signal to extract cosmological parameters.

2.1 Modeling Reionization

2.1.1 The view from simulations

Simulations of reionization have a history dating back almost a decade (e.g. [28, 29, 30, 31, 32, 33, 34, 35, 36]). Many of the efforts were inspired after the WMAP collaboration announced [3], in 2003, that the total integrated optical depth due to Thomson scattering of the CMB due to reionization was about 2 times larger than previously expected, $\tau_{rei} \simeq 0.17$, corresponding in the WMAP cosmology to a reionization redshift of $z_{rei} \simeq 20$. On the other hand, extended gaps of transmission seen in the spectra of quasars at redshifts z=5.5-6.5, led to the interpretation that there is a strongly fluctuating ionization background at $z \simeq 6$ [8]. In this light the WMAP result suggested a quite complex and extended reionization scenario. This lead to a surge of theories, including interest in high redshift 'Population III' stars in leading to an early phase of reionization (e.g. [33, 37]). [1].

The reason for the early reionization claim of the first year WMAP release (WMAP-1) was a large feature found in the polarization signal on the scale of tens of degrees (in WMAP-1 this feature was only detected in cross correlation with the CMB temperature beause of its larger S/N). The theoretical motivation for this interpretation [38] is re-scattering of the primordial CMB quadrupole off free electrons created during reionization. The height and angular scale of the large scale feature reflect the Hubble scale (size of the universe) during reionization.

The large scale polarization bump was three years later (2006), with the release of the WMAP-3 analysis, understood to be to a large extent sourced by polarized foreground emission, dominated by galactic synchrotron [7]. Many of the characteristics of models developed since WMAP-1 carry over to lower redshift reionization [2].

To model reionization most accurately, we would want to use numerical simulations to incorporate effects of non-linear clustering and radiative transfer. The morphology of the ionized regions and evolution of the ionized

---

[1] These are extremely metal poor stars with a top-heavy initial mass function (IMF), which cool through molecular hydrogen. They are to be contrasted to sun-like 'Pop II'-stars with a Salpeter IMF, which cool through atomic hydrogen.

[2] and for most reionization probes, such as the 21 cm signal discussed in the next section, the redshift of reionization *needs to be lower* than z=20 to make observations feasible

fraction should also depend sensitively on the assumed source prescription. To date it is not clear what the contribution of quasars to the total ionizing flux might have been. Theoretically, this depends on the extrapolation of the observed quasar luminosity function to low luminosities, which suggests that the high redshift contribution is small [39, 40]. Another argument against the importance of quasars in reionizing the universe is that the observed soft X-ray background does not have a very large un-resolved component which one might expect if quasars reionized the IGM [41]. In what follows, we will assume that the influence of quasars to the formation of HII regions is of secondary nature.

Simulations have supported theoretical claims (e.g. [42, 43]) that reionization should be a very inhomogeneous process. In them, reionization proceeds from high to low density regions and recombinations seem to play a subdominant role to large scale bias. Strömgren spheres of neighboring protogalaxies overlap, and, as a result, overdensities harbor large ionized regions, up to tens of comoving Mpc across. Besides uncertainties over the physical approximations made in current radiative transfer calculations of reionization, memory and CPU requirements pose a serious limitation, so that these simulations have until recently only been performed on scales of up to 10 Mpc/h, corresponding to $\simeq 6$ arcminutes on the sky [44] for a typical reionization redshift of $z = 8$. If the HII regions are of comparable size (as we will show later they can indeed become several tens of comoving Mpc across), sample variance becomes a problem for these simulations. In addition, [45] showed that the halo mass function will be biased in a simulation that is normalized to the mean density of the universe on the cutoff scale of the box.

Figure 2.1 shows the result of the simulation by [44]. The radiative transfer is typically performed as a post-processing step after running a simulation of the cosmic density field, in this case a smoothed particle hydrodynamical simulation (SPH) with 324^3 particle resolution (for each dark matter and gas). Simulation snapshots are then searched for compact systems (halos), that are in turn assigned an ionizing luminosity. Then rays are cast from those sources, and propagated through the hydrogen fluctuation field given by the cosmological simulation. This procedure can quickly become very CPU and memory intensive, when we have to account for the joint influence of many thousand sources on the ionization state of many volume elements in the box. Each HII region in this simulation contains many sources, whose strong clustering makes the bubbles grow large (comparable to the box scale) quickly. We can see that the 10 Mpc/h simulation size used here, although a substantial step at the time, only allows to model the very beginning stages of the process, after which bubbles quickly merge and we are left in the dark about the actual clustering properties of the ionization field.

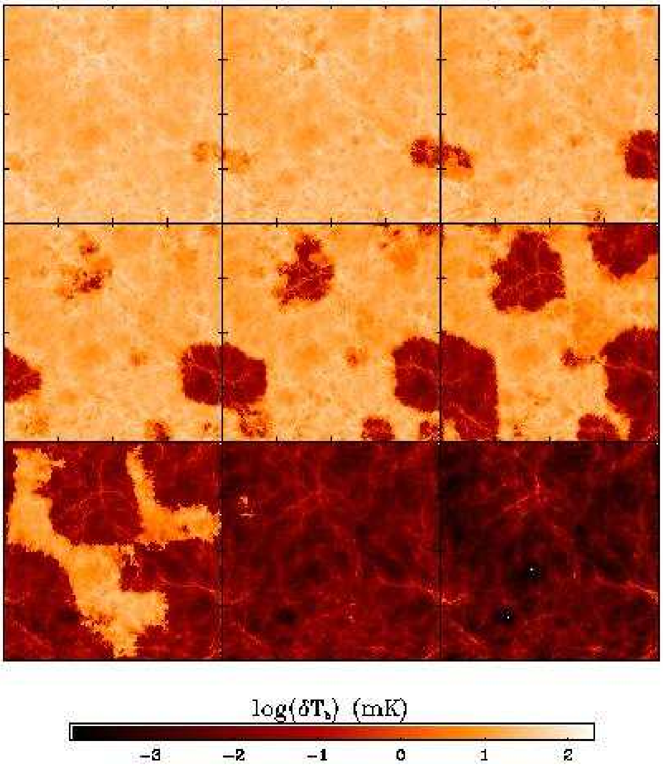

Figure 2.1 21 cm signal (see Section 2.2 resulting from a radiative transfer simulation by [44]. The comoving size of this box (shown are 9 snapshots at different evolution stages) was 10 Mpc/h on a side. We can see that already at small ionization fractions this simulation box size is insufficient to sample the bubble size distribution evenly. Permission to print granted from Aaron Sokasian.

To fully satisfy the requirements on dynamical range, we would on one hand like to reliably simulate the large scales on which bubbles occur, i.e. roughly 100 comoving Megaparsec (Mpc)[3]. On the other hand we would need to resolve the smallest dwarf galaxies potentially contributing to the reionization process. The question of what the lowest mass sources are is essentially a requirement to the temperature of virialized systems. For cooling through atomic hydrogen[4], the required temperature is about 10^4 Kelvin.

---

[3] We will justify this assertion in Chapter 5

[4] In contrast, *molecular* hydrogen cooling is the mechanism allowing very massive and metal poor high redshift stars to cool, so called Population III systems. The Lyman-Werner photons produced by these stars have a tendency to photo-dissociate the molecular

This corresponds to a virial mass of [43]

$$m_{\rm min} \simeq 3.0 \times 10^9 (1+z)^{-1.5} M_\odot \,. \tag{2.1}$$

corresponding to $10^8 M_\odot$, where $M_\odot$ is the mass of our sun, at redshifts $z = 8$. To determine the number of particles necessary to resolve this mass within a 100 Mpc simulation volume, notice that the critical density is measured [14] to be

$$\rho_{\rm crit} \simeq 10^{-29} \frac{g}{\rm cm^3} \simeq 1.4 \times 10^{17} \frac{M_\odot}{(100\,{\rm Mpc})^3} \tag{2.2}$$

To resolve the minimum mass required for atomic cooling, we therefore require

$$\frac{1.4 \times 10^{17}}{3 \times 10^6} = 4.6 \times 10^{10} \simeq 3500^3 \tag{2.3}$$

particles! This number is out of reach to the largest computer clusters we are aware of. In Chapter 5 we will try to come closer to this goal by running a simulation based on 30 times more particles, in a two orders of magnitude larger volume than the simulation described. This will allow us to model the bubble morphology in a representative volume even into the late stages of reionization, when the bubbles become very large. Our simulation will still fall short of the above mentioned resolution goal, however we will argue for why its minimum mass is sufficient to simulate the large scale morphology of reionization.

Even if the dynamical range requirements in a simulation of reionization were fulfilled, there would still be a large uncertainty in many of the input parameters of these simulations. Even within the paradigm of reionization by Population II hosting galaxies, the prescriptions used for the star formation efficiency, the escape fraction, the number of photons emitted on average per baryon, and the number of recombinations encountered, are at present all uncertain by at least an order of magnitude.

2.1.2 Analytic Modeling

In the light of these difficulties, it would be helpful if we could come up with an analytic prescription to guide our intuition for the ways in which the reionization morphology depends on a number of parameters. If found

---

hydrogen they need for their cooling. It is a matter of present debate whether this negative feedback makes Pop III stars a realistic possibility. In most of this thesis we will assume Pop II stars, although the models we develop can also be applied for Pop III hosting halos, see Chapter 4.

successful, such models would be useful because of their larger dynamical range, making them less prone to the resolution problems of the simulations.

The most important ingredients for a model of reionization are the number density of sources as a function of mass, their clustering strength, and their correlation with the underlying density field. Because HII regions extend to larger radii than the correlation length of individual galaxies, building an analytic model purely from first principles based on local galaxy properties can only succeed before clustering beomes important[46]. A straightforward generalization is then to assume that HII regions trace dark matter halos but to include source clustering in an approximate way. One possibility is to specify the global neutral fraction $\bar{x}_i(z)$ and the characteristic bubble size $R_{\text{char}}(z)$. The number density of bubbles $n_b(m)$ does then follow automatically, and the bubbles can be associated with dark matter halos of the same number density [47]. This allows the model to make use of the well established halo-clustering formalism [48] to describe the bubble pattern, however it requires $R_{\text{char}}(z)$ to be arbitrarily specified.

It would be more satisfying to motivate $R_{\text{char}}(z)$ physically. The central quantity is the clustering of reionization sources so that overdense regions, which harbor more sources, will be ionized before underdense regions [43] [5] .

Let us begin by associating an HII region with a single galaxy. The size distribution of ionized regions then follows directly from the halo mass function when the ansatz $m_{\text{ion}} = \zeta m_{\text{gal}}$ is made, where m_{gal} is the mass in a collapsed object. The parameter ζ is the efficiency factor for ionization, for example composed as $\zeta = f_{\text{esc}} f_* N_{\gamma/b} n_{\text{rec}}^{-1}$, where f_{esc} is the escape fraction of ionizing photons from the object, f_* is the star formation efficiency, $N_{\gamma/b}$ the number of ionizing photons produced per baryon by stars, and n_{rec} is the typical number of times a hydrogen atom has recombined. The efficiency factor is a rough combination of uncertain source properties, but encapsulating a variety of reionization scenarios in it can be regarded as a starting point to gain insights into the morphological properties of the partly ionized phase.

According to the extended Press-Schechter model [49], the collapsed fraction (or the fraction of baryons that lie in galaxies) in a region of size r depends on the mean overdensity of that region, $\overline{\delta}_r$, as

$$f_{\text{coll}}(m_{\text{min}}) = \text{erfc}\left[\frac{\delta_c(z) - \overline{\delta}_r}{\sqrt{2[\sigma^2(r_{\text{min}}) - \sigma^2(r)]}}\right] . \tag{2.4}$$

Here, $\sigma^2(r)$ is the linear theory rms fluctuation on scale r and r_{min} is taken to

---

[5] A scenario in which the higher level of clumpiness associated with the overdense regions completely reverses this trend [42], leading to ‘outside-in’ reionization, can not be confirmed in present reionization modeling

be the radius that encloses the mass $\mathrm{m}_{\min}$ (at average density $\overline{\rho}$) corresponding to a virial temperature of 10^4K, at which atomic hydrogen line cooling becomes efficient and $\delta_c(z)$ is the numerical factor 1.686 scaled to today using linear theory. The redshift dependence of the minimum mass is given by Equation 2.1. The fraction of mass in galaxies required to ionize all hydrogen atoms is inversely proportional to the ionizing efficiency, so one requires that

$$f_{\mathrm{coll}} \geq \zeta^{-1} \, . \tag{2.5}$$

Combining equations 2.4 and 2.5, we can define a barrier which fluctuations have to cross for their baryonic content to become ionized [50]

$$\delta_r \geq \delta_x(m,z) \equiv \delta_c(z) - \sqrt{2}\, \mathrm{erfc}^{-1}(\zeta^{-1})[\sigma^2(r_{\min}) - \sigma^2(r)]^{1/2} \, . \tag{2.6}$$

Because Press-Schechter theory assumes Gaussian fluctuations on the mass scale m, this formalism can be applied only to mass scales larger than the size of individual collapsed objects.

Let us try to compute the size-distribution of HII regions fulfilling the above condition, as a function of mass. We cannot treat each HII bubble in isolation, because even if a region does itself not contain many sources, it might receive ionizing radiation from sources outside of it. In combination the incident radiation could - especially if the region is a low density part of the universe - lead to reionization. This consideration is reminiscent of the excursion set formalism [49, 51], which was used to derive the Press-Schechter [52] mass function. In that case the critical overdensity $\delta_c(z)$ describes a condition for virialization. Any region with $\delta > \delta_c(z)$ is assigned to be part of a halo. The Press-Schechter formalism suffers from a problem similar to our problem of a region anemic of ionizing sources. There is has been called the “cloud-in-cloud” problem, meaning that a point can be part of many regions with $\delta > \delta_c(z)$ on different mass scales. For halos, as for HII regions, only the largest scale is physically important, because it incorporates all of the smaller scales. The excursion set formalism treats this as a diffusion problem in the ($\sigma^2(m)$, δ) space with an *absorbing barrier* ($\delta_c(z)$). As the rms density fluctuation increases monotonically toward smaller scales, σ^2 plays the role of time, while δ plays the role of space. One can use this as a basis to compute the distribution of crossing times, or masses, from which the halo mass function follows. The cloud-in-cloud problem is solved by following trajectories from large to small mass scales, or increased $\sigma^2(m)$, while assigning each diffusion trajectory to the largest halo (‘absorbing’ smaller ones) which it is embedded in.

The problem of finding the mass function of HII regions is only different from the problem of finding the halo mass function in that, instead of being a constant, the absorbing barrier δ_x follows from the condition $f_{\rm coll}(\delta, \sigma(m)) = \zeta^{-1}$, i.e. it is a function of mass. As can be guessed from Figure 2.3, the ionization barrier can however be approximated by a linear function in σ^2, $\delta_x(\sigma^2) \approx B(\sigma^2) \equiv B_0 + B_1\sigma^2$, which allows us to find an analytic solution for the 'bubble mass function' [53, 50, 54]

$$m\, n_b(m)\, dm = \sqrt{\frac{2}{\pi}}\, \frac{\bar{\rho}}{m} \left| \frac{d\ln\sigma}{d\ln m} \right| \frac{B_0}{\sigma(m)} \exp\left[-\frac{B^2(m,z)}{2\sigma^2(m)} \right] dm. \tag{2.7}$$

As a convenient result of this, many of the tools used for halo mass functions, clustering, etc. can be carried over to HII regions.

The solid curves in the left panel of Figure 2.2 show the size distribution following from Equation 2.7 for different $\bar{x}_i$ at $z = 18 - 12$. The ordinate is the fraction of the ionized volume filled by bubbles of a given size. The model suggests that bubbles grow large toward the middle stages of reionization, with characteristic sizes exceeding 10 Mpc/h during the middle and final stages. It would be satisfying if we could confirm this picture with numerical simulations of reionization performed on an appropriate scale (as we will do in Chapter 5).

The right panel of Figure 2.2 shows the evolution of the global ionized fraction of the IGM, $\zeta f_{\rm coll}$ in the analytic model, for three different values of the ionization efficiency.

Note that we have only incorporated homogeneous recombinations as a background into the overall efficiency parameter ζ (the intrinsic photon output of the sources being largely unknown). In reality, dense systems, such Lyman-limit systems or minihalos (if these survive the photo-ionizing background inside the first HII regions) might play an important contributing role. A property of those systems would be that the larger the bubble they reside in, in other words the higher the photoionizing background, the deeper photons penetrate into them, and the higher the resulting recombination rate becomes. Because these photons are lost to reionizations and to further growth of the bubble, at some point a saturation will be reached, at which the total photon output of sources just cancels with recombinations, and the bubble growth could be effectively stalled. Given a prescription of the small scale density structure of the IGM (e.g. calibrated off simulations), this scenario can be incorporated in analytic models [55] [6]

---

[6] We are currently actively working on including recombinations in the semi-analytic scheme proposed in the next section, validating them against simulations, and using our generalizations of the model to efficiently explore the degeneracies in reionization parameter space.

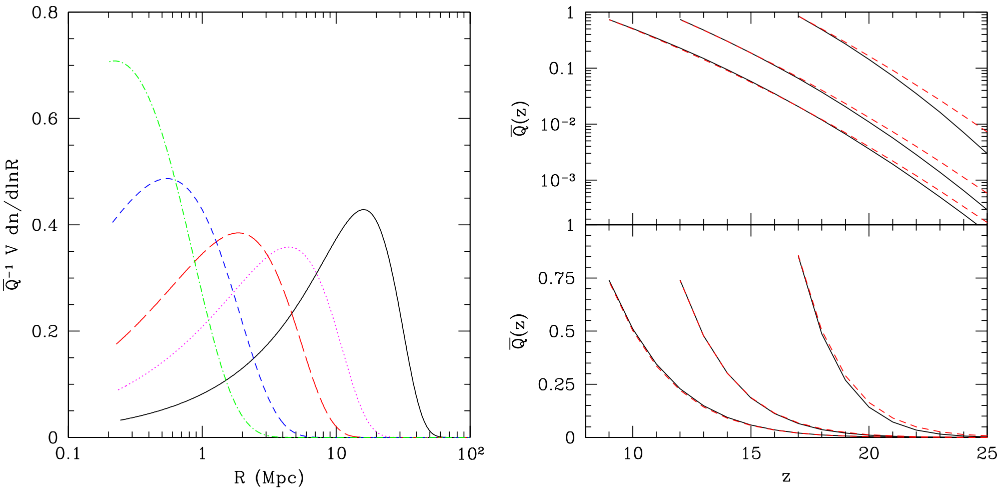

Figure 2.2 *Left panel*: bubble size distribution according to Equation 2.7. The lines represent the redshifts and ionization fractions (from left to right) z=18 (x_i = $\hat{Q}$=0.037), 16 (0.11), 14 (0.3), 13 (0.5), and 12 (0.74). The efficiency parameter ζ assumed here was 40. *Right panel*: the evolution of the global ionization fraction $\zeta f_{\rm coll}$ according to Equation 2.4 for the values of $\zeta = 500, 40, 12$. The dashed lines are the exact result, the solid lines are from the linear barrier approximation described in the text. From [50], permission to re-print from M. Zaldarriaga.

2.1.3 Monte-Carlo type implementation of the analytic model

We would like to use the formalism described in the previous section to predict non-spherical bubble shapes. In particular, we would also like to be able to compare the model directly to simulations of the reionization morphology that use radiative transfer. In this section we propose a new way of establishing the reionization morphology which amounts to a Monte-Carlo realization of the analytic model described in the previous section.

As the analytic reionization model provides us with a barrier prescription for assigning ionized regions, Equation 5.2, we can apply it to any three dimensional realization of the density field. A convenient option for the relatively high redshifts of interest is to generate Gaussian random fields from a linear theory power spectrum (the amplitude and shape of which we think we understand very well). The field is then smoothed with a top-hat window, describing spheres of influence from ionizing sources. The window convolution becomes a simple multiplication with the Fourier space analogue of the spherical top-hat, given by

$$W_{TH}(k, R_{\mathrm{TH}}) = \frac{(\sin x - x\cos x)}{x^3}, \quad x = kR_{\mathrm{TH}}\,. \tag{2.8}$$

To find the smoothing scale at which a given cell is ionized, we have to keep in mind (recall the discussion in the previous section) that it could also be ionized by photons originating from neighboring regions. Thus we should smooth the density on all possible scales to see whether a given point was above the ionization threshold of equation (5.2) for some smoothing scale. In practice, we start at large radii (comparable to the simulation box size) and record the smoothed overdensity as we smooth logarithmically on progressively smaller scales. When a cell first crosses the barrier (which depends only on redshift and ionization efficiency), it is deemed ionized. If later, as a function of decreasing scale, it crosses the barrier downwards, this means that the region had been initially ionized by a neighboring overdensity.

Figure 2.3 shows the ‘random walk’ of δ_0, the density fluctuation scaled to the present using linear theory, for three different regions inside a simulation box (where the efficiency parameter was chosen such that the universe is half ionized at redshift $z = 14.2$) with increasing $\sigma^2(m)$ (decreasing smoothing radius r). It also shows the ionization efficiency dependent barrier, from equation (5.1), as the solid curve. The short-dashed curve describes a region of high overdensity that self-ionizes. In the dotted curve at $\sigma^2(m) \simeq 2.2$ the barrier is crossed downwards, so the volume element was ionized by sources in neighboring cells. The long-dashed curve corresponds to an element that did not ionize at this redshift.

We show the resulting ionization field for an ionized volume fraction of $x_{\mathrm{i,V}} = 0.48$ in Figure 2.4. As underlying realization of the cosmic web we here used a Gaussian random field realization of the linear redshift 8 matter power spectrum generated with CMBFAST [56]. The box has a side length of 100 comoving Mpc/h. The slice shown is 10 Mpc/h deep. There is a wide range of different bubble sizes, mirroring the complex clustering behavior of sources, which themselves are of course missing in our simulation, which is solely based on the collapse fraction given a linear overdensity. In Chapter 5 we will study in more detail how the bubble morphology changes at different ionization fractions.

The ionization threshold according to Equation 5.2 can also be varied across a given box to show the redshift evolution of the signal and provide the reionization scenario on the light cone. The results of this procedure is shown for a 500 Mpc/h box in Figure 2.5, where we plot comoving extend of the field on the abscissa, and redshift on the ordinate. This implementation

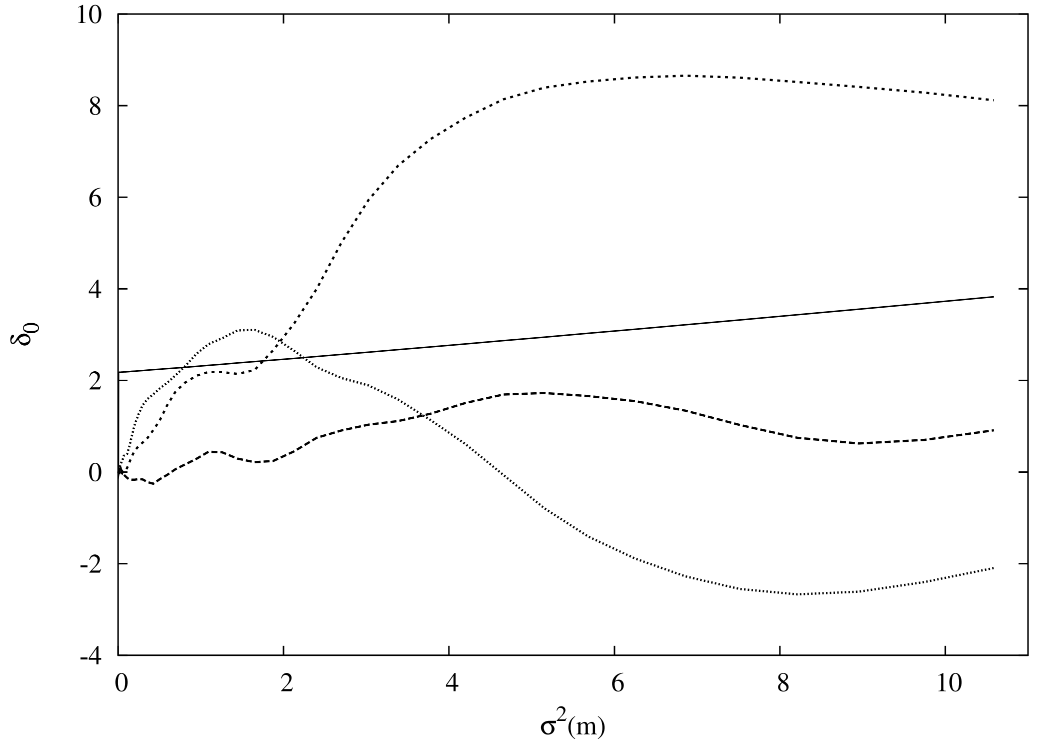

Figure 2.3 The behavior of the overdensity scaled to today, δ_0, for four regions from a 100 Mpc/h, 256^3, calculation. The abscissa in this plot is the rms fluctuation, dependent on the applied smoothing scale. The solid curve is the barrier given from equation (5.1). The region corresponding to the short dashed curve crosses the barrier for ionization at $\sigma^2(m) \simeq 1.8$. The region described by the dotted curve wanders below the barrier again, but has been ionized by sources in a neighboring region with higher density. Finally the long dashed curve represents a region in which the gas stays neutral at this particular redshift ($\overline{z} = 14.2$)

.

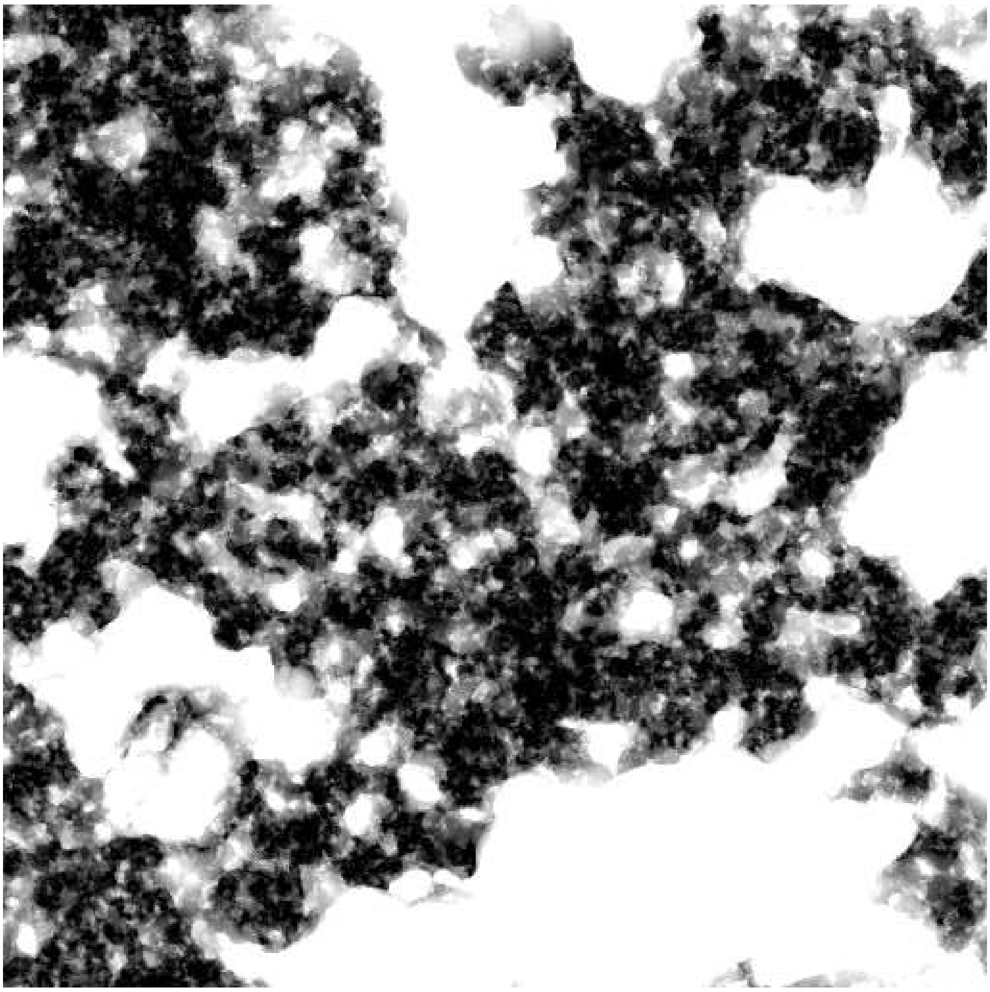

Figure 2.4 We show the result of the fast numerical scheme suggested here, based on Gaussian random field of extension 100 Mpc/h with a resolution of 512^3 cells. The (volume weighted) ionized fraction achieved at z=8 with an efficiency of $\zeta = 12$ is $x_{\rm i,V} = 0.48$. Clearly the bubble morphology produced by the semi-analytic scheme we proposed is very complex. There is also a wide distribution of bubble sizes (compare the black curve in Figure 2.2), and the largest HII regions can be several tens of comoving Mpc across.

illustrates nicely how small ionized regions form around a few most massive sources initially, and how the HII regions formed later merge to clusters that can be (at the final stages of reionization) of the order 100 comoving Mpc/h in size. For orientation, the angular scale probed by this box is given at the angular diameter distance[7] corresponding to $z = 8$ by $\theta = \frac{500}{6260} = 4.2°$. This simulation also re-iterates that within our analytic model, reionization takes place over a redshift interval of $\Delta z \simeq 3$.

This 'Fourier space radiative transfer' may seem as a bold simplification of the problem of describing propagation of radiation from sources through the IGM. In Chapter 5 we will expose our model to a number of detailed tests, and show that it in fact performs surprisingly well.

Our poor man's solution, by exploiting the speed of Fast Fourier transforms (FFT), has a number of advantages over brute force numerical methods of simulating reionization. To improve our understanding of reionization, various parametrizations of ζ and its time evolution may be compared to data from the next generation of experiments. In addition it is straightforward to generalize the analytic model to a mass-dependent ionizing efficiency [57]. In contrast to radiative transfer simulations, our implementation is not limited by similar CPU or memory related problems. For each box we need to Fourier transform $\simeq$ 50 times back and forward to do the smoothing. For a box with the dynamical range from 0.4-100 Mpc, this takes $\simeq$ 10 minutes per model on a Xeon 3.2 GHz computer. The implementation may be parallelized easily, hence the realization of a large number of parametrizations of reionization is feasible.

We should clarify our usage of the term 'Monte-Carlo'. The numerical scheme suggested in this section is *not random* in assigning the ionization state of any IGM cell. For a given realization of a density field it is deterministic in that it decides whether a region is ionized based on the density field smoothed on different scales. In this sense the criterion is *non-local*, because the ionization degree of a region does depend not simply on the linear overdensity of this region, but on the fluctuation of the surroundings. The procedure we suggested here is Monte-Carlo-like only because an underlying density field might be produced with random modes, using the power spectrum of matter fluctuations, which we think we know well from linear

---

[7] Given in our flat cosmology by

$$\mathcal{D}(a) = \int_a^1 \frac{da'}{a' H(a')}\,, \tag{2.9}$$

where a is the scale factor and H(a) is the expansion rate, $\dot{a}/a$. In our cosmology $H(a) = H_0 \left[a^{-3}\Omega_m + \Omega_\Lambda\right]^{1/2}$.

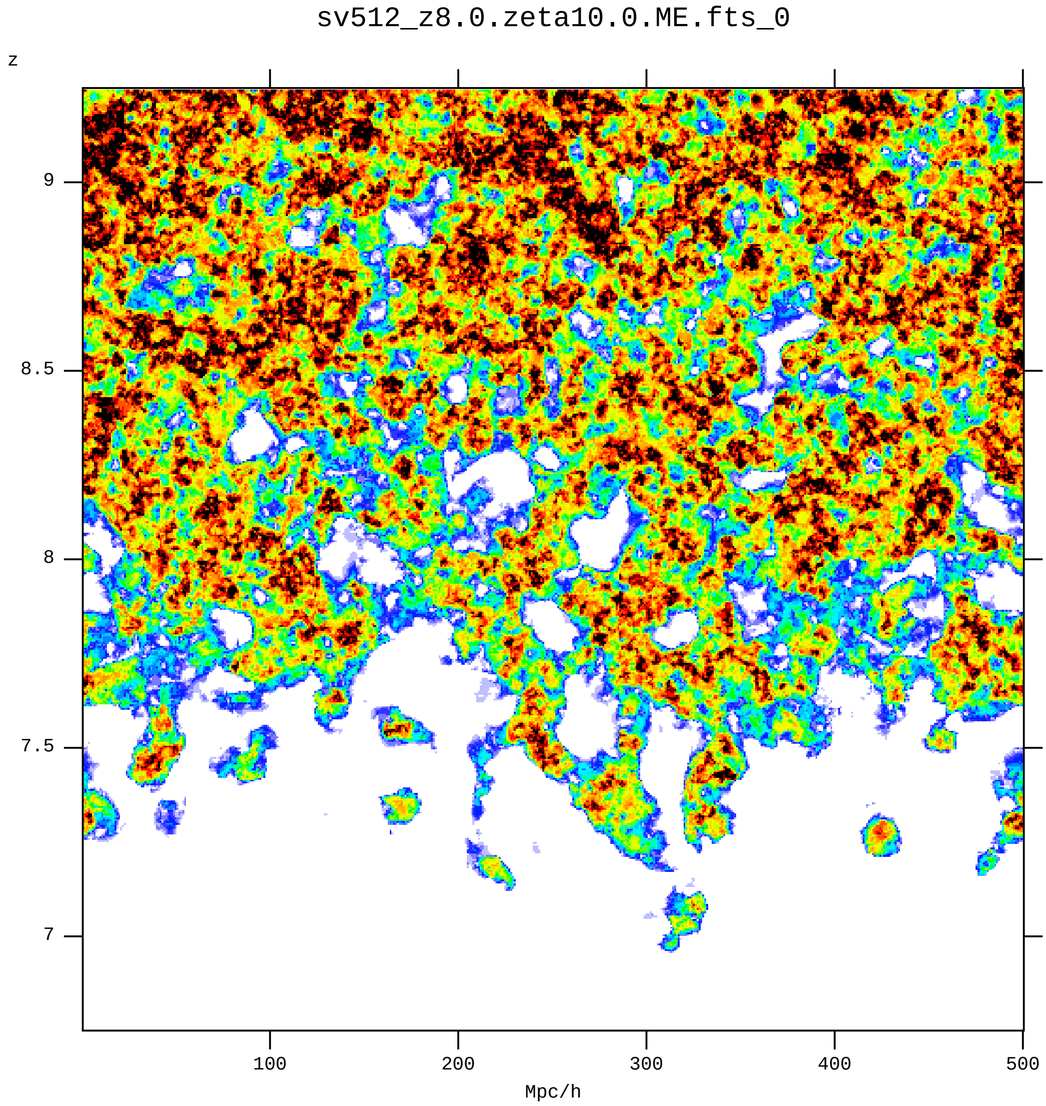

Figure 2.5 Shown is a 10 Mpc/h deep cut through an ionization box of comoving sidelength 500 Mpc/h. The ionization fraction is averaged over voxels and is color schemed between white (ionized) and black (neutral). Here we evolved the ionization threshold throughout the simulation, converting comoving distance to redshift along the y-axis. Reionization in this scenario takes place between redshift $z \simeq 9.5$ and $z \simeq 7$.

theory.

This is the advantage of the method suggested here over others: we can produce well-motivated reionization fields which carefully trace the large scale density fluctuations in a non-spherical manner. As we will show in Chapter 5, the resulting ionization morphology resembles that found in simulations, passing a number of quantitative tests. It will also be shown to guide our intuition beyond numerical simulations, because it does not have the same limitation in low mass source resolution.

2.2 21 cm radiation from high redshifts

In this section we will describe the physics behind a new potential probe of the reionization epoch. The 21 cm radiation we are interested in arises from from the spin-flip transition in clouds of neutral hydrogen at high redshift, with a rest frequency of $\nu_0 = 1420.4\,\mathrm{MHz}$. The incident intensity I_ν can be described by its equivalent brightness temperature $T_b(\nu)$, which is what would be required of a blackbody with spectrum B_ν such that $I_\nu = B_\nu(T_b)$. The Rayleigh-Jeans approximation is appropriate for the frequencies and temperatures of interest, so that $T_b(\nu) \simeq I_\nu\, c^2\, 2\, k_B\, \nu^2$.

Following the radiative transfer equation along a line of sight through a cloud of uniform excitation temperature $T_{\rm ex}$, the emergent brightness at a frequency ν is given by

$$T_b(\nu) = T_{\rm ex}(1 - e^{-\tau_\nu}) + T_R(\nu) e^{-\tau_\nu} \tag{2.10}$$

where the *optical depth* $\tau_\nu \equiv \int ds\, \alpha_\nu$ is the integral of the absorption coefficient (α_ν) along the ray through the cloud, T_R' is the brightness of the background radiation field incident on the cloud along the ray, and s is the proper distance.

The excitation temperature $T_{\rm ex}$ in this equation is also called the *spin temperature* T_S of the 21 cm transition. It quantifies the relative populations, n_i, of atoms in the two hyperfine levels (n=1 for triplet, n=0 for singlet) of the electronic ground state. The excitation temperature is then defined through

$$\frac{n_1}{n_0} = \frac{g_1}{g_0} e^{-E_{10}/k_B T_S} = 3\, e^{-T_\star/T_S} \tag{2.11}$$

where g_i is the statistical weight (here $g_0 = 1$ and $g_1 = 3$), $E_{10} = 5.9 \times 10^{-6} eV$ is the energy splitting, and $T_\star \equiv E_{10}/k_B = 0.068$ K is the temperature corresponding to the energy difference between the levels. In all astrophysical applications $T_S \gg T_*$, hence approximately three of four atoms find themselves in the excited state. Therefore the absorption coefficient must include a correction for stimulated emission, and it depends on T_S as well.

Let us next consider how the brightness temperature of the spin-flip transition evolves throughout different cosmological regimes. The spin temperature is a result of *three* processes whose relevance changes with time:

1. absorption and stimulated emission of CMB photons
2. collisions with other hydrogen atoms, electrons, and protons
3. scattering of UV photons.

In other words, the spin temperature is governed by (e.g. [58])

$$n_1 \left(C_{10} + P_{10} + A_{10} + B_{10} I_{\rm CMB}\right) = n_0 \left(C_{01} + P_{01} + B_{01} I_{\rm CMB}\right), \qquad (2.12)$$

where $C_{10/01}$ and $P_{10/01}$ are the de-excitation/excitation rates from collisions and UV induced transitions, B_{01} and B_{10} are the Einstein transition rates, and $I_{\rm CMB}$ is the intensity of incident CMB radiation. It can be shown that all relevant timescales are shorter than the typical expansion time, so the assumption of equilibrium is justified. In the Rayleigh-Jeans regime, equation (2.12) can be rewritten as [59]

$$T_S^{-1} = \frac{T_\gamma^{-1} + x_c T_K^{-1} + x_\alpha T_c^{-1}}{1 + x_c + x_\alpha}, \qquad (2.13)$$

where x_c and x_α are coupling coefficients for collisions and UV scattering, respectively, and T_K is the gas kinetic temperature. Here we have assumed detailed balance by requiring

$$\frac{C_{01}}{C_{10}} = \frac{g_1}{g_0} e^{-T_\star/T_K} \approx 3\left(1 - \frac{T_\star}{T_K}\right). \qquad (2.14)$$

We furthermore introduced an *effective color temperature of the UV radiation field* T_c via

$$\frac{P_{01}}{P_{10}} \equiv 3\left(1 - \frac{T_\star}{T_c}\right). \qquad (2.15)$$

We then need to determine x_c, x_α, and T_c. It can be shown that in most situations of interest $T_c \to T_K$ (see Section 2.2.3), and equation (2.13) may be rewritten

$$1 - \frac{T_\gamma}{T_S} = \frac{x_c + x_\alpha}{1 + x_c + x_\alpha}\left(1 - \frac{T_\gamma}{T_K}\right). \qquad (2.16)$$

2.2.1 Compton Heating and Collisional Coupling

At high redshifts, Compton scattering in the IGM between CMB photons and free electrons left over from recombination control the gas temperature. The heating rate is given by (e.g. [60])

$$\frac{2}{3}\,\frac{\epsilon_{\rm comp}}{k_B n} = \frac{\bar{x}_i}{1+f_{\rm He}+\bar{x}_i}\,\frac{8\sigma_T u_\gamma}{3m_e c}\,(T_\gamma - T_K)\,. \tag{2.17}$$

In this equation, $f_{\rm He}$ is the primordial helium fraction, $u_\gamma \propto T_\gamma^4$ is the energy density of the CMB, and σ_T is the Thomson scattering cross-section. The first factor appears as CMB photons scatter off free electrons, while the heat must be shared with all particles. The efficiency of Compton heating decreases with time when electrons recombine and the CMB energy density drops. The IGM thermally decouples from the CMB at a redshift given by [61]

$$1 + z_{\rm dec} \approx 150(\Omega_b h^2/0.023)^{2/5}. \tag{2.18}$$

The precise decoupling history can be calculated with the publicly available code RECFAST [62]. The black solid line in Figure 2.6 shows the CMB temperature evolution, the blue dashed line the gas temperature evolution resulting from RECFAST, leading to decoupling from the CMB at $z \simeq 200$.

At high redshift the spin temperature is coupled to the gas temperature through collisions. The collisional coupling strength is quantified through the coefficients in Equation 2.16, which are given by

$$x_c^i \equiv \frac{C_{10}^i}{A_{10}}\,\frac{T_\star}{T_\gamma} = \frac{n_i\,\kappa_{10}^i}{A_{10}}\,\frac{T_\star}{T_\gamma}\,. \tag{2.19}$$

Here, κ_{10}^i is the rate coefficient for spin de-excitation in collisions with that species in units of cm^3 s^{-1}. We must take into account coupling coefficients between various species: H-H collisions, H-e^- collisions and collisions of neutral atoms with protons, deuterium atoms, as well as Helium in its neutral or ionized states. We will not go in much detail here but refer the reader to e.g. [63] for details. It can be shown that $H-H$ collisions dominate throughout all regimes, and that collisions are able to couple the spin temperature effectively to the kinetic temperature of the gas between redshifts $z \simeq 150$ and $z \simeq 70$.

Once Compton heating becomes less important, as the free electron density decreases, the gas cools adiabatically, its temperature following a $1/a^2$ scaling of pressure-less dust. The CMB continues its $1/a$ cooling.

At even lower redshift the gas dilutes, the Hubble expansion makes the collision rate subdominant relative to the radiative coupling rate, and the spin temperature converges again toward the CMB temperature, driven by Compton scatterings. We can get a rough estimate for when collisions become unimportant by looking at the critical overdensity δ_{coll} at which $x_c = 1$ (e.g. [63])

$$1 + \delta_{\rm coll} = 1.04 \left[\frac{\kappa_{10}(88{\rm K})}{\kappa_{10}(T_K)}\right] \left(\frac{0.024}{\Omega_b h^2}\right) \left(\frac{70}{1+z}\right)^2 , \tag{2.20}$$

By $z \simeq 30$ the spin temperature again traces the CMB temperature so that the IGM becomes invisible. This is only valid as long as there are no early radiative processes from first sources, such as metal-poor Population III stars.

In Figure 2.6 we show the spin temperature evolution resulting from initial Compton heating and later adiabatic cooling. The CMB temperature is shown in the black solid line. The evolution of the gas temperature (blue dashed line) has been obtained by integrating over equation 2.17. The spin temperature (red, dot-dashed line) initially follows the gas temperature, but once collisional couplings become less important is drawn towards the CMB temperature through Compton scattering.

2.2.2 X-ray heating

Once the first sources of radiation turn on, the neutral IGM will be heated by their radiation. The most important heating channel is thought to be X-rays because of their long mean free path. X-ray sources are thought to homogeneously fill the universe almost as soon as collapsed objects form. There are two main candidates for their sources: supernovae and high mass binary systems. In the first case, radiation can inverse-Compton scatter of the relativistically ejected ionized particles to become highly energetic. This mechanism could be more important [64] at the high redshifts we are interested in, than in the local universe, because the energy density of radiation $u_\gamma \propto (1+z)^4$, so that the radiation field is substantially larger than in the starbursts observed locally. The second class of sources, high-mass binary systems, should be more abundant. In them, material from a massive main sequence star accretes onto a compact neighbor. The systems should be present within a few million years after the first stars are formed.

In studies of the high redshift X-ray background, the dependence of the luminosity for 0.2-10 keV photons on the star formation rate is usually extrapolated from low redshift observations with a conversion factor f_X to account for the different physics at high redshift (e.g. [65, 66]). Figure 2.7, panel (a) demonstrates the effect of varying this extrapolation normalization between 0.2 (in the blue dot-dashed curves) and 1 (in the solid curves).

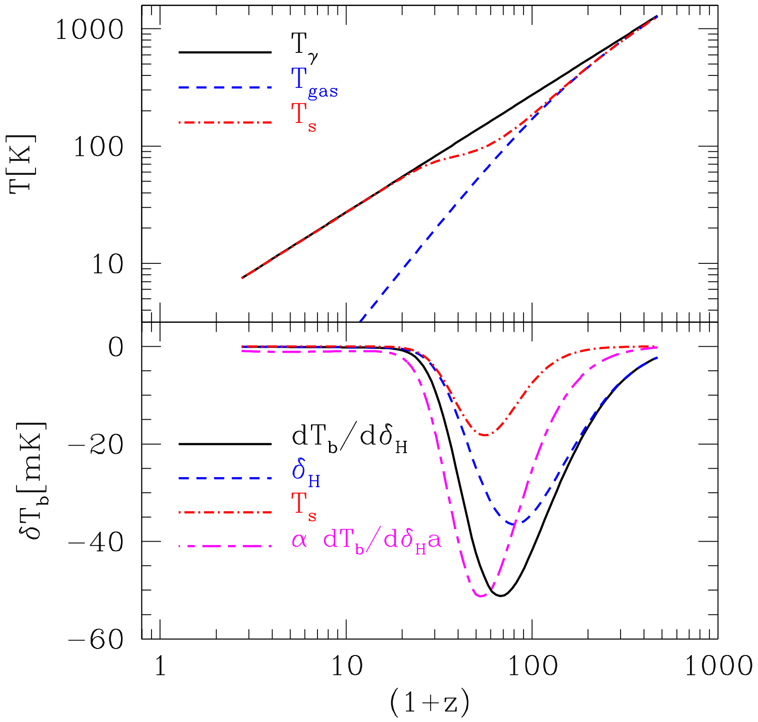

Figure 2.6 The evolution of the global spin temperature in the absence of collapsed objects. At z=200 the gas adiabatically cools away from the CMB and so does the spin temperature, coupled to the kinetic temperature through collisions. At $z \simeq 100$, the dilution of the gas leads to a ceasing of the collisional coupling. Compton scattering with remaining free electrons then brings the spin temperature in equilibrium with the CMB again. The bottom panel decomposes the brightness temperature fluctuation in fluctuations in the spin temperature (red dot-dashed), and those in the neutral hydrogen density (blue dashed). From [60], printed with permission by M. Zaldarriaga.

X-rays deposit their energy in the IGM by photoionizing hydrogen and helium. The hot primary electron then distributes its energy through collisional ionizations, producing more secondary electrons, collisional excitation of He, which produces a photon capable of ionizing H, and through Coulomb collisions with thermal electrons. The relative cross-sections of these processes determine the fraction of X-ray energy available for heating ($f_{X,h}$) and for ionization ($f_{X,\rm ion}$). These rates depend on $\bar{x}_i$ and the initial photon energy. It can be shown [67, 68] that X-ray heating should be quite rapid, and the fraction of photons going into ionization decreases quickly once there are

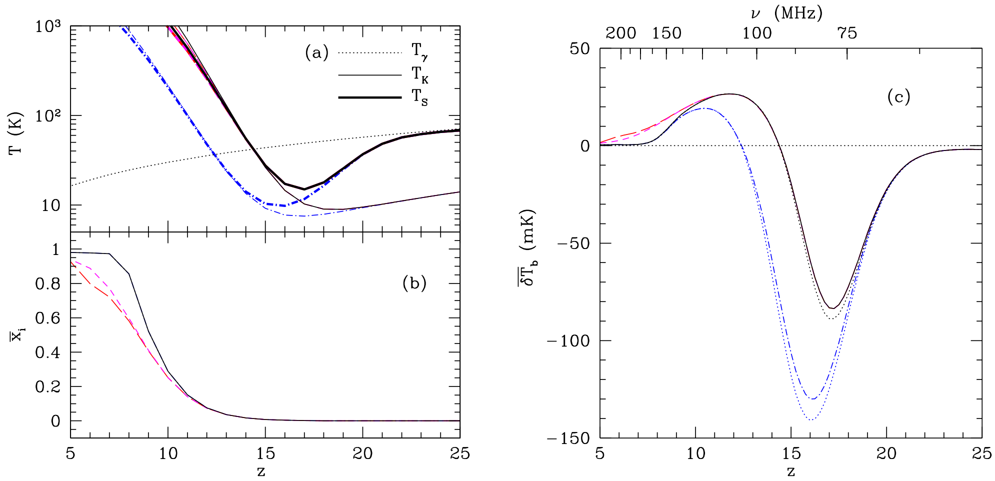

Figure 2.7 Spin temperature history in the presence of collapsed objects which lead to a X-ray background (heating the gas) and UV photons (coupling spin and kinetic temperatures) is shown in panel a). The CMB temperature is shown in the dotted, the gas kinetic temperature in the thin, and the spin temperature in the thick curve, respectively. Here reionization by Pop II star forming galaxies was assumed. The dot-dashed curves assume that a larger fraction of photons goes into reionizing the hydrogen atoms, $f_X = 0.2$. In this case the resulting spin temperature fluctuations could be substantial even during reionization, adding a layer of complexity. Panel b) shows the evolution of the ionized fraction. The long and short dashed curves assume a model for photo-heating feedback, limiting the influence of low mass sources. Panel c) then shows the differential 21 cm brightness temperature against the CMB. The two dotted lines show δT_b if shock heating is ignored. From [67], printed with permission by P. Oh.

sufficient free electrons. The formalism was first developed by [68].

The result of those calculations is shown in Figure 2.7. The thin solid and dot-dashed lines in panel (a) represent the gas ‘kinetic’ temperature, which is raised above the CMB temperature by the X-ray background. The dotted line is the CMB temperature The thick solid and dot-dashed lines are for the spin temperature. To understand the evolution of the spin temperature (thick lines) we have to discuss the role played by the UV background.

2.2.3 Wouthuysen-Field effect (Ly-α pumping)

Let us focus on the regime below z=30, which should be accessible to 21 cm experiments planned for the foreseeable future (the brightness temperature of galactic synchrotron, which is also called the *system temperature*, rises with falling radio frequency roughly as $\nu^{-2.6}$, while $T_{sys} = 440K$ at z=8.). During this regime, collisional coupling has ceased to be important because of the dilution of the IGM. As was suggested by Field and Wouthuysen [69, 59] at this time coupling of the spin temperature to the gas kinetic temperature by the UV background created by first collapsed objects becomes important. The way this process works is illustrated in Figure 2.8, where the hyperfine sublevels of the 1S and 2P states of hydrogen are drawn. The convention $n_F L_J$ was used to denote an atom with radial quantum number n, orbital angular momentum L, and total angular momentum J. $F = I + J$ is the quantum number obtained from the nuclear spin I and J.

Let us imagine an incident Lyα photon being absorbed by a hydrogen atom in the hyperfine singlet state. Transitions in which $\Delta F = 0, 1$ are allowed except for $F = 0 \rightarrow 0$. So the atom state can jump to either of the *central* 2P states.The dipole selection rules then allow this state to decay to the ${}_1S_{1/2}$ triplet level. The net effect is a change in hyperfine state by the absorption and subsequent re-emission of a Lyα photon. In principle any Lyman series photons can contribute through cascading effects, however in practive the higher level decays have only small importance [70].

Let us understand how effectively the Wouthuysen-Field effect will equilibrate kinetic and spin temperatures. The Lyα coupling depends on the effective temperature T_c of the UV radiation field, defined in equation (2.15). This is determined by the shape of the photon spectrum at the Lyα resonance. The color temperature of the radiation field matters because there is an energy difference between the hyperfine splittings of the Lyα transition. Hence the mixing process is sensitive to the gradient of the background spectrum near the Lyα resonance.

The medium is optically thick and a large number of Lyα scatterings will tend to bring the Lyα profile to a blackbody of temperature T_k near the line center. This is thought to be the case [69] in the high-redshift IGM, where in our cosmology the mean optical depth of a Lyα photon that redshifts across the entire resonance is given by [71]

$$\tau_{\rm GP} = \frac{\chi_\alpha \, n_{\rm HI}(z) \, c}{H(z)\nu_\alpha} \approx 3 \times 10^5 \, \overline{x}_{HI} \left(\frac{1+z}{7}\right)^{3/2} . \tag{2.21}$$

The primary mechanism responsible for establishing this equilibrium has been shown to be atomic recoil during scattering, tilting the spectrum to

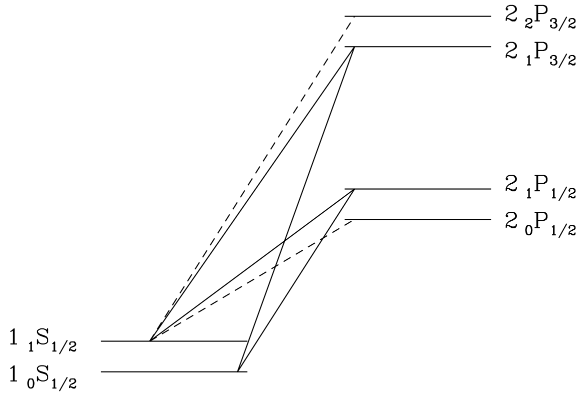

Figure 2.8 Level diagram illustrating the Wouthuysen-Field effect. We show the hyperfine splittings of the $1S$ and $2P$ levels. The solid lines label transitions that mix the ground state hyperfine levels, while the dashed lines label complementary transitions that do not participate in mixing.

the red [72]. For this reason the color temperature will essentially be equal to the kinetic gas temperature, $T_c \simeq T_k$. Finally the WF effect will couple the color temperature to the spin temperature so during this period we expect $T_s \simeq T_k$ overall.

Again we refer to Figure 2.7, a continuation of Figure 2.6 to lower redshift. The thin lines are the kinetic gas temperatures and the CMB temperature. Two additional pieces of physics have been added to the calculations shown here. The thick curves in panel (a) show the evolution of the spin temperature in the interval $z < 25$ for two different efficiencies of X-ray production. In the case with $f_X = 0.2$ (dot-dashed line), the hard X-ray luminosity is only 20% of that seen at low redshift for a given star formation rate [65]. In this case a larger fraction of radiation presumably goes into ionizations and some spin temperature fluctuations might survive into the beginning stages of reionization at $z \simeq 11$ (compare panel (b)), but quite soon we are in the regime $T_s \gg T_{\rm CMB}$. In panel (c), which shows the differential 21 cm brightness temperature, the two dotted lines show the case where heating by shocks in the IGM is ignored. This makes clear that X-ray heating is the most relevant mechanism in most cases.

Summary

We find that there are three important regimes for 21 cm cosmology. The line transition is first visible in absorption against the CMB when the gas cools adiabatically and couples the spin temperature to the gas temperature through collisions. Second, the collisions cease to be important and at redshift 30-50 there might be a dark gap where Compton scattering with residual free electrons re-establishes equilibrium of the spin temperature with the CMB. Once the first sources turn on, and distribute UV photons throughout the IGM, Wouthuysen-Field coupling can again lower the spin temperature toward the gas. Once the gas is heated by injection of X-ray radiation from inverse Compton scattering off the photons of electrons accelerated in Supernovae and accreting binaries, the spin temperature is driven (still coupled efficiently by the UV photons present to the gas kinetic temperature) to temperatures far above the CMB, before the universe undergoes substantial ionization.

Summing up the results from the previous sections, we may therefore express the 21 cm brightness temperature fluctuation as a combination of fluctuations in the following way

$$\delta_{21} = A\delta_b + A_x\delta_x + A_\alpha\delta_\alpha + A_T\delta_T - \delta_{\partial v} \,. \tag{2.22}$$

Here δ_i describes the fractional variation in quantity i where: $i = b$ for the baryonic density, $i = \alpha$ for the Lyα coupling coefficient x_α, $i = x$ for the neutral fraction (note that using the ionized fraction would cause a sign change), $i = T$ for T_K. Finally we have a term $i = \partial v$ for the line-of-sight peculiar velocity gradient, that arises because the signal is observed in redshift space. It is the only *anisotropic* term in the above expansion. The expansion coefficients can be shown to have simple physical explanations [67].

In chapters 3 and the power spectrum calculation of chapter 5 we will operate under the assumption that, within an extended interval before and during reionization, we can assume that the Wouthuysen-Field coupling and gas heating by X-rays are homogeneous. This assumption is based on the long mean free path expected by those photons with energies above 10.2 eV. In the next section, we will discuss the 21 cm power spectrum in this regime, which, as theoretical arguments suggest, should be limited to a redshift interval of roughly $\Delta z \simeq 5$ [73, 74, 67] directly proceeding reionization.

We will show how the presence of large scale velocity streams breaks the spherical symmetry of the observed (i.e. in redshift space) 21 cm power spectrum. We can in principle use this fact to distinguish cosmological parts of the power spectrum, i.e. those due to fluctuations in the distribution of matter) from astrophysical fluctuation modes (i.e. those due to the spin temperature and ionization fraction fluctuations).

2.3 The 21 cm Power Spectrum

The difference between the 21 cm brightness temperature at the observed frequency ν and the CMB temperature is [72]

$$T_b(\mathbf{x}) = \frac{3c^2\, h\, A_{10}\, n_H(\mathbf{x})\, a^3\; [T_s(\mathbf{x}) - T_{\rm CMB}(z)]}{32\pi\, k_B\, T_s(\mathbf{x})\, \nu_0} \left|\frac{\partial r}{\partial \nu}\right|, \tag{2.23}$$

where $A_{10} = 2.85 \times 10^{-15}\ s^{-1}$ is the spontaneous 21 cm transition rate, T_s is the spin temperature, $\nu_0 = 1420\, MHz$, and n_H is the number density of neutral hydrogen. The factor $|\partial r/\partial \nu|$ accounts for the Hubble flow as well as peculiar velocities.

Ignoring peculiar velocities, the 21 cm brightness temperature, relative to the CMB, at observed frequency, ν, and redshift, z, is then (e.g. [75]):

$$\begin{aligned}\delta T(\nu) \;&\approx\; 26\, x_H (1+\delta_\rho) \left(\frac{T_S - T_{\rm CMB}}{T_S}\right) \left(\frac{\Omega_b h^2}{0.022}\right) \\ &\quad \times \left[\left(\frac{0.15}{\Omega_m h^2}\right)\left(\frac{1+z}{10}\right)\right]^{1/2} \text{mK}.\end{aligned} \tag{2.24}$$

In this equation, x_H is the hydrogenic neutral fraction, $1+\delta_\rho$ is the gas density in units of the cosmic mean, T_S is the spin temperature, and $T_{\rm CMB}$ is the CMB temperature. The other symbols have their usual meanings. In this section, we will make the simplifying assumption that $T_S \gg T_{\rm CMB}$ globally during reionization, implying $\delta T \propto (1+\delta_\rho)x_H$ [73, 67, 74].

One way to quantify fluctuations $\delta_{T_b}(\mathbf{x})$ in the brightness temperature is through the power spectrum, the Fourier transform of the two point correlation function, defined through

$$\langle \delta(\mathbf{k}) \delta^*(\mathbf{k}') \rangle = (2\pi)^3\, \delta_D(\mathbf{k} - \mathbf{k}') P_\delta(k) \tag{2.25}$$

where $\delta(\mathbf{k})$ is the Fourier transform of the real space contrast $\delta(\mathbf{x})$. To the extend that fluctuations are Gaussian, the power spectrum offers a complete statistical description of the field. In the case of 21 cm fluctuations, we can at best expect this to be true in the epoch directly before reionization, where fluctuations in the spin temperature might be negligible compared to fluctuations in the density field. During reionization the extended HII regions with their sharply defined fronts will render the assumption of Gaussianity invalid and we can hope to gain complementary information from statistics beyond the power spectrum. We can further define the *dimensionless* power spectrum $\Delta^2(k) = k^3 P_\delta(k)/(2\pi^2)$, which gives the contribution to the variance of the field per $ln(k)$.

Ignoring peculiar velocities for now, the 21 cm power spectrum can be decomposed into the sum of several terms (generalizing the formula in [76]):

$$\begin{aligned}\Delta^2_{21}(k) = \langle T_b\rangle^2\langle x_H\rangle^2 \quad & [\Delta^2_{\delta_\mathrm{x},\delta_\mathrm{x}}(k) + 2\Delta^2_{\delta_\mathrm{x},\delta_\rho}(k) + \Delta^2_{\delta_\rho,\delta_\rho}(k) \\ + \quad & 2\Delta^2_{\delta_\mathrm{x}\delta_\rho,\delta_\mathrm{x}}(k) + 2\Delta^2_{\delta_\mathrm{x}\delta_\rho,\delta_\rho}(k) \\ + \quad & \Delta^2_{\delta_\mathrm{x}\delta_\rho,\delta_\mathrm{x}\delta_\rho}(k)]\end{aligned} \tag{2.26}$$

In this equation $\delta_x = (x_H - \langle x_H\rangle)/\langle x_H\rangle$ is the fractional fluctuation in the hydrogenic neutral fraction, and $\langle T_b\rangle$ is the average 21 cm brightness temperature relative to the CMB. Here and throughout $\Delta^2_{\mathrm{a,b}}(k)$ indicates the dimensionless cross-power spectrum between two random fields, a and b. The terms on the first line of Equation (2.26) are the usual low-order terms, representing the power spectrum of neutral hydrogen fluctuations, the cross power spectrum between neutral hydrogen and gas over-density, and the density power spectrum, respectively (e.g. Furlanetto et al. 2006c).

The terms on the following lines, which we can be referred to as 'higher order', were the focus of a paper not discussed in this thesis [77]. They reflect mode-couplings due to non-linear growth of structure, and can amount to large corrections, of order 100%, to the 21 cm power spectrum.

Going to redshift space

Starting from equation 2.24, we can ask what the effect of redshift space distortions will be. To calculate $\partial r/\partial\nu$, we relate comoving distance to frequency [78]

$$r = \int_{\frac{\nu}{\nu_0(1-v_r/c)}}^{1} \frac{c\, da}{a^2\, H(a)}, \tag{2.27}$$

where v_r is the l.o.s. peculiar velocity. Differentiating this expression, we find

$$\frac{\partial r}{\partial \nu} = -\frac{c}{a^2 \nu_0 H}\left[1 - \frac{1}{Ha}\frac{\partial v_r}{\partial r}\right], \tag{2.28}$$

where we have dropped terms of order $[(Ha)^{-1}\ \partial v_r/\partial r]^2$ and $[v_r/c]$. In the limit $T_s \gg T_{\mathrm{CMB}}$, fluctuations in the 21 cm brightness temperature at $\mathbf{x}$ can be expressed as

$$\begin{aligned} \frac{\Delta T_b(\mathbf{x})}{\tilde{T}_b} &= (1 - \bar{x}_i\,[1 + \delta_x(\mathbf{x})])\;(1 + \delta(\mathbf{x})) \\ &\times \left(1 - \frac{1}{Ha}\frac{\partial v_r(\mathbf{x})}{\partial r}\right) - \bar{x}_H, \end{aligned} \qquad (2.29)$$

where $\bar{x}_i \equiv 1 - \bar{x}_H$ is the global ionized fraction, δ_x is the overdensity in the ionized fraction and δ is the dark matter overdensity (on the scales and redshifts of interest, the baryons trace the dark matter), and we define the normalized temperature $\tilde{T}_b \equiv \bar{T}_b/\bar{x}_H$. In Fourier space, since the linear theory velocity at redshifts where dark energy is unimportant is $v(k,z) = -i\,H\,a\,\mathbf{k}\,\delta_L/k^2$, the peculiar velocity term is $\delta_v \equiv (Ha)^{-1}\;\partial v_r/\partial r = -\mu^2\delta_L$ where $\mu \equiv \hat{\mathbf{k}}\cdot\hat{\mathbf{n}}$, the cosine of the angle between the wavevector and the l.o.s., and L denotes the linear theory value.[8] Keeping terms to second order in $\{\delta, \delta^L\}$, the brightness temperature power spectrum is

$$\begin{aligned} \tilde{T}_b^{-2}\;P_{\Delta T}(\mathbf{k}) &= \left[\bar{x}_H^2\,P_{\delta\delta} + P_{xx} - 2\bar{x}_H\,P_{x\delta} + P_{x\delta x\delta}\right] \\ &+\; 2\mu^2\left[\bar{x}_H^2\,P_{\delta_L\delta} - \bar{x}_H\,P_{x\delta_L}\right] + \mu^4\left[\bar{x}_H^2\,P_{\delta_L\delta_L}\right] \\ &+\; \left[2P_{x\,\delta\,\delta_v x} + P_{x\,\delta_v\,\delta_v\,x}\right], \end{aligned} \qquad (2.30)$$

noting that $P_{xx} = \bar{x}_i^2\,P_{\delta_x\delta_x}$ and $P_{x\delta} = \bar{x}_i\,P_{\delta_x\delta}$. In our calculations, we drop the connected part and set $P_{x\delta x\delta} = P_{x\delta}^2 + P_{xx}\,P_{\delta\delta}$. In equation 2.30, we have decomposed the power spectrum into powers of μ; the last bracket in this decomposition has a non-trivial dependence on μ. For notational convenience, we refer to the k-dependent coefficients in equation (2.30) as P_{μ^0}, P_{μ^2} and P_{μ^4} and the terms in the last bracket as $P_{f(\mu,k)}$. The above decomposition should allow one to extract the "physics" – $P_{\delta_L\delta_L}$ – from the "astrophysics"– P_{xx} and $P_{x\delta}$ [80, 76]. The terms in the last bracket in equation (2.30) were omitted in their analysis, but must be included if reionization is patchy because $\delta_x \sim 1$ on scales at or below the bubble size. The disconnected part was calculated in [80].

The evolution of the ionized fraction over a mode can also affect the spherical symmetry of $P_{\Delta T}$, since time is changing in the l.o.s direction but not in the angular directions. The magnitude of this effect depends strongly on the morphology of reionization and we do not discuss it in this thesis (but see [81]).

The 21 cm background directly measures the baryonic density field δ_b (or even more precisely, the hydrogen density field). For most purposes, this

---

[8] The velocity field at $z \sim 10$ is in the linear regime for $k \leq 5$ Mpc^{-1}. See [79] for a discussion of the effect of the non-linear velocity field on the 21 cm signal. Upcoming interferometers are most sensitive to scales where the velocity field is linear.

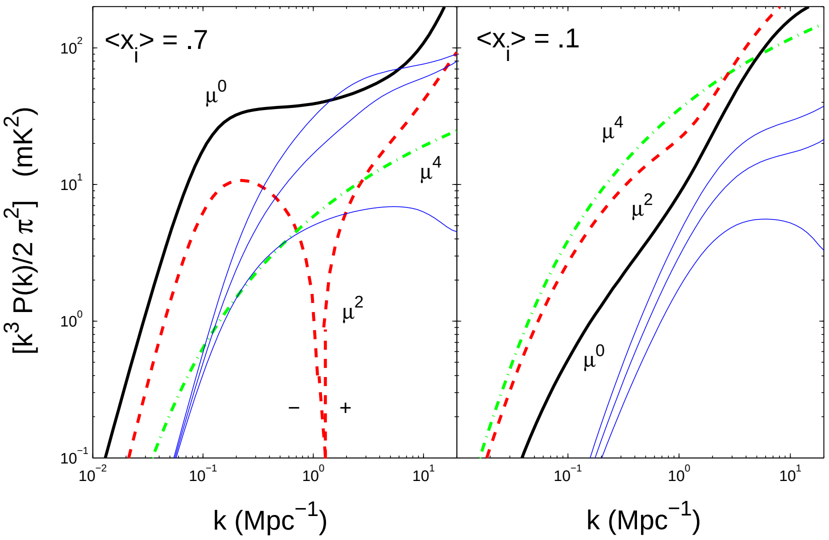

Figure 2.9 The μ decomposition of the signal (see equation 2.30) for $\bar{x}_i = 0.1$ and 0.7, corresponding to $z = 13.5$ and 9 in the $\zeta = 12$ model. The thick solid, dashed and dot-dashed are P_{μ^0}, P_{μ^2}, and P_{μ^4}, respectively. The three thin solid curves are the connected part of the terms in the last bracket of 2.30, calculated with $\mu^2 = 0.0, 0.5$ and 1.0 (in order of increasing amplitude).

is equivalent to the total matter density δ and in the following we will set $\delta_b = \delta$ throughout. However, note that on small scales the finite pressure of the baryons introduces a cutoff absent from the dark matter [82]; in detail, galaxy formation processes and feedback can also work on the two separately. To the extent that the matter fluctuations are probed we may try to extract cosmological information from the 21 cm power spectra. We will present results of such an analysis in the next section.

In Figure we show the different power spectrum components in equation 2.30, labeled by their characteristic dependence on μ. We used the model described in Section 2.1 to describe fluctuations in the ionized fraction. The μ^4 term is simply proportional to the density power spectrum, and we will use this feature below to constrain cosmological parameters. At high ionization fractions, the astrophysical terms, in particular the μ^0-term, can become large, as shown in the left panel.

2.4 Using the 21 cm power spectrum to constrain cosmological parameters

We can now turn to predictions of cosmological parameter constraints with future 21 cm experiments. A number of groups are ramping up to measure the reionization signal, among them the Mileura Wide Field Array (MWA) [9], the PrimeavAl Structure Telescope (PAST), and the Low Frequency Array (LOFAR) [10], while another second generation experiment, the Square Kilometer Array (SKA)[11] is being conceived. We will here focus on the MWA, LOFAR, and the SKA, for which experimental specifications are available [12]. Some specifications that are relevant for calculating sensitivities are shown in 2.1. The parameters we adopt come from [83] for MWA, [84] and www.lofar.org for LOFAR, and [85] for SKA.

LOFAR will have 77 large "stations," each of which combines the signal from thousands of dipole antennae to form a beam of ≈ 10 square degrees. Each station is able to simultaneously image N_p regions in the sky. We set $N_p = 4$ in our estimates, but this number may be higher. The signal from these stations is then correlated to produce an image. In contrast, MWA will have 500 correlated $4\,\mathrm{m} \times 4\,\mathrm{m}$ antenna panels, each with 16 dipoles. This amounts to a total collecting of 7000 m^2 at $z = 8$, or 15% of the collecting area in the core of LOFAR. While correlating such a large number of panels is computationally challenging, this design gives MWA a larger field of view (f.o.v.) than LOFAR, which is an advantage for a statistical reionization survey. The properties of the SKA have not yet been finalized, and it is quite possible that the EOR science driver for SKA may form a distinct array from the other, higher-frequency drivers. In addition, the successes of MWA and LOFAR will likely influence the final design of SKA. The collecting area for SKA is projected to be roughly 100 times larger than that of MWA. There are a number of competing designs for SKA's antennae. In one case, SKA will have roughly 5000 smaller antennae (like a much larger MWA).

Details of the sensitivity calculation are discussed in [80]. There we also derive the optimal antenna distribution for measurements of the EoR 21 cm signal. Figure 2.10 shows the result of this calculation, as statistical error in $[k^3\, P_{\Delta T}(k)/2\pi^2]$, for MWA (dashed), LOFAR (dash-dotted), and SKA (solid). Even though $P_{\Delta T}(k)$ is not spherically symmetric, we spherically average $P_{\Delta T}$ as well as the errors for the purpose of this plot. Because of

---

[9] http://web.haystack.mit.edu/arrays/MWA/

[10] http://www.lofar.org

[11] http://www.skatelescope.org/

[12] In the case of SKA, the specifications we use should be seen as tentative etimates

this averaging, the interferometers will be slightly more sensitive to some modes than this plot implies. At z = 6, the trend is as expected: SKA is more sensitive than LOFAR and LOFAR is more sensitive than MWA. Still, LOFAR's gains over MWA are not proportional to the square of the collecting area, a result of its smaller field of view. At higher redshifts, LOFAR and MWA are comparably sensitive on most scales. We also plot the sensitivity of MWA at $z = 8$ for a flat rather than the fiducial r^{-2} distribution of antennae. In this case, MWA is substantially less sensitive at *all* scales. This contrasts with angular power spectrum measurements, where a flat distribution of antennae is always more sensitive at larger k than a tapered distribution.

For these three arrays, the system temperature is dominated by the sky temperature. In our calculations, we set $T_{\rm sys} = T_{\rm sky} = 250\,K$ at $z = 6$, $T_{\rm sys} = 440\,K$ at $z = 8$ and $T_{\rm sys} = 1000\,K$ at $z = 12$ [83], and we set $B = 6$ MHz bandwidth, which translates to a conformal distance of 100 Mpc at $z = 8$.

All the significant foreground contaminants should have smooth power-law spectra in frequency. Known sources of radio recombination lines are estimated to contribute to the fluctuations at an insignificant level [20]. Before fitting a model to the cosmological signal, it is necessary to clean the foregrounds from the data. The idea is to subtract out a smooth function from the total signal prior to the parameter fitting stage [86]. Such pre-processing is common with CMB data sets, and [47] showed that this procedure can also be used in handling 21 cm observations. We will not go into detail here but refer the reader to [80]. The upshot is that in the Fisher analysis, the results of which are shown in Table 2.2, we only used modes larger then (scales smaller then) a minimum $k_{\rm min} = \frac{2\pi}{B}$, where $B = 6\,{\rm MHz}$ is the frequency depth of the observation. This has been chosen to minimize foreground contamination and evolution effects of the signal (the density field and ionization fraction) throughout the data volume.

To obtain an estimate, for how well our set of reionization parameters can be determined with planned experiments, we employ the Fisher matrix formalism. The Fisher or curvature matrix is defined to be expectation value of the second derivative of the natural logarithm of the likelihood function around its maximum for small parameter deviations:

$$F_{ij} = \langle \frac{\delta^2 (\ln \mathcal{L})}{\delta\theta_i \delta\theta_j} \rangle \, , \tag{2.31}$$

It provides us with a rough guess for the shape and width of the likelihood function in the multi-dimensional parameter space. The covariance matrix between the parameters $\mathbb{M}$ is given by the inverse of the Fisher matrix. This

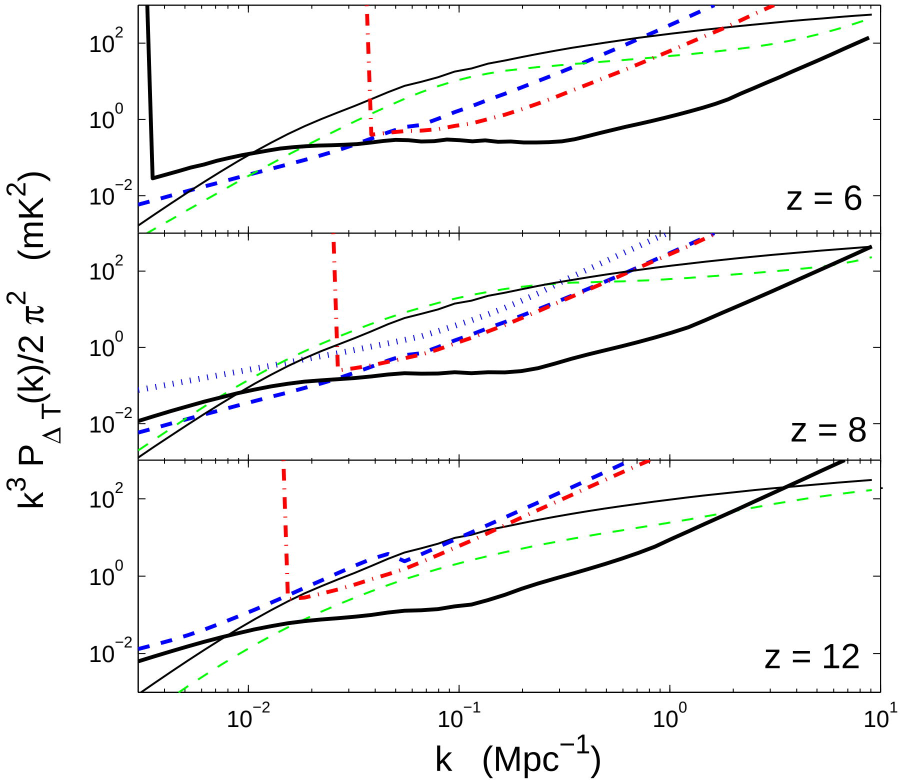

Figure 2.10 Detector noise plus sample variance errors for a 1000 hour observation on a single field in the sky, assuming perfect foreground removal, for MWA (thin dashed curve), LOFAR (thin dot-dashed curve), and SKA (thin solid curve) using the specifications given in Table 2.1 and for bin sizes of $\Delta k = 0.5\,k$. These errors are for the spherically averaged signal. The hashed line in the middle panel is for MWA with a flat distribution of antennae rather than the fiducial r^{-2} distribution. The detector noise dominates over sample variance for these sensitivity curves on almost all scales. The thick solid curve is the spherically averaged signal for $\bar{x}_i \ll 1$ and $T_s \gg T_{\rm cmb}$. We use this curve to calculate the sample variance error. For comparison, the thin dashed curves are the signal from the analytic model [50] when $\bar{x}_i$ is equal to 0.20, 0.55 and 0.75 for $z = 12, 8$ and 6, respectively. The foreground cutoff is not shown here, instead some experiments such as LOFAR have a sharp cutoff because of the size of their minimum baseline (compare Table 2.1).

Array	$N_{\rm ant}$	$N_{\rm ant}\,A_e$ (m^2) at $z=8$	f.o.v. (deg^2 at z=8)	min. baseline (m)	Cost (10^6 \$)
MWA	500	7000	$\pi\,16^2$	4	~ 10
LOFAR	64	4.2×10^4	$4\times\pi\,2.0^2$	100	$\sim 10^2$
SKA	5000	6.0×10^5	$\pi\,5.6^2$	10	$\sim 10^3$

Table 2.1 Survey parameters for upcoming 21 cm experiments: MWA, LOFAR, and SKA. Here we optimized the design for SKA for observations of the EOR, while keeping the current gross specifications for this array. Values for 10^3 hours of observation with $B=6$ MHz at 150 MHz. Due to its high survey speed, MWA will observe the largest field of these three experiments.

means that the one sigma error in the determinability of the parameters can be approximated by

$$\sigma_i = F_{ij}^{-1/2} \tag{2.32}$$

and that the correlation coefficient between the different parameters is

$$r_{ij} = M_{ij}/(\sigma_i\sigma_j) \tag{2.33}$$

where the M_{ij} are the elements of the parameter covariance matrix. Given an estimate for the 21 cm power spectrum and measurement sensitivity, 1-σ errors in the cosmological parameters λ_i are given in terms of the Fisher matrix

$$F_{ij} = \sum_{\rm k} \frac{1}{(\delta P_{\Delta T}(k))^2}\,\frac{\partial P_{\Delta T}(k)}{\partial\lambda_i}\,\frac{\partial P_{\Delta T}(k)}{\partial\lambda_j}. \tag{2.34}$$

The calculation in Table 2.2 assumes Gaussian variance of the signal, which is appropriate before reionization where we expect to encounter a Gaussian random field on large scales. During reionization, the ionization fraction fluctuations on the scale of the HII bubbles will not be Gaussian. They will lead to a non-Gaussian signal covariance matrix through which the connected four-point function will effectively correlate bands and will increase the diagonal elements. However especially for the first generation of experiments, the noise term will be dominating.

During reionization, we could also make use of the decomposition 2.30 to get at the cosmological part of the signal. We showed in [80] that this is difficult in practice, basically because foreground contamination limits the number of modes that can be extracted along the line of sight. However it is these modes that contribute most to the μ^4 term P_δ which we would like to measure to get at the purely cosmological P_{δ_L}. Hence we will concentrate (in Table 2.2) on the regime before regionization, where the 21 cm power spectrum is simply the density power spectrum boosted by the constant 'Kaiser factor' of $\langle(1+\mu^2)^2\rangle = 1 + 1 + 2/3 + 1/5 \simeq 1.87$.

We find that the first generation of 21 cm observations should moderately improve existing constraints on cosmological parameters for certain low-redshift reionization scenarios, and a two year observation with the second generation interferometer MWA5000 in combination with the CMB telescope Planck can improve constraints on Ω_w (to ± 0.019, a 30% improvement over Planck alone), $\Omega_m h^2$ (± 0.0011, 50%), $\Omega_b h^2$ (± 0.00013, 30%), Ω_ν (± 0.003, 300%), n_s (± 0.0034, 30%), and α_s (± 0.004, 100%). Larger interferometers, such as SKA, have the potential to do even better.

	τ	Ω_w	w	$\Omega_m h^2$	$\Omega_b h^2$	n_s	$\delta_H \times 10^5$	α_s	Ω_ν	$\bar{x}_H$
Fiducial param. value	0.1	0.7	-1.0	0.14	0.022	1.0	3.91	0.0	0.0	1.0
LOFAR	-	0.09	-	0.14	0.04	0.14	3.9	-	-	-
MWA	-	0.10	-	0.13	0.03	0.13	3.9	-	-	-
MWA5000	-	0.007	-	0.011	0.003	0.03	0.31	0.012	0.008	-
SKA	-	0.005	-	0.009	0.002	0.04	0.26	0.011	0.009	-
Planck	0.0050	0.029	0.09	0.0023	0.00018	0.0047	0.026	0.008	0.010	-
Planck +MWA5000	0.0046	0.019	0.07	0.0011	0.00013	0.0034	0.018	0.004	0.003	0.05
Planck + SKA	0.0046	0.018	0.07	0.0009	0.00013	0.0033	0.018	0.003	0.004	0.05

Table 2.2 Errors on cosmological parameter estimates when density fluctuations dominate the 21cm signal for two year observations with 21 cm interferometers and in combination with Planck. We assumed, unless otherwise noted, observations of 2000 hrs on two places in the sky in a $6MHz$ band which is centered at $z = 8$. In these calculations, we account for foregrounds by imposing a sharp cutoff in sensitivity at $k = 2\pi/B$, where B is the width of the box, and we avoid fitting to scales in the non-linear regime by imposing a small scale cutoff at $k = 2$ Mpc^{-1}. The calculations are for a flat universe, $1 = \Omega_m + \Omega_w$, and dashes indicate parameters which are not marginalized. MWA5000 is a conceived extension of the MWA, which builds on the design layout by increasing the number of receivers by a factor of ten. We point out that from just the 21 cm data, the parameter δ_H is completely degenerate with $\bar{x}_H$. Because of this, for 21 cm observations alone, the constraints in this column are really for the parameter $\bar{x}_H\,\delta_H$. Predictions for SKA are for ten locations on the sky, 400 hours each.

Summary

In comparison to the other reionization probes mentioned in the introduction, the 21 cm transition has the great advantage of offering to probe the high redshift IGM tomographically, by making three dimensional maps. The line transition can also be used to probe the pre-reionization IGM. The dataset that can be acquired this way is – e.g. in comparison to the CMB – potentially very large. Let us imagine measuring an angular mode l, corresponding to a wave number $k \simeq l/r$. Two maps at different frequencies will be independent if they are separated by a radial distance $1/k$. An experiment covering a spatial range Δr can probe a total of $k\Delta r \simeq l\Delta r/r$ independent maps. A 21 cm experiment taking data over a range $\Delta\nu$ centered on frequency ν is then sensitive to $\Delta r/r \simeq 0.5(\Delta\nu/\nu)(1+z)^{-1/2}$. The number of data points acquired by such an experiment is (say it is centered at z=13, and measures fluctuation in the regime z=6-27 so that $\Delta\nu = \nu$)

$$N_{\rm 21cm} \simeq 10^{17}(l_{\rm max}/10^6)^3(\Delta\nu/\nu)(z/13)^{-1/2} \tag{2.35}$$

independent samples, where the multipole number l corresponds to a mode of wavelength $\lambda = (2\pi)/(l/r)$. Of course this number has been derived under the extremely optimistic assumption of frequency and angular resolution such that fluctuations can be observed all the way down to the Jeans smoothing scale of $l \simeq 10^6$, but it demonstrates the point (made originally by [60]). In comparison, the CMB contains only $N_{cmb} \simeq 2l_{max}^2 \simeq 2 \times 10^7(l_{max}/3000)^2$ Fourier independent data points in both temperature and polarization. The limit in this case is Silk damping [87] (this process is responsible for the exponential decay of power in the CMB on scales $l \simeq 3000$; it is due to photon diffusion in the last scattering surface, because recombination is not a completely instantaneous process).

Even if the amount of *data* in 21 cm will be larger than ongoing CMB analyses, the challenge will lie in extracting as much *information* about physics as possible from it. We would expect that the 21 cm signal from the considered range of redshifts will contain – beyond information about the fluctuations of baryons or matter – information about fluctuations in the UV background and about inhomogeneous X-ray heating [74]. Most importantly though, it will contain information about fluctuations in the ionized fraction which we would like to use to infer knowledge about the nature of the sources responsible for this phase transition of the IGM.

Chapter 3

Lensing Reconstruction using redshifted 21 cm fluctuations[1]

In this chapter we investigate the potential of second generation measurements of redshifted 21 cm radiation from before and during the epoch of reionization (EOR) to reconstruct the matter density fluctuations along the line of sight through the gravitational lensing effect. To do so we generalize quadratic methods developed for the Cosmic Microwave Background (CMB) to 21 cm fluctuations. We show that the three dimensional signal can be decomposed into a finite number of line of sight Fourier modes that contribute to the lensing reconstruction. Our formalism properly takes account of correlations along the line of sight and uses all the information contained in quadratic combinations of the signal.

In comparison with the CMB, 21 cm fluctuations have the disadvantage of a relatively scale invariant unlensed power spectrum which suppresses the lensing effect. The smallness of the lensing effect is compensated by using information from a range of observed redshifts.

We estimate the size of experiments that are needed to measure this effect. With a square kilometer of collecting area and a maximal baseline of 3 km one can achieve lensing reconstruction noise levels an order of magnitude below CMB quadratic estimator constraints at $L = 1000$, and map the deflection field out to less then a tenth of a degree ($L > 2000$) within a season of observations on one field. Statistical lensing power spectrum detections will be possible to sub-arcminute scales, even with the limited sky coverage that currently conceived experiments have. One should be able to improve constraints on cosmological parameters by using this method. With larger

---

[1] Based in part on O. Zahn & M. Zaldarriaga, Astrophysical Journal, 653, in press (2006)

collecting areas or longer observing times, one could probe arcminute scales of the lensing potential and thus individual clusters. We address the effect that foregrounds might have on lensing reconstruction with 21 cm fluctuations.

3.1 Introduction

In Chapter 2 we discussed measurements of the 21 cm radiation from before and during reionization as a potential probe of cosmological parameters. We found that due to the confounding effects of their unknown astrophysics it might be difficult to compete with the constraints on cosmological parameters (see Chapter 2 and [80]) coming from future microwave background experiments. A few very ambitious probes on the CMB side are the Planck satellite [2], the Atacama Cosmology Telescope (ACT) [3] [88], or the South Pole Telescope (SPT) [4] [89]).

Here we will go a different route, and explore the cosmological information contained in the 21 cm measurements about the intervening mass distribution at lower redshifts through the lensing effect. Before the ionized fraction of the IGM becomes substantial, the 21 cm emission against the CMB is a near Gaussian random field. In this regime, which is the focus of the present article, the quadratic estimator should be close to optimal [90].

We will look at 21 cm fluctuations at their lowest possible redshift range, $z = 6-12$, where the second generation of experiments (such as the SKA and MWA50k described in Chapter 2) might be able to measure at high signal-to-noise. Using our formalism we can also estimate information losses due to foreground contamination, once these have been described by some model. We also explore the possibility to constrain the dark energy density with lensing of the 21 cm background. Another application would be to measure nonlinearities in the density field, or the contribution of neutrinos to the energy density of the universe. We compare our results to the potential of a future high precision observation of the CMB. The CMB damping tail is an advantage for lensing reconstruction since reconstruction errors decrease with increasing slope, but at the same time it leads to a small scale limitation for CMB reconstruction, as the signal quickly falls below the noise.

Lensing reconstruction using the redshifted 21 cm radiation *in absorption* against the CMB has been investigated before by [91], in particular also the possibility to get a handle on gravity waves from inflation by gravitational lensing cleaning of B mode polarization (lensing converts E to B modes of the

---

[2] http://www.rssd.esa.int/index.php?project=PLANCK&page=perf_top

[3] see http://www.hep.upenn.edu/ angelica/act/act.html

[4] see http://astro.uchicago.edu/spt/

polarization and acts as a contaminant to the primordial signal) [92]. Their work describes two types of observations, which employ a 20/200 times larger total collecting area than we will assume here (and five times longer observation time) to observe angular fluctuations $L_{max} = 5000 - 10^5$ in the 21 cm field. The problem is that the prospect, beating the CMB level for B mode lensing cleaning, relies on measuring the 21 cm power spectrum at very high redshifts (they use $z_{\rm source} = 30$), at which the galactic synchrotron contamination is a factor $\simeq 20$ larger than for example at redshift 8. The reason such high redshift observations are needed to compete with likelihood based lensing estimation is that there is a partial delensing bias when comparing lenses out to different redshifts and $z_s = 30$ turns out to be close enough to the last scattering surface of the CMB, where gravity waves are expected to create the B mode fluctuations. These authors furthermore make the approximation of treating their slices through the 21 cm measurement cube as uncorrelated, which is not warranted.

Reference [93] suggested measuring the effective convergence from the effect it has on the real space variance map of 21 cm fluctuations. The author also presented rough sensitivity estimates for LOFAR, PAST, and SKA. We improve on this by using all the available information in convergence and shear in an optimal way and use more realistic errors.

In section 2 we review the quadratic estimator technique for lensing reconstruction following [94]. Then we naturally expand the formalism to the extraction of weak lensing from an intrinsically three dimensional signal. The decomposition of the line of sight component of the signal into modes leads to a hierarchy of independent lensing backgrounds that can be probed with varying precision. Although our concentration lies on applying the quadratic estimator to the epoch immediately before substantial ionization occurs, we scrutinize its applicability to the patchy regime by using an analytic model for the morphology of HII regions.

In section 3 we put our investigation in the context of experiments, estimating the potential redshift range in which they will observe. Because signal and noise are evolving with redshift, we break down the volume of the observation in smaller boxes along the line of sight. We calculate estimates for the lensing reconstruction future 21 cm experiments might be able to achieve.

We present results based on current rough specifications of the Square Kilometer Array (SKA) in Section 4 and compare them to the possibility of constraining the matter power spectrum with the CMB temperature and polarization. The 21 cm approach turns out to have no angular scale limitation for constraining the convergence. We address limitations due to the galactic foreground and show how these can be incorporated into our formalism in a straightforward manner. We conclude with an outlook and discussion in section 5.

We discussed the theory of the 21 cm signal in Chapter 2. Here we will assume that in the regime of interest $f \simeq 1$, hence we obtain with $T_s \gg T_{\mathrm{CMB}}$ that the power spectrum of the 21 cm brightness temperature fluctuation in the neutral regime is given by

$$P_{\Delta T_b}(k) \simeq (26\mathrm{mK})^2 \frac{1+z}{10}(1+\mu_k^2)^2 P_\delta(k) \tag{3.1}$$

In this chapter, we shall be mainly concerned with quadratic estimator lensing reconstruction during this highly neutral regime. The extension to a patchy epoch is complicated by the presence of a connected four-point function contribution to the source field. On the level of the power spectrum this contribution acts as a sample variance term, correlating different k-modes.

Figure 3.1 shows the angular power spectrum of 21 cm fluctuations at redshift 8 for different values of the efficiency and therefore ionization fraction. We see that up to an ionization fraction of $x_i = 0.7$ the signal on small scales decreases (structures below the bubble scale are washed out) while the ionized regions lead to a bump in the power spectrum on scales $k \simeq 0.2$ h/Mpc which corresponds to an angular multipole at the relevant redshifts of approximately $l = 1000$. At even higher ionized fractions, the entire patchy power spectrum lies below the neutral case, so it becomes more difficult to observe the fluctuations and hence to use them for lensing reconstruction. In any event it seems from Figure 3.1 that a significant part of the patchy regime can be used for the lensing reconstruction, in part because the boosted amplitude on scales $l \simeq 100 - 1000$ might aid somewhat in this effort. We will evaluate these estimates more carefully in Section 3.4. Our choice of ionization efficiency lets reionization begin at redshifts around 8 and evolves rather slowly, due to photon consumption by clumps in the IGM. It evolves through $x_i \simeq 50\%$ at redshift 7 to complete at redshift 6.

We will assume a bandwidth of $B = 5\,\mathrm{MHz}$ for calculating the power spectrum at various redshifts. This corresponds to a redshift interval $\Delta z = 0.286$. During the neutral phase the density fluctuations evolve slowly, however the sensitivity of the experiments change rapidly with observation frequency. Because the comoving length scale is given in terms of bandwidth through

$$\mathcal{L} \approx 1.2 \left(\frac{B}{0.1\mathrm{MHz}}\right) \left(\frac{1+z}{10}\right)^{1/2} \left(\frac{\Omega_m h^2}{0.15}\right)^{-1/2} \mathrm{Mpc/h}, \tag{3.2}$$

our window in frequency space corresponds to a depth of 50 Mpc/h at z=6 and to 70 Mpc/h at z=12. When the first extended HII regions start forming, the power spectrum evolves more rapidly, however reionization still only

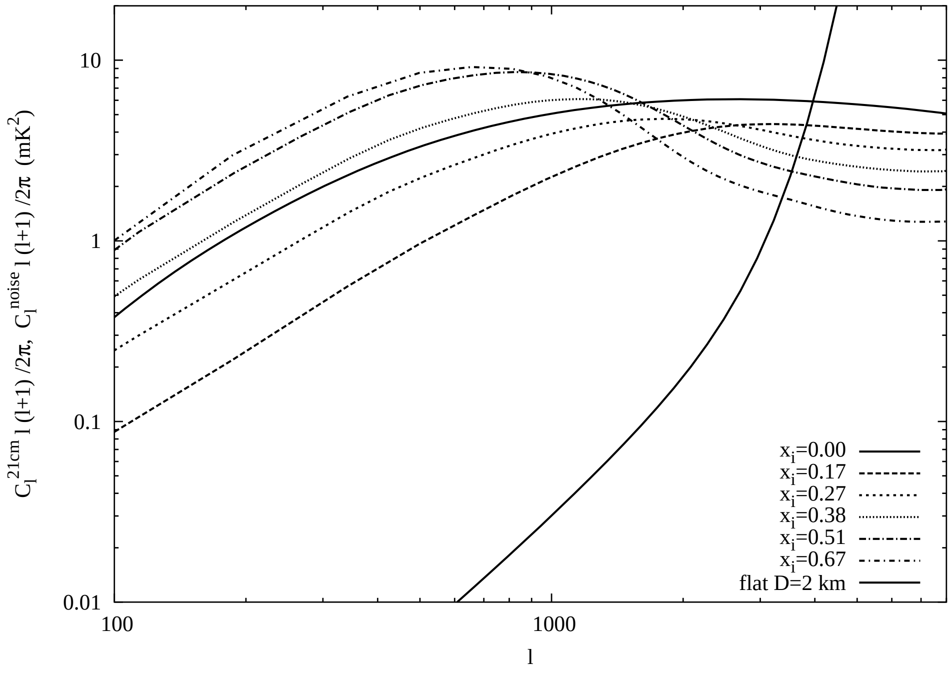

Figure 3.1 Angular power spectrum of the 21 cm signal at various stages during reionization. The thick solid line shows the expected noise for SKA for a flat configuration of antennas inside a circle of diameter 2 km. When the ionization fraction rises during the expansion of HII spheres, first the overall signal decays, then bubbles cluster quickly to form large ionized regions tens of Mpc/h across. This can lead to a significant increase in the signal on scales that the first imaging 21 cm experiments should be sensitive to. On the smallest scales the signal is decreased, making usage of 21 cm fluctuations for lensing reconstruction somewhat more difficult.

lapses over a comoving length of about 300 Mpc/h, in comparison to which our window is small.

We will generate 21 cm brightness temperature power spectra following Formula 3.1 using linear power spectra that contain the acoustic oscillation amplitude generated from CMBFAST transfer functions [56]. The baryonic wiggles included in the code might aid somewhat in our reconstruction endeavour, for reasons given in the next section. We use the same transfer functions to implement the signal in three dimensional Gaussian random fields and model the patchy phase.

A ΛCDM cosmology is assumed throughout all calculations, with parameters $\Omega_m = 0.3$, $\Omega_\Lambda = 0.7$, $\Omega_b = 0.04$, $H_0 = 100$hkm/sec/Mpc (with h=0.7), and a scale-invariant primordial power spectrum with $n = 1$ normalized to $\sigma_8 = 0.9$ at the present day.

3.2 Weak Lensing Reconstruction

3.2.1 Quadratic Estimator, General Consideration

Lensing by large scale structure can be observed whenever there is a fluctuating background field. At position $\hat{\mathbf{n}}$ we observe the field

$$T(\hat{\mathbf{n}}) = \tilde{T}(\hat{\mathbf{n}} + \nabla\phi) \tag{3.3}$$

where $\tilde{T}$ denotes the unlensed field, $\delta\theta = \nabla\phi$ is the displacement vector while ϕ is the projected potential. Here and in what follows, boldface quantities denote vectors. The projected potential is given in terms of the gravitational potential $\psi(\mathbf{x}, \mathcal{D})$, where $\mathbf{x}$ is position and $\mathcal{D}$, the angular diameter distance, is used as time variable, as

$$\phi(\hat{\mathbf{n}}) = -2 \int d\mathcal{D} \frac{\mathcal{D}_A(\mathcal{D}_s - \mathcal{D})}{\mathcal{D}\mathcal{D}_s} \psi(D\hat{\mathbf{n}}, D)\,. \tag{3.4}$$

So the power spectrum of the displacements is $C_L^{\delta\theta\delta\theta} = L(L+1)C_L^{\phi\phi}$.

An estimator $D(\hat{\mathbf{n}})$ for the lensing displacement field information contained in the temperature field should contain an even number of temperature terms since the expectation value for odd powers would vanish. It must also satisfy the condition

$$\langle D(\hat{\mathbf{n}}) \rangle = \delta\theta(\hat{\mathbf{n}}) \tag{3.5}$$

when averaged over many realizations of the background radiation field, that is for example the CMB or 21 cm radiation.

[95] showed that the divergence of the temperature-weighted gradient of the map achieves maximal signal-to-noise among quadratic statistics. In Fourier space this quadratic estimator takes the form [96]

$$D_{\text{est.}}(\mathbf{L}) = A(L) \int \frac{d^2l}{(2\pi)^2} F(\mathbf{l}, \mathbf{L}-\mathbf{l}) T(\mathbf{l}) T(\mathbf{L}-\mathbf{l}) \tag{3.6}$$

The Filter $F(\mathbf{l}, \mathbf{L}-\mathbf{l})$ is obtained by minimizing the variance of $D_{\text{est.}}$ under the normalization condition for $D(\mathbf{L})$

$$F(\mathbf{l}, \mathbf{L}-\mathbf{l}) = \frac{[C_l \mathbf{L}\cdot\mathbf{l} + C_{L-l}\mathbf{L}\cdot(\mathbf{L}-\mathbf{l})]}{2\tilde{\text{C}}_l^{\text{tot}}\tilde{\text{C}}_{L-l}^{\text{tot}}} \tag{3.7}$$

and the normalization is

$$A(L) = L \left[\int \frac{d^2l}{(2\pi)^2} \frac{[C_l L\cdot l + C_{L-l} L\cdot(L-l)]}{2\,\tilde{\text{C}}_l^{\text{tot}}\tilde{\text{C}}_{L-l}^{\text{tot}}} \right]^{-1} \tag{3.8}$$

Here $\tilde{\text{C}}_l^{\text{tot}}$ is the sum of the lensed angular power spectrum of 21 cm fluctuations $\tilde{\text{C}}_l$ and the noise power spectrum which we will give in the next section, C_l^N. As shown by [97], the effect of lensing on the angular 21 cm power spectrum for an individual plane is small, so one can use the unlensed power spectrum in place of it. The high-pass shape of the quadratic estimator gives it a property all reconstruction methods share, that they extract most information from the smallest scales resolved by some experiment. We emphasize that the estimator is unbiased by construction (Equation 3.5), independent of Gaussianity of the source field.

With the definition of the lensing reconstruction noise power spectrum N_L^D

$$\langle D^*(\mathbf{L}) D(\mathbf{L}') \rangle = (2\pi)^2 \delta(\mathbf{L}-\mathbf{L}')(C_L^{DD} + N_L^D) \tag{3.9}$$

evaluation of the variance of Equation 3.6, $\langle ||D(\mathbf{L})||^2 \rangle = (2\pi)^2 \delta^D(0) N_L^D$ gives

$$\begin{aligned} N_L^D(L) &= L^2 \left[\int \frac{d^2l}{(2\pi)^2} \frac{[C_l\,\mathbf{L}\cdot\mathbf{l} + C_{L-l}\,\mathbf{L}\cdot(\mathbf{L}-\mathbf{l})]^2}{2\,\tilde{\text{C}}_l^{\text{tot}}\,\tilde{\text{C}}_{L-l}^{\text{tot}}} \right]^{-1} && (3.10) \\ &= A(L) L && (3.11) \end{aligned}$$

Roughly, when $C_L^{DD} = N_L^D$, then structures down to the angular size $2\pi/L$ in the lensing field can be reconstructed.

We illustrate the different power spectrum characteristics of CMB and 21 cm in Figure 3.2, where we re-scaled the 21 cm power spectrum to be of comparable amplitude. While the CMB fluctuation signal exhibits more

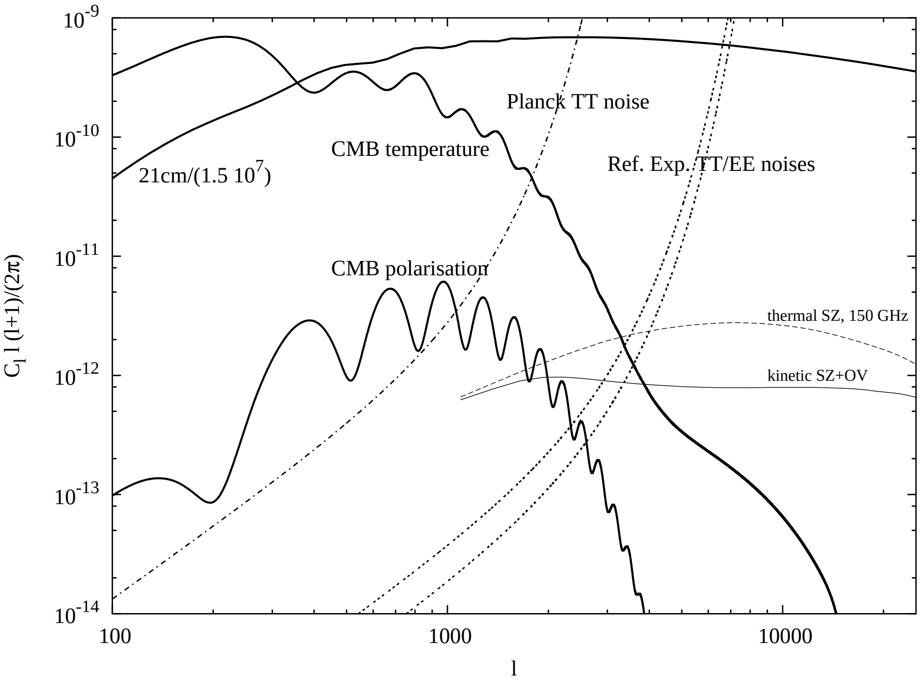

Figure 3.2 CMB temperature and E polarization power spectrum and noise levels of our example experiments: Planck and a futuristic polarized satellite mission (see text for specifications). The 21 cm power spectrum has been rescaled to fit into the same plot. The CMB exhibits more pronounced peaks and a sharp decay on scales $l \simeq 2500$ above which the Sunyaev-Zel'dovich effects become important.

features on the scale of the acoustic oscillations in the pre-recombination baryonic plasma, the primordial signal decays sharply on scales above $l \simeq 2500$. The 21 cm angular power spectrum, in contrast, does not decay very strongly.

We can investigate qualitatively which properties of the power spectrum set the effectiveness of this estimator by looking at the limit $\mathbf{L} \to 0$ (on scales where the noise is small and the lensed power is not systematically larger than the unlensed, $\tilde{\mathrm{C}}_l^{\mathrm{tot}} = \tilde{\mathrm{C}}_l + \mathrm{C}_l^N \simeq \tilde{\mathrm{C}}_l \simeq \mathrm{C}_l$)

$$\begin{aligned}
(L^2 N_L^D)^{-1} &= \frac{1}{L^4}\int \frac{d^2l}{(2\pi)^2}\frac{[\mathbf{L}\cdot\mathbf{l}C_l + \mathbf{L}\cdot(\mathbf{L}-\mathbf{l})C_{L-l}]^2}{2\tilde{\mathrm{C}}_l^{\mathrm{tot}}\tilde{\mathrm{C}}_{L-l}^{\mathrm{tot}}} \\
&\simeq \int \frac{dl}{l}\frac{l^2}{2\pi}(\frac{1}{2}+\frac{1}{2}\alpha+\frac{3}{16}\alpha^2)+ \\
&\quad +L^2\int\frac{d^2l}{(2\pi)^2}\frac{1}{l^2}g(\alpha,\beta,\gamma)
\end{aligned} \tag{3.12}$$

where

$$g(\alpha,\beta,\gamma) = \frac{3(5\beta+8\gamma)+\alpha(\alpha(2+\alpha)(14+5\alpha+20\gamma))}{384}\,, \tag{3.13}$$

and $\alpha \equiv \frac{dlnC_l}{dlnl}$, $\beta = \frac{d^2\mathrm{ln}C_l}{d\mathrm{ln}l^2}$, $\gamma = \frac{d^3\mathrm{ln}C_l}{d\mathrm{ln}l^3}$. The integrand of the first order term has its minimum close to a value $\alpha = -2$, in other words when l^2C_l has no slope. This implies that the CMB with its exponential decay on small scales will have a lower value of N_L^D if those scales are resolved. Integrating Equation 3.12 to the maximum multipole $l_{\max}$ at which $C_l^S > C_l^N$ leads to

$$\begin{align}
(L^2N_L^D)^{-1} &\simeq \frac{1}{2\pi}(\frac{1}{2}+\frac{1}{2}\alpha+\frac{3}{16}\alpha^2)\frac{l_{\max}^2}{2} \tag{3.14}\\
&\quad +\frac{L^2}{2\pi}g(\alpha,\beta,\gamma)\mathrm{ln}(l_{\max}/l_{\min})\,, \tag{3.15}
\end{align}$$

where $l_{\min}$ is the lower bound of the integration. The second term will lead to departures from a constant value of $(L^2N_L^D)$. The scale at which both terms are comparable is

$$L_{\mathrm{comp.}} \simeq \frac{l_{\max}}{\ln(l_{\max}/l_{\min})^{1/2}}\sqrt{\frac{1+\frac{1}{2}\alpha+\frac{3}{16}\alpha^2}{g(\alpha,\beta,\gamma)}}\,. \tag{3.16}$$

Evaluation of this expression shows that for a sloped power spectrum l^2C_l, such as that of the CMB, $L_{\mathrm{comp.}}$ is lower than for a spectrum that is nearly constant, such as that of 21 cm fluctuations. The second order term contributes strongly when the slope is large. If the measured power spectrum has a small slope, as is the case with 21 cm fluctuations, $L^2N_L^D$ can be expected to be nearly constant to the scale $l_{\max}$ where noise becomes important.

In the following section we will generalize the quadratic estimator to a three dimensional observable that is used to reconstruct the lensing field.

The final estimator is then simply the sum of estimators of modes of the wave-vector $k_{\|}$ along the line of sight. This allows one to improve the constraints above those by the CMB especially on small scales by summing over sufficiently many lensing backgrounds.

For our analysis in Section 3.3 we will compute the angular power spectrum of the lensing displacements as the integral over line of sight

$$C_L^{\delta\theta\delta\theta} = \frac{9H_0^4\Omega_0^2}{L(L+1)c^2}\int_0^{\mathcal{D}_s} d\mathcal{D}_l\left(\frac{\mathcal{D}_{ls}}{\mathcal{D}_s\, a(\mathcal{D}_l)}\right)^2 \times \times P_\delta(k=\frac{L}{\mathcal{D}_l},\mathcal{D}_l) \qquad (3.17)$$

over the power spectrum of mass fluctuations. $\mathcal{D}_x$ denote angular diameter distances with $x = l, s$ for lens and source.

We use the halo model fitting function to numerical simulations of [98] to generate nonlinear Λ CDM power spectra as input for the deflection angle integral.

3.2.2 Extension to a three dimensional signal

Different from the CMB, in the case of 21 cm brightness fluctuations we will be able to use multiple redshift information to constrain the intervening matter power spectrum. One could imagine applying this estimator to succesive planes prependicular to the line of sight. However the different planes would be correlated and there is no straightforward criterion to take this correlation into account in establishing the final estimator, since it would depend on redshift, source properties, and during reionization on the mean bubble size and distribution. Instead we will use the knowledge of the three-dimensional information in a different way, dividing the temperature fluctuations in Fourier space in fluctuations $\mathbf{k}_\perp$ perpendicular to the line of sight, and a component $k_{\|}$ in the frequency direction.

We devide a volume on the sky to be probed by a given 21 cm survey into a solid angle $d\Omega$ and a radial coordinate z. Components of wavevectors along the line of sight are described by $k_{\|}$ and those perpendicular to the line of sight are given by the vector $\mathbf{k}_\perp$, which is related to the multipole numbers of the spherical harmonic decomposition on the sky as $\mathbf{l} = \mathbf{k}_\perp\mathcal{D}$, where $\mathcal{D}$ is the angular diameter distance to the volume element we are probing.

Suppose we want to measure a field $I(\mathbf{r})$ with power spectrum $P(\mathbf{k}) = P(\mathbf{k}_\perp, k_{\|})$. Converting $k_\perp$ to angular multipole

$$
\begin{aligned}
I(\mathbf{r}) &= \int \frac{d^3k}{(2\pi)^3} I(\mathbf{k}) e^{i\mathbf{k}\cdot\mathbf{r}} \qquad (3.18)\\
&= \int \frac{d^2l}{(2\pi)^2} \int \frac{dk_\parallel}{2\pi} \frac{I(\mathbf{k}_\perp, k_\parallel)}{\mathcal{D}^2} e^{i(\mathbf{l}\cdot\theta + k_\parallel z)}
\end{aligned}
$$

with $\tilde{I}(\mathbf{l}, k_\parallel) = \frac{I(\mathbf{k}_\perp, k_\parallel)}{\mathcal{D}^2}$ we have

$$
\begin{aligned}
\langle \tilde{I}(\mathbf{l}, k_\parallel) \tilde{I}(\mathbf{l}', k'_\parallel) \rangle &= \delta^D(\mathbf{k} - \mathbf{k}')(2\pi)^3 \frac{P(\mathbf{k}_\perp, k_\parallel)}{\mathcal{D}^4}\\
&= (2\pi)^2 \delta^D(\mathbf{l} - \mathbf{l}')(2\pi)\delta^D(k_\parallel - k'_\parallel) \times\\
&\quad \times \frac{P(\mathbf{k}_\perp, k_\parallel)}{\mathcal{D}^2} \qquad (3.19)
\end{aligned}
$$

where in the second step a factor of $\mathcal{D}^2$ got absorbed into $\delta^D(\mathbf{l} - \mathbf{l}')$ because of $\mathbf{l} = \mathbf{k}_\perp \mathcal{D}$.

Let us discretize the z direction of a real space observed volume with radial length $\mathcal{L}$,

$$
k_\parallel = j\frac{2\pi}{\mathcal{L}}, \quad \delta^D(k_\parallel - k'_\parallel) = \delta_{j_1 j_2}(\frac{\mathcal{L}}{2\pi}) \qquad (3.20)
$$

so that

$$
I(\mathbf{r}) = \int \frac{d^2l}{(2\pi)^2} \sum_j \left(\frac{I(\mathbf{k}_\perp, k_\parallel)}{\mathcal{D}^2\mathcal{L}} \right) e^{i\mathbf{k}\cdot\mathbf{r}} \qquad (3.21)
$$

It makes sense to define

$$
\hat{I} \equiv \frac{I(\mathbf{k}_\perp, k_\parallel)}{\mathcal{D}^2\mathcal{L}} \qquad (3.22)
$$

so that on the sphere we have

$$
\langle \hat{I}_{j_1}(\mathbf{l}_1) \hat{I}^*_{j_2}(\mathbf{l}_2) \rangle = (2\pi^2)\delta^D(\mathbf{l}_1 - \mathbf{l}_2)\delta_{j_1 j_2} \left(\frac{P(k, \mu_k)}{\mathcal{D}^2\mathcal{L}} \right) \qquad (3.23)
$$

where μ_k is the cosine between the wave vector and the line of sight.

We have for the angular power spectrum for separate values of j that (including redshift space distortions)

$$
C_{l,j} \equiv (1 + \mu_k^2)^2 \frac{P(\sqrt{(l/\mathcal{D})^2 + (j\,2\pi/\mathcal{L})^2})}{\mathcal{D}^2\mathcal{L}}, \qquad (3.24)
$$

where P now represents the spherically averaged power spectrum. We have also introduced the notation $C_{l,j}$, denoting the power in a mode with angular component l and radial component $k_j = j\,2\pi/\mathcal{L}$.

We show in the Appendix that because modes with different j can be considered independent, the best estimator can be obtained by combining the individual estimators for separate j's without mixing them (in the sense of making quadratic combinations of them). As long as the IGM is not substantially ionized, the assumption of Gaussianity is justified at the redshifts of interest, $z \simeq 6 - 12$, where non linearites in the gravitational clustering are small on observed scales of several Mpc/h. We find the three dimensional lensing reconstruction noise defined by

$$\langle D(\mathbf{L}) D^*(\mathbf{L}')\rangle = (2\pi)^2 \delta(\mathbf{L} - \mathbf{L}')(C_L^{DD} + N_L^D) \tag{3.25}$$

to be (Equation 3.56 of the Appendix, where e.g. $\mathrm{C}_l \rightarrow \mathrm{P}_l$)

$$\begin{aligned} N_L^D &= \frac{1}{\sum_k \frac{1}{L^2} \int \frac{d^2 l}{(2\pi)^2} \frac{[\mathrm{C}_{l,k} \mathbf{L}\cdot\mathbf{l} + \mathrm{C}_{L-l,k} \mathbf{L}\cdot(\mathbf{L}-\mathbf{l})]^2}{2\tilde{\mathrm{C}}^{\mathrm{tot}}_{l,k} \tilde{\mathrm{C}}^{\mathrm{tot}}_{L-l,k}}} \qquad (3.26) \\ &= \frac{1}{\sum_k N_{L,k}^{-1}} \qquad (3.27) \end{aligned}$$

where in the last line we have just substituted the standard expression, Equation 3.11. Note that analogous to the CMB case, $\tilde{\mathrm{C}}_l^{\mathrm{tot}} = \tilde{\mathrm{C}}_l + C_l^N$, where C_l^N is the noise power spectrum, and $\tilde{\mathrm{C}}_l \simeq \mathrm{C}_l$ in the case of 21 cm fluctuations.

If there is a connected four point function contribution during the epoch of extended HII regions, this will add a term to the variance of the estimator. This will change the weightings A_L as well, and make the estimator suboptimal. We will not try to come up with an estimator that is fully compatible with the non Gaussian signal due to patchy reionization. Instead, in the next section we will conservatively estimate that sensitivities get worse by a factor $\frac{1}{\sqrt{x_H}}$, where x_H is the ionized fraction. In other words, we will effectively be treating the patchy regions as part of the source field which can be masked.

Let us examine the contribution of the components $C_{l,j}$ to the total noise in the estimation of the deflection field. From Equation 3.24 we see that with higher values of the component $k||$, higher values of the three dimensional power spectrum $P(k)$ will translate into each C_l value. But $P(k)$ is monotonically falling on all scales of interest (foregrounds can be expected to contaminate constraints below $\mathrm{k} < 10^{-2}$h/Mpc, the scale of the horizon at matter radiation equality and the turnover of the power spectrum), so that effectively the angular power spectrum amplitude will drop with j towards the noise level. We show this in Figure 3.3 for our bandwidth choice of 5 MHz. Notice that on the smallest resolved scales, $l \simeq 2000 - 5000$ the signal increases slightly as we go from the fundamental $k_{\|} = 0$ to the next higher modes in our line-of-sight decomposition. This is because the radial

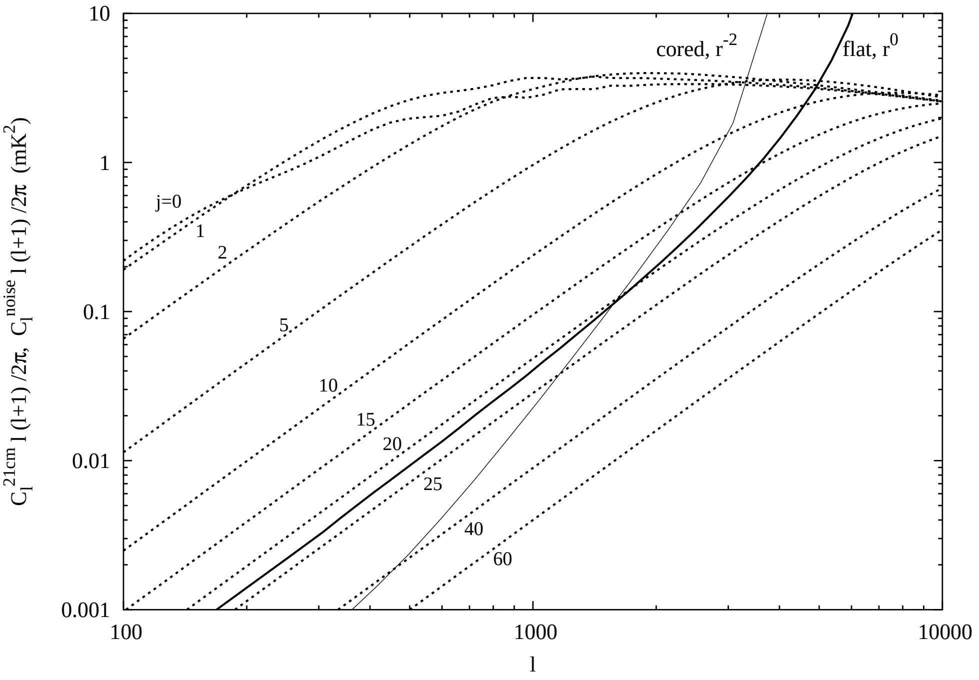

Figure 3.3 The dotted lines show the angular power spectrum for different $k_{\|,j} = j\,2\,\pi/L$, labeled by j. Going to higher values of j, the signal decays quickly below S/N=1 and only the first 15 or so modes contribute to the final lensing estimator. This number depends of course on the thickness of the redshift interval probed (in this case $B = 5\,\mathrm{MHz}$, corresponding to $\Delta z = 0.286$ at $z = 8$). The thick and thin solid curves are for a flat and a cored antenna configuration of SKA (see the text).

component of the power spectrum is increased due to redshift space distortions. Because the smallest resolved angular scales contribute most to the lensing reconstruction, in case of the first few modes in the $k_{\|}$ decomposition this increase overcompensates for the general decay of $C_{l,j}$ on the smallest scales. However overall for each rectangular data field of a given bandwidth we will only be able to sample a limited number of modes $k_{\|}$ with signal-to-noise greater than one, this number being proportional to the frequency depth/bandwidth of the field.

The 21 cm power spectrum and, as we will see in the next section, the noise of the experiment depend on redshift, so we calculate both for volume elements corresponding to the above choice a 5 MHz bandwidth. Beginning at the end of reionization, each volume element contributes to reducing the reconstruction noise while we go along, until the signal-to-noise of the experiment at high redshift becomes negligible. We should wonder whether long wavelength modes overlapping neighbouring volumes lead to an underestimation of the final lensing noise, as we are treating each volume element as uncorrelated. We made a simple test by comparing the N_L of a pair of neighbouring volumes to the sum of N_L's of each element. With our choise of a 5 MHz bandwidth we found no excess information $> 1\%$ in the sum of the seperated field's N_L's, meaning that we can safely neglect those correlations. A multiplicity of those volumes can thus be used to reconstruct each lens just by summing over them.

3.3 Antenna Configuration, Sensitivity Calculation

We have found out in the previous section that in order to measure the lensing signal with redshifted 21 cm fluctuations, we need small angular scale resolution as well as wide redshift coverage. Sensitivity calculations for 21 cm experiments were used in Chapter 2 to constrain cosmological parameters. We give here more details about how this sensitivity is calculated in practice. The sensitivity diminishes quickly with rising foreground temperature at longer wavelengths. The foreground temperature is dominated by galactic synchrotron. To observe at high redshift one needs to compensate for the increased foreground by increasing the collecting area or number of antennas. The angular resolution is improved by increasing the maximal baseline. To have good angular Fourier mode coverage we want all baselines to be represented though. Hence an increase in angular resolution has to be compensated for by increasing the collecting area in order to keep the covering fraction the same. In this section we will discuss various aspects of the first two generations of 21 cm experiments in the context of using them for lensing reconstruction.

A standard approach in radio astronomical measurements (see e.g. the Very Large Array (VLA) [5], the Low Frequency Array LOFAR [6], and the Atacama large millimeter array (ALMA) [7] configurations) is to have a power law decay in the number density of antenna $\mathcal{P} \propto r^{\alpha}$ with radius. This translates into a drop in the number of baselines with separation. The distribution flattens out towards the center to $n(r) = r^0$ simply because antennas cannot be stacked closer to each other than their individual physical size. We found

---

[5] http://www.vla.nrao.edu/

[6] http://www.lofar.org/

[7] http://www.alma.nrao.edu/

in the previous section that the contribution to the weak lensing estimator of $C_{l,j}$ becomes smaller quickly with higher line of sight modes j used. This is just an expression of the fact that what we are interested in is displacements of 21 cm photons perpendicular the line of sight. Lensing reconstruction works through a large number of individual sources being aligned around a big deflector, hence the imaging of small scales is important. For probing small angular scales a flat array profile (that is without a power law decay) may offer an advantage, especially if the observable angular power spectrum falls slightly beyond $l \simeq 1000$ and we want to probe it on those scales.

We can calculate the number of baselines as a function of visibility u from performing the autocorrelation

$$n(u) = \lambda^2 \int d^2r \, \mathcal{P}_{\text{ground}}(\mathbf{r} + \mathbf{x}) \, \mathcal{P}_{\text{ground}}(\mathbf{r}) \tag{3.28}$$

where λ is the observed wavelength and $\mathcal{P}(r)$ denotes the radial profile of the circularly symetric antenna distribution. $\mathbf{x}$ is the vector of seperation of an antenna pair, $\mathbf{x} = \lambda \mathbf{u}$.

The time a particular visibility u is observed, t_u is given by

$$t_u = \frac{A_e t_0}{\lambda^2} n(u) \tag{3.29}$$

where A_e is the effective antenna area and t_0 is the total observing time. We will assume 2000 hours for our calculations, which might be achieveable with planned observatories within a single seasons.

The sensitivity for a given array distribution and specifications can then be calculated as follows. The RMS fluctuation of the thermal noise per pixel of an antenna pair is [99, 22]

$$\Delta T^N(\nu) = \frac{\lambda^2 B T_{\text{sys}}}{A_e \sqrt{Bt}} \tag{3.30}$$

where B is the bandwidth of the observation. For a single baseline the thermal noise covariance matrix becomes

$$C_{ij}^N = \left(\frac{\lambda^2 B T_{\text{sys}}}{A_e} \right)^2 \frac{\delta_{ij}}{B t_{\mathbf{u}}} \tag{3.31}$$

where T_{sys} is the system temperature, dominated by galactic synchrotron radiation (roughly, $T_{\text{sys}} \propto \nu^{-2.55}$ with $T_{\text{sys}} = 440K$ at $z = 6$) and B is the bandwidth of this frequency bin of the total observation. From this we get the noise versus angular multipole number because of $2\pi u = l$ through $\frac{d^2 l}{2\pi} C_l^N = d^2 u C_u^N$.

We are now going to asses the potential of planned 21 cm experiments to measure the lensing imprint using this quadratic estimator. There are currently four major experiments under way, the Mileura Wide Field array (MWA) [100], the primeaval structure telescope [101], the Low Frequency Array (LOFAR) [8] and in the second generation planning stage, the Square Kilometer Array (SKA) [9]. While these projects differ qualitatively in the hardware used, the most crucial difference is their total collecting area. For SKA, current proposals call for 5000 antennas with an individual collecting area of $120m^2$ at $z = 8$ (the effective antenna area depends on wavelength and hence redshift through the square). The collecting areas for MWA and LOFAR/PAST are significantly smaller, 1% and 10% of that of SKA respectively. The optimal array can be designed by distributing the total collecting area over a large number of antennas. The number of baselines goes as N_{ant}^2 which enters into Equation 3.29. In other words, since an array with say ten times the number of dishes (each ten times smaller) as SKA has a ten times larger survey speed, it is better suited for EOR observations. However the computational requirements for the associated correlator unfortunately also scale as N_{ant}^2.

We show the result of our imaging sensitivity calculation for a flat (r^0) to $r_{\rm max} = 1500$ m and a cored (r^0 to $r = 80$ m, then r^{-2} to $r_{\rm max} = 1500$ m) array of SKA antenna in Figure 3.3, together with the hierachy of decreasing angular power spectra as the line of sight component of the 3D measurement $k_\|$ is decreased. We find that a constant radial density of antennas turns out to offer the best compromise between the number of $(\mathbf{k}_\perp, k\|)$ modes that can be probed and overall angular resolution. For a cored r^{-2} distribution for example, the improved sensitivity on those intermediate scales does not compensate for the loss in angular resolution that comes from the lack of large baselines relative to a flat distribution.

For statistical detections of the convergence on the sky a large field of view is desired. The angular power spectrum errors go as $1/\sqrt{f_{\rm sky}}$. Hence it is advantageous to distribute the same total collecting area in many smaller antennas, thus increasing the speed of the survey. On the down-side, it is more difficult to scale small dipole like antenna to high freqencies (below the redshift of reionization), where other interesting science with 21 cm emitters lies (see e.g. [102]).

---

[8] http://www.lofar.org

[9] http://www.skatelescope.org/

3.4 Results and a Comparison with the CMB

In this section we will discuss a specific configuration that seems likely within reach of the second generations of EOR observatories and calculate our three dimensional lensing estimator for a particular reionization scenario. This way we will gauge the prospects of lensing reconstruction using redshifted 21 cm fluctuations and how they relate to using other backgrounds.

The prospects of lensing reconstruction with the quadratic estimator have been explored in depth by [95, 96, 103, 104] in the context of the CMB. A systematic problem with temperature is that it is contaminated by Doppler related anisotropies (the kinetic Sunyaev-Zel'dovich effect [105]) which share the same frequency dependence as the primordial CMB. [104] showed that this contamination is significant, and might eventually have to be taken care of by masking thermal SZ detected areas from the map. It is found that using the CMB polarization an order of magnitude improvement over temperature reconstruction might be possible [96]. On scales where the B component of polarization can be resolved (above $l \simeq 100$ this component is almost entirely produced by gravitational lensing rotation of the E modes), with iterative likelihood techniques astonishingly there may be no limit at all to delensing [106], on angular scales where the B modes can be resolved.

As discussed in the previous section (Equation 3.12), the effectiveness of lensing reconstruction depends on the slope of the power spectrum, and the 21 cm background suffers a disadvantage compared to the CMB in that there is no damping tail and the traces of baryonic oscillations are comparatively small. On the other hand the lack of an exponential decay in the 21 cm fluctuations suggests that these can be used for reconstruction out to smaller scales. Figure 3.2 shows CMB strengths and limitations in comparison to the shape of the 21 cm power spectrum (which has been rescaled to fit in the same plot).

The damping tail of the CMB at scales $l \geq 3000$ leads to a limit for the deflection scales $l \simeq 1200$ that can be probed using quadratic techniques [96]. The 21 cm power spectrum does not decrease substantially at small scales, the only theoretical limit being set by the Jeans scale.

Figure 3.4 shows a rather constant shape of $L^2 N_L$ versus the angular multipole of the lensing field L. This is essentially a consequence of the rather flat shape of the 21 cm power spectrum, as we discussed following Equation 3.12: in this case we would expect N_L to not change much up to scales where the signal becomes comparable to the noise of the experiment. This property will allow us to image the lensing field down to small scales. We also show in the same figure a plot of the temperature based CMB lensing reconstruction based on the Planck satellite experimental specifications.

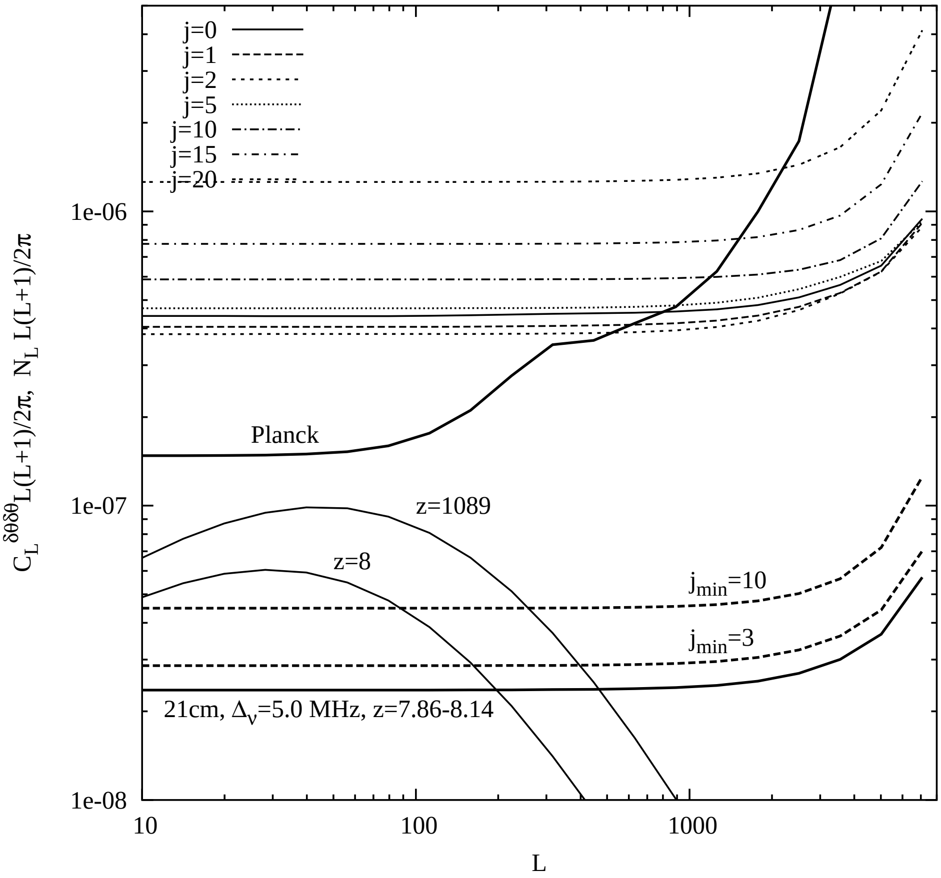

Figure 3.4 Lensing reconstruction noise N_L for one redshift interval centered at $z = 8$ corresponding to a bandwidth of 5 MHz. The curves labeled 'z=8' and 'z=1089' are the displacement field power spectra for 21 cm and CMB as source respectively. The thick solid curves labeled 'Planck' and '21 cm' are the lensing reconstruction noises we find. The 21 cm noise is based on combining all $k_{\|}$ modes. The thin lines labeled 'j=0-20' on the other side are the results for individual $k_{\|}$-modes. We see that from this redshift range alone the combined temperature and polarization information of Planck can be beaten. The necessity to substract foregrounds lessens the constraint from 21 cm somewhat. They effectively render the first few $k_{\|}$ modes useless for the reconstruction, see the text. The resulting noise levels are shown in the thick dashed curves labeled $j_{\min} = 3$ and $j_{\min} = 10$, for a less and more conservative assumption about the complexity of foreground contamination respectively.

The CMB power spectrum sensitivity is given in terms of detector noise w^{-1} and beam σ_{FWHM} [107]

$$C_l^{\mathrm{noise}} = w^{-1} e^{l(l+1)\sigma^2_{\mathrm{FWHM}}/8ln2} \tag{3.32}$$

We assume two types of experiments, Planck, with $w^{-1/2} = 27\mu\mathrm{K} - \mathrm{arcmin}$ at 5 arcmin angular resolution, and a futuristic experiment with noise level $w^{-1/2} = 3\mu\mathrm{K} - \mathrm{arcmin}$ at an angular resolution of 3 arcmin. For the polarization we use as usual that $w_P^{-1/2} = \sqrt{2} w_T^{-1/2}$ if all detectors are polarized. We include the noise power spectra for Planck temperature, and for polarization and temperature measurements of our reference CMB experiment in Figure 3.2.

We calculate the minimum variance lensing noise level following [94]

$$N_{\mathrm{mv}}(L) = \frac{1}{\sum_{\alpha,\beta} (\mathrm{N}^{-1}(L))_{\alpha\beta}} \tag{3.33}$$

where α and β run over T, E, and B temperature and polarization fluctuations. The noise levels $N(\mathbf{L})_{\alpha\beta}$ take on different forms depending on whether α and β are equal (the BB term is generally considered to have vanishingly small signal to noise), or different, $\alpha\beta = \theta E$, θB, and EB.

We compare Planck constraints to 21 cm observation sensitivities for the deflection angle power spectrum that we get from observing a 5 MHz slice at redshift 8 in Figure 3.4. The corresponding redshift depth is $\Delta z = 0.5$. If we want to gather all the information accessible to us from fluctuations in the 21 cm brightness temperature, we can add up a number of redshift intervals with the constant bandwidth, employing the whole redshift range covered by the observation. We find that even when using only a fraction of the entire data volume available in 21 cm, $\Delta z \simeq 0.3$, Planck's combined temperature and polarization potential for doing lensing reconstruction can be beaten with the three dimensional generalization of the quadratic estimator. If we want to use a larger redshift range for the 21 cm reconstruction, we need to take into account the redshift evolution in the power spectrum of matter fluctuations, and that of the ionization fraction. For an SKA type experiment in the optimized configuration we use, this range is $z = 6 - 12$, at higher redshifts the sensitivity becomes too small for imaging, the limitation being set by the increased temperature of the foreground. Note that if reionization completes earlier than $z = 12$ lensing reconstruction using 21 cm will be impossible with SKA. In our particular reionization scenario we achieve a constraint at $L \approx 1000$ about ten times as good (i.e. an N_L ten times lower) for the lensing reconstruction, in comparison to our reference CMB experiment with 3 arcminute resolution and a noise level of $w^{-1/2} = 3\mu\mathrm{K} - \mathrm{arcmin}$. We show this result in Figure 3.5, together with nonlinear/linear lensing field power spectra. The Figure also shows (in the thick dashed curve) the increase in noise when our patchy model is used for the range 6-8 in place of an extension of the neutral phase. This increased noise relative to the case of probing the pre-reionization IGM has two reasons: first, as shown in Figure 3.1, the fluctuation level of the 21cm signal is decreased on the smallest resolved scales, making this source less valuable for lensing reconstruction. Secondly, the connected four-point function contribution adds a non Gaussian term to the noise covariance matrix of the power spectrum, acting as a sample variance term in correlating different band-powers. We treated this term in a simplified manner by assuming that the majority of bubble features arises on scales well above the resolution scale of SKA, about 1'. Then the bubbles can be resolved and masked when establishing the final estimator. The mask increases the sample variance simply as $\delta C_l^* = \frac{1}{\sqrt{x_H}}\delta C_l$, where x_H is the neutral fraction at this redshift. Our estimate of the lensing reconstruction noise for the patchy epoch is conservative, in that power in the regions outside the bubble mask will not be suppressed, however we use the global average power spectrum which is suppressed by x_H^2. For completeness we also show (in the thick dotted curve) the total lensing reconstruction noise if we only use the neutral regime above $z = 8$ in the analysis.

Because of the multiple background information, in reconstructing the deflection field we can approach the limit imposed by the finite angular resolution of an experiment (determined by its maximum baseline). In Figure 3.6 we show contours for the maximum lensing deflection field multipole L that can be probed as a function of the maximum baseline and the total collecting area. For the r^0 array there exists an optimal $r_{\max}$ which depends on the amplitude of the power spectrum and the total collecting area. If one uses a wider radius while keeping the number of dishes constant, the noise level increases on all angular scales, so although one might be able to use slightly larger multipoles (smaller scales) for the reconstruction, many modes of our hierarchy do not enter the estimator. On the other hand, if one decreases the array size, thus making the antenna distribution denser, this leads to a lower noise level on relatively large scales, while no baselines exist anymore to measure the small scales that are crucial for the reconstruction.

We find that after gathering 2000 hours of data, a very ambitious experiment with four times the collecting area of SKA (for which $A_{\mathrm{coll.,z=8}} = 0.6\mathrm{km}^2$) could detect lensing at scales beyond $L = 6000$, which is comparable to the scale of galaxy clusters.

We will extend considerations to statistical detections of the deflection power spectrum. Because the geometrical ratio $\frac{D_l D_{ls}}{Ds}$ is larger for the CMB

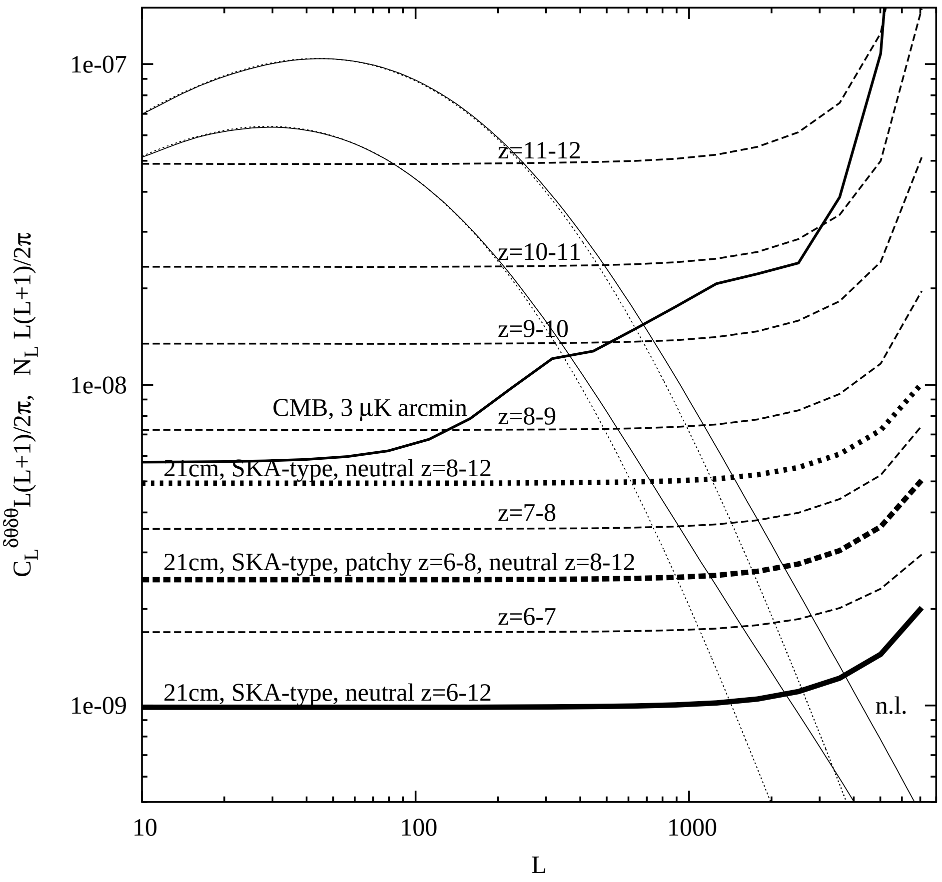

Figure 3.5 Lensing reconstruction noise with an experiment that has the total collecting area of SKA, if the IGM is not ionized during the regime z=6-12, shown in the thick line at bottom. The individual contributions from redshift intervalls are shown in the dashed lines. The noise levels are compared to the deflection angle power spectrum, where the solid (dotted) lines are for the nonlinear (linear) density fluctuations at z=8 and z=1089. On scales of $L = 1000$ and above, our method might be able to achieve an order of magnitude lower total noise levels than what is possible with the CMB quadratic estimator technique (shown in the other thick solid line). Here the smallest angular scale reconstructed using EOR fluctuations is $L_{\rm max} = 2250$. The thick dashed line shows the increased noise level if reionization is inhomogeneous during $z = 6 - 8$, calculated in the way detailed in the text. Finally the thick dotted curve gives the total noise level if the regime $z = 6 - 8$ is not used at all in the analysis.

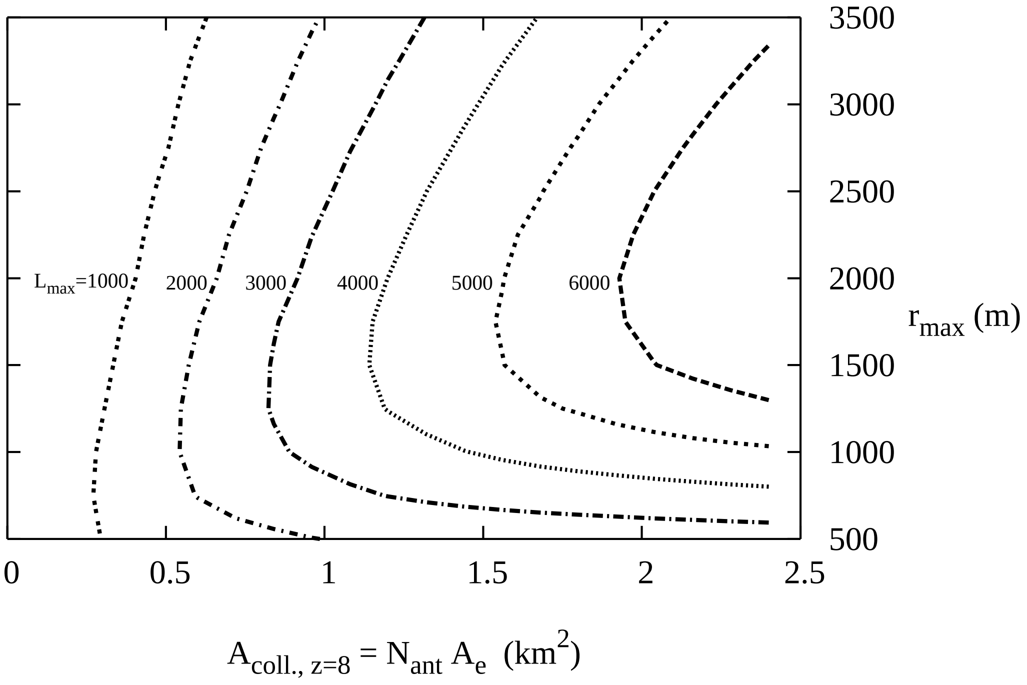

Figure 3.6 Contour plot of L_{max}, the largest displacement field multipole probed. From this Figure one can infer the optimal array radius (assuming here an r^0 distribution of antennas) that one should choose given a total collecting area A_{coll}. It also shows that if one would have four times the collecting area of SKA (for which $A_{\mathrm{coll.,z=8}} = 0.6\mathrm{km}^2$), or if one were to observe four times longer on the same patch of the sky, very high multipoles could be probed.

(qualitatively the bulk of lensing happens at angular diameter distances that are closer to the middle between the observer and the CMB), the respective deflection angle power spectrum has a higher amplitude. On the other hand the 21 cm experiment will have the advantage of measuring multiple planes so that at comparable angular resolution smaller errors in the angular power spectrum at high L can in principle be achieved.

In [92] it was proposed that 21 cm reconstruction of the lensing power spectrum might be helpful in getting at B mode polarization from primordial gravity waves. Since lensing partially converts E (gradient) polarization into a curl component, this secondary signal swamps the B modes from a possible inflationary tensorial fluctuation background. The problem is that at significantly lower redshifts than the last scattering surface, only part of the lensing structure encountered by the CMB photons is traced, leading to a delensing bias if 21 cm fluctuations are used. One would have to observe at high enough redshifts if one were to compete with CMB polarization experiments. Indeed the authors find that in principle with an ultra sensitive experiment (for instance space based) observing at redshift 30 one might be able to beat CMB limits beyond the iterative likelihood approach of [106, 90]. To achieve this one would need 1-2 orders of magnitude more collecting area than what is planned for the second generation of observatories, hence this application is beyond the scope of this thesis.

A characteristic of 21 cm fluctuations is that the distance between observer and lens is a larger fraction of the whole distance to the source, so one would imagine that if the same number of multipoles are probed with 21 cm as with the CMB (by having a lower noise level), one would obtain different constraints on dark energy. We show this in Figure 3.7, where the ratio

$$\Gamma_{\Omega_\Lambda}(L) = \frac{\Omega_\Lambda}{C_L^{DD}} \frac{\partial C_L^{DD}}{\partial \Omega_\Lambda} \tag{3.34}$$

is plotted against L. The quantity measured shows how well the dark energy density can be constrained by using information from a given angular scale. Its value gives the constraint that can be put on the parameter from this scale if there were no degeneracies with other unknowns. We see that when the same range of angular scales are resolved, the 21 cm fluctuations fair somewhat better in constraining the dark energy density Ω_Λ.

The noise for estimation of bandpowers is reduced by averaging over $\mathbf{L}$ directions in a band of width ΔL

$$\Delta C_L^{DD} = \sqrt{\frac{2}{(2L+1)\Delta L f_{\rm sky}}} [C_L^{DD} + N_{\rm mv}(L)] \, . \tag{3.35}$$

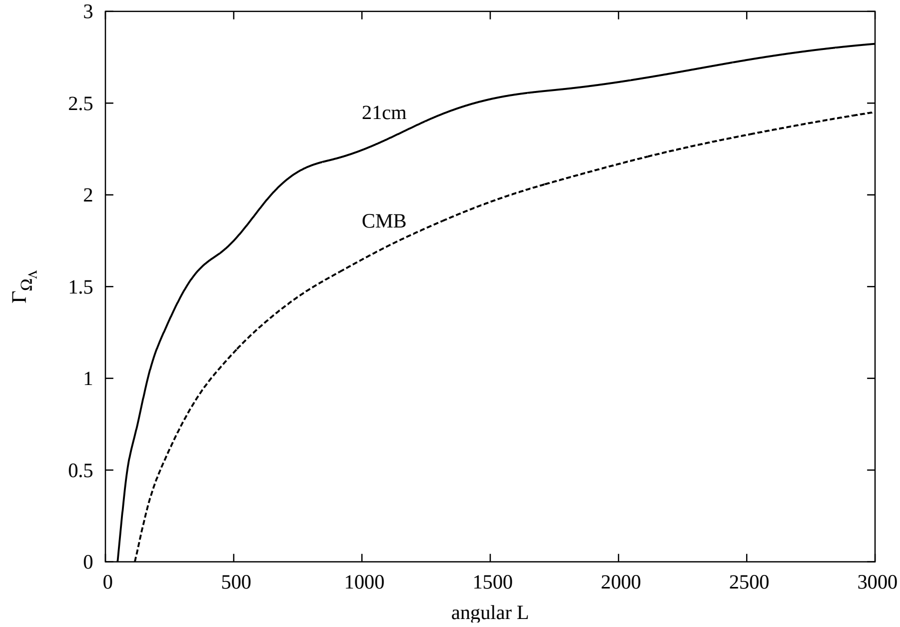

Figure 3.7 Plot of the parameter Γ defined in the text. This suggests that 21 cm fluctuations are better suited in principle to measure the value of the cosmological constant than the CMB, assuming that the same number of angular modes can be probed.

A comparison between the polarized reference CMB experiment and an experiment with SKA's sensitivity is shown in Figure 3.8 where we assumed a sky coverage of 0.8 for the CMB experiment and a smaller field of view 0.08 for the 21 cm experiment. We plot the sample variance error ('S') and sample variance plus noise ('S+N'). Polarized CMB experiments suffer from foreground contamination [7], so our reference experiment should be an idealized limit. The sky coverage of the 21cm experiment might be achievable within one year of observation with an MWA type experiment that has the same collecting area as SKA but a ten times higher survey speed. Using fluctuations in the 21 cm background, we should be able to measure the deflection power spectrum to much higher multipoles, $l > 10000$ for this type of experiment, than what will ultimately be possible using the CMB quadratic estimator technique, even if the latter observes on a much larger part of the sky (notice also that 21 cm experiments should be able to observe separate fields in consecutive seasons). The requirement of a combination of large collecting area and high survey speed makes this an ambitious project.

Finally we would like to estimate the effect foregrounds will have on the estimation of the lensing field suggested here. As pointed out by [21, 22],

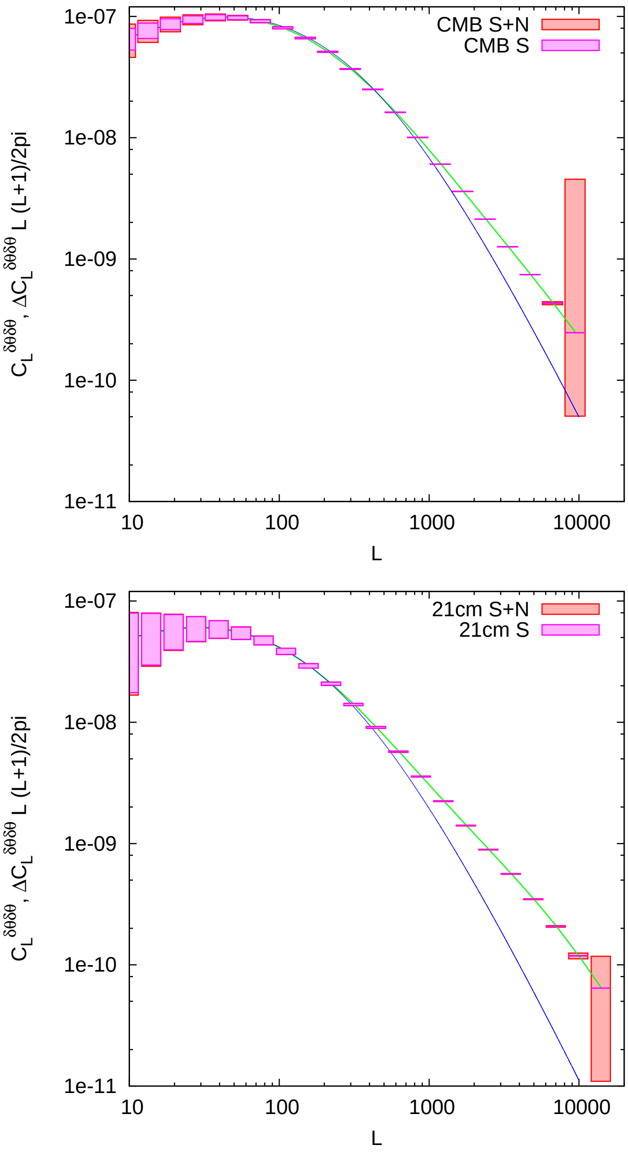

Figure 3.8 Displacement field power spectra and sample variance (‘S’) and noise (‘N’) errors. An SKA like experiment might be suited to probe a large dynamical range in the displacement field. The displacement field angular power spectrum with errorbars on the left is for our reference CMB experiment at $f_{\rm sky} = 0.8$ and the curves on the right are for 21 cm redshift 6-12 lensing reconstruction using the ”MWA50k” (same collecting area but 10 times higher survey speed than SKA) with $f_{\rm sky} = 0.08$.

fluctuations in the gas at high redshift can be seperated against the much brighter foregrounds (the main source of confusion being galactic and extra-galactic synchrotron), because the former vary rapidly, the latter slowly in frequency. This can be done by fitting various smooth functions to the signal. [108], [47], and [80] suggest quadratic or cubic polynomials, but also more complicated functions such as Chebychew polynomials have been proposed. [80] show that this will practically make the first few wavevector modes in the line of sight direction unusable. The exact number of modes that can be used depends of course on the nature of foregrounds, the bandwidth, and the technique of fitting.

On the positive side once a model for foregrounds is given, we can implement this pretty straightforwardly within our formalism by discarding the first few modes $k_{\|}$ (depending on the order of fitting polynomial) in the hierarchy of C_l's, compare Figure 3.3. It is to be expected that a large number of modes still will contribute to the final noise level. This is quantified in Figure 3.4 where the sum $N_L^{-1} = 1/\sum_{k_j > j_{\min}} N_{L,k_j\mathcal{L}/(2\pi)}$ is plotted for the two cases $j_{\min} = 3, 10$ meaning that the first 3/10 modes have been discarded in the analysis. The resulting noise levels (short dashed lines) are somewhat higher than the solid line that was obtained from assuming no foregrounds.

3.5 Conclusions and Outlook

In this chapter we have extended the quadratic estimator formalism to use a three dimensional signal as lensing background. 21 cm fluctuations from neutral hydrogen prior and during the epoch of reionization contain an enormous amount of data points. The correlations induced by lensing into this signal can be used to probe the intervening matter fluctuations either on a individual object basis, or statistically to for example probe dark energy models. To describe fluctuations in the neutral fraction, we used an analytic model for the morphology of HII regions to demonstrate the applicability of our method to this regime.

Our estimator should be complete as long as non linearities in the signal (e.g. due to the bubbles) are small. The bulk of the information we use is coming from the neutral phase.

The first generation of experiments is likely not going to be able to image the angular fluctuations in 21 cm needed to measure the lensing effect. However we arrive at good constraints by employing current specifications of the SKA with a flat antenna distribution.

In comparison with the CMB, 21 cm fluctuations have a rather featureless scale invariant unlensed spectrum which leads to a smaller lensing effect. This can be compensated for by using multiple redshift information when probing each individual lens surface. The CMB quadratic estimator sensitivity can actually be beaten this way, for example with an SKA type experiment.

Another possibility would be to combine 21 cm lensing reconstruction with that from other observables, such as the CMB. Similar to combining the latter with galaxy shear surveys, this will improve the constraints on the mass/energy budget or geometry of the universe significantly.

If ambitions in the community of observational and theoretical cosmologists increase in the years to come, and third generation experiments will be scheduled, a new prospect would be the measurement of polarized 21 cm emission. [109] find that Thomson scattering of the quadrupole produced by the reionized universe produces the largest effect and similar to the gains by using CMB polarization, this could make the method suggested in this chapter, the three dimensional form of the quadratic estimator, even more promising.

Larger collecting areas and longer observation times also promise to allow 21 cm lensing reconstruction to map out the gravitational potential of individual galaxy clusters. We will attempt to address this topic in a future work.

3.6 Appendix A: Quadratic estimator applied to a three dimensional observable

We want to observe the three dimensional field $I(\theta, z)$. We assume weak lensing, i.e. that

$$\tilde{\mathrm{I}}(\theta, z) = \mathrm{I}(\theta, z) + \delta\theta \cdot \nabla_\theta \mathrm{I}(\theta, z) + ... \tag{3.36}$$

where $\tilde{\mathrm{I}}(\theta, z)$ is the lensed, $\mathrm{I}(\theta, z)$ the unlensed field. The Fourier transform of this expression is

$$\begin{aligned}\tilde{\mathrm{I}}(\mathbf{l}, k) &= \mathrm{I} + \int \frac{d^2l'}{(2\pi)^2}(\delta\theta(\mathbf{l}-\mathbf{l}') \cdot i\mathbf{l})\mathrm{I}(\mathbf{l}', k) & (3.37)\\ &= \mathrm{I}(\mathbf{l}, k) - \int d^2l' \mathrm{I}(\mathbf{l}', k)\phi(\mathbf{l}-\mathbf{l}')(\mathbf{l}-\mathbf{l}') \cdot \mathbf{l}' & (3.38)\end{aligned}$$

where we have used that $\delta\theta(\mathbf{L}) = i\mathbf{L}\phi(\mathbf{L})$. We are looking for a quadratic estimator $\Phi(\mathbf{L})$ for $\phi(\mathbf{L})$, i.e. of the form

$$\Phi(\mathbf{L}) = \int \frac{d^2l}{(2\pi)^2} \int \frac{dk_1}{2\pi} \int \frac{dk_2}{2\pi} F(\mathbf{l}, k_1, k_2, \mathbf{L}) I(\mathbf{l}, k_1) I(\mathbf{L}-\mathbf{l}, k_2) \tag{3.39}$$

(notice that $F(\mathbf{l}, k_1, k_2, \mathbf{L}) = F(\mathbf{l}, k_2, k_1, \mathbf{L})$). Because $\delta\Phi(\mathbf{L}) = \delta\Phi^*(-\mathbf{L})$ it can also be shown that

$$F(\mathbf{l}, k_1, k_2, \mathbf{L}) = F^*(-\mathbf{l}, -k_1, -k_2, -\mathbf{L}) \tag{3.40}$$

We want to find F such that it minimizes the variance of $\Phi(\mathbf{L})$ under the condition that its ensemble average recovers the lensing field, $\langle\Phi(\mathbf{L})\rangle_{\mathrm{I}} = \phi(\mathbf{L})$. This becomes (to first order in ϕ)

$$\begin{aligned}
\langle\Phi(\mathbf{L})\rangle_{\mathrm{I}} &= \int \frac{d^2l}{(2\pi)^2}\int\frac{dk_2}{2\pi}\int\frac{dk_2}{2\pi}F(\mathbf{l},k_1,k_2,\mathbf{L})\left[-\langle \mathrm{I}(\mathbf{l},k_1)\int\frac{d^2l}{(2\pi)^2}'\mathrm{I}(\mathbf{l}',k_2)\phi(\mathbf{L}-\mathbf{l}-\mathbf{l}')\times\right.\\
&\left.\times(\mathbf{L}-\mathbf{l}-\mathbf{l}')\cdot\mathbf{l}'\rangle - \langle \mathrm{I}(\mathbf{L}-\mathbf{l},k_2)\int\frac{d^2l}{(2\pi)^2}'\mathrm{I}(\mathbf{l}',k_1)\phi(\mathbf{l}-\mathbf{l}')(\mathbf{l}-\mathbf{l}')\cdot\mathbf{l}'\rangle\right]\\
&= -\int \frac{d^2l}{(2\pi)^2}\int\frac{dk_1}{2\pi}\int\frac{dk_2}{2\pi}F(\mathbf{l},k_1,k_2,\mathbf{L})\left[\int\frac{d^2l}{(2\pi)^2}'(2\pi)^2\delta(\mathbf{l}+\mathbf{l}')(2\pi)\delta(k_1+k_2)\mathrm{P}_{l,k}\times\right.\\
&\left.\times\phi(\mathbf{L}-\mathbf{l}-\mathbf{l}')(\mathbf{L}-\mathbf{l}-\mathbf{l}')\cdot\mathbf{l}' + \int\frac{d^2l}{(2\pi)^2}'(2\pi)^2\delta(\mathbf{L}-\mathbf{l}+\mathbf{l}')(2\pi)\delta(k_1+k_2)\mathrm{P}_{L-l,k}\phi(\mathbf{l}-\mathbf{l}')(\mathbf{l}-\mathbf{l}')\cdot\mathbf{l}'\right]\\
&= -\int \frac{d^2l}{(2\pi)^2}\int\frac{dk_1}{2\pi}\int\frac{dk_2}{2\pi}F(\mathbf{l},k_1,k_2,\mathbf{L})(2\pi)\delta(k_1+k_2)\left[\mathrm{P}_{l,k}\phi(\mathbf{L})\mathbf{L}\cdot(-\mathbf{l})+\mathrm{P}_{L-l,k}\phi(\mathbf{L})\mathbf{L}\cdot(-(L-l))\right]\\
&= \int \frac{d^2l}{(2\pi)^2}\int\frac{dk_1}{2\pi}\int\frac{dk_2}{2\pi}F(\mathbf{l},k_1,k_2,\mathbf{L})(2\pi)\delta(k_1+k_2)\left[\mathrm{P}_{l,k}\phi(\mathbf{L})\mathbf{L}\cdot\mathbf{l}+\mathrm{P}_{L-l,k}\phi(\mathbf{L})\mathbf{L}\cdot(\mathbf{L}-\mathbf{l})\right], \qquad (3.41)
\end{aligned}$$

where e.g. $\mathrm{P}_{l,k}$ is the power in a mode with angular component l and radial component k. With the requirement that $\langle\Phi(\mathbf{L})\rangle_{\mathrm{I}} = \phi(\mathbf{L})$ this leads to the normalization condition

$$\int \frac{d^2l}{(2\pi)^2}\int\frac{dk_1}{2\pi}\int\frac{dk_2}{2\pi}F(\mathbf{l},k_1,k_2,\mathbf{L})(2\pi)\delta^D(k_1+k_2)\left[\mathrm{P}_{l,k}\mathbf{L}\cdot\mathbf{l}+\mathrm{P}_{L-l,k}\mathbf{L}\cdot(\mathbf{L}-\mathbf{l})\right] = 1 \qquad (3.42)$$

The next step is to minimize the variance

$$\begin{aligned}
\langle||\Phi(\mathbf{L})||^2\rangle_{\tilde{\mathrm{I}}} &= \int \frac{d^2l}{(2\pi)^2}\int\frac{dk_1}{2\pi}\int\frac{dk_2}{2\pi}\int\frac{d^2l}{(2\pi)^2}'\int\frac{dk_1}{2\pi}'\int\frac{dk_2}{2\pi}' F(\mathbf{l},k_1,k_2,\mathbf{L})F^*(\mathbf{l}',k_1',k_2',\mathbf{L}')\times \\
&\qquad \times\langle\tilde{\mathrm{I}}(\mathbf{l},k_1)\tilde{\mathrm{I}}(\mathbf{L}-\mathbf{l},k_2)\tilde{\mathrm{I}}(\mathbf{l}',k_1')\tilde{\mathrm{I}}(\mathbf{L}-\mathbf{l}',k_2')\rangle \\
&= \int\int\int\int\int\int F(\mathbf{l},k_1,k_2,\mathbf{L})F^*(\mathbf{l}',k_1',k_2',\mathbf{L}')(2\pi)^2\delta(\mathbf{l}-\mathbf{l}')(2\pi)\delta(k_1-k_1')\tilde{\mathrm{P}}^{\mathrm{tot}}_{l,k_1}\times \\
&\qquad \times(2\pi)^2\delta(\mathbf{l}'-\mathbf{l})(2\pi)\delta(k_2-k_2')\tilde{\mathrm{P}}^{\mathrm{tot}}_{L-l,k_2} \\
&\quad +\int\int\int\int\int\int F(\mathbf{l},k_1,k_2,\mathbf{L})F^*(\mathbf{l}',k_1',k_2',\mathbf{L}')(2\pi)^2\delta(\mathbf{l}-\mathbf{L}+\mathbf{l}')(2\pi)\delta(k_1-k_2')\tilde{\mathrm{P}}^{\mathrm{tot}}_{l,k_1}\times \\
&\qquad \times(2\pi)^2\delta(\mathbf{L}-\mathbf{l}-\mathbf{l}')(2\pi)\delta(k_2-k_1')\tilde{\mathrm{P}}^{\mathrm{tot}}_{L-l,k_2} \\
&= \int\frac{d^2l}{(2\pi)^2}\int\frac{dk_1}{2\pi}\int\frac{dk_2}{2\pi}(2\pi)^2\delta(0)F(\mathbf{l},k_1,k_2,\mathbf{L})F^*(\mathbf{l}',k_1',k_2',\mathbf{L}')\tilde{\mathrm{P}}^{\mathrm{tot}}_{l,k_1}\tilde{\mathrm{P}}^{\mathrm{tot}}_{L-l,k_2} \\
&\quad +\int\frac{d^2l}{(2\pi)^2}\int\frac{dk_1}{2\pi}\int\frac{dk_2}{2\pi}(2\pi)^2\delta(0)F(\mathbf{l},k_1,k_2,\mathbf{L})F^*(\mathbf{L}-\mathbf{l}',k_2',k_1',\mathbf{L}')\tilde{\mathrm{P}}^{\mathrm{tot}}_{l,k_1}\tilde{\mathrm{P}}^{\mathrm{tot}}_{L-l,k_2} \qquad (3.43)
\end{aligned}$$

but from 3.39 we see with the substitution $\mathbf{L}-\mathbf{l}\rightarrow\mathbf{l}$ that $F^*(\mathbf{L}-\mathbf{l},k_2,k_1,\mathbf{L}) = F^*(\mathbf{l},k_1,k_2,\mathbf{L})$ hence

$$\langle||\Phi(\mathbf{L})||^2\rangle = 2(2\pi)^2\delta(0)\int\frac{d^2l}{(2\pi)^2}\int\frac{dk_1}{2\pi}\int\frac{dk_2}{2\pi}F(\mathbf{l},k_1,k_2,\mathbf{L})F^*(\mathbf{l},k_1,k_2,\mathbf{L})\tilde{\mathrm{P}}^{\mathrm{tot}}_{l,k_1}\tilde{\mathrm{P}}^{\mathrm{tot}}_{l,k_2}\,. \qquad (3.44)$$

Both real and imaginary part of $||F||^2 = F_R^2 + F_I^2$ contribute to this variance, however the condition for the minimization will only pick out the real part. The solution is found by minimizing the function

$$\langle||\Phi(\mathbf{L})||^2\rangle - A_R\times(\,\text{Equation}\,3.42) \qquad (3.45)$$

with respect to F, where A_R is a Lagrangian multiplier. In steps,

$$\frac{\partial(\,\text{Eq.}\,3.42)}{\partial F(\mathbf{l},k_1,k_2,\mathbf{L})} = A_R\frac{d^2l}{(2\pi)^2}\frac{dk_1}{2\pi}\frac{dk_2}{2\pi}(2\pi)\delta^D(k_1+k_2)[\mathrm{P}_{l,k}\mathbf{L}\cdot\mathbf{l}+\mathrm{P}_{L-l,k}\mathbf{L}\cdot(\mathbf{L}-\mathbf{l})] \qquad (3.46)$$

and

$$\frac{\partial\langle||\Phi(\mathbf{L})||^2\rangle}{\partial F(\mathbf{l},k_1,k_2,\mathbf{L})} = 2(2\pi)^2\delta(0)\frac{d^2l}{(2\pi)^2}\frac{dk_1}{2\pi}\frac{dk_2}{2\pi}2F_R(\mathbf{l},k_1,k_2,\mathbf{L})\tilde{\mathrm{P}}^{\mathrm{tot}}_{l,k_1}\tilde{\mathrm{P}}^{\mathrm{tot}}_{L-l,k_2} \tag{3.47}$$

so

$$F_R(\mathbf{l},k_1,k_2,\mathbf{L}) = A_R(2\pi)\delta^D(k_1+k_2)\frac{[\mathrm{P}_{l,k}\mathbf{L}\cdot\mathbf{l} + \mathrm{P}_{L-l,k}\mathbf{L}\cdot(\mathbf{L}-\mathbf{l})]}{\tilde{\mathrm{P}}^{\mathrm{tot}}_{l,k_1}\tilde{\mathrm{P}}^{\mathrm{tot}}_{L-l,k_2}} \tag{3.48}$$

and by inserting this into the normalization condition 3.42 we get that

$$A_R = \frac{1}{\sum_k\int\frac{d^2l}{(2\pi)^2}\frac{[\mathrm{P}_{l,k}\mathbf{L}\cdot\mathbf{l}+\mathrm{P}_{L-l,k}\mathbf{L}\cdot(\mathbf{L}-\mathbf{l})]^2}{\tilde{\mathrm{P}}^{\mathrm{tot}}_{l,k_1}\tilde{\mathrm{P}}^{\mathrm{tot}}_{L-l,k_2}}}\,. \tag{3.49}$$

By using Equation 3.48 we find that the variance becomes

$$\begin{aligned}
\langle||\Phi(L)||^2\rangle &= 2(2\pi)^2\delta(0)\int\frac{d^2l}{(2\pi)^2}\int\frac{dk_1}{2\pi}\int\frac{dk_2}{2\pi}\tilde{\mathrm{P}}^{\mathrm{tot}}_{l,k_1}\tilde{\mathrm{P}}^{\mathrm{tot}}_{L-l,k_2}F_R^2 &(3.50)\\
&= 2(2\pi)^2\delta(0)A_R^2\int\frac{d^2l}{(2\pi)^2}\int\frac{dk_1}{2\pi}\int\frac{dk_2}{2\pi}[(2\pi)\delta(k_1+k_2)]^2\frac{[\mathrm{P}_{l,k}\,\mathbf{L}\cdot\mathbf{l}+\mathrm{P}_{L-l,k}\,\mathbf{L}\cdot(\mathbf{L}-\mathbf{l})]^2}{\tilde{\mathrm{P}}^{\mathrm{tot}}_{l,k}\,\tilde{\mathrm{P}}^{\mathrm{tot}}_{L-l,k}} &(3.51)
\end{aligned}$$

Using $(2\pi)\delta^D(0) = \frac{2\pi}{dk}$ and $\int\frac{dk}{2\pi}\frac{2\pi}{dk}\rightarrow\sum_k$, this becomes

$$\begin{aligned}
\langle||\Phi(L)||^2\rangle &= 2(2\pi)^2\delta(0)A_R^2\sum_k\int\frac{d^2l}{(2\pi)^2}\frac{[\mathrm{P}_{l,k}\,\mathbf{L}\cdot\mathbf{l}+\mathrm{P}_{L-l,k}\,\mathbf{L}\cdot(\mathbf{L}-\mathbf{l})]^2}{\tilde{\mathrm{P}}^{\mathrm{tot}}_{l,k}\,\tilde{\mathrm{P}}^{\mathrm{tot}}_{L-l,k}}\\
&= 2(2\pi)^2\delta(0)A_R^2\frac{2}{A_R}\\
&= (2\pi)^2\delta(0)\frac{1}{\sum_k\int\frac{[\mathrm{P}_{l,k}\mathbf{L}\cdot\mathbf{l}+\mathrm{P}_{L-l,k}\mathbf{L}\cdot(\mathbf{L}-\mathbf{l})]^2}{2\,\tilde{\mathrm{P}}^{\mathrm{tot}}_{l,k}\tilde{\mathrm{P}}^{\mathrm{tot}}_{L-l,k}}} &(3.52)
\end{aligned}$$

With the definition of the noise power spectrum N_L^{Φ},

$$\begin{aligned} \langle \Phi(\mathbf{L}) \Phi^*(\mathbf{L}') \rangle &= (2\pi)^2 \delta^D(\mathbf{L} - \mathbf{L}') N_L^{\Phi} && (3.53) \\ \text{or } \langle ||\Phi(L)||^2 \rangle &= (2\pi)^2 \delta^D(0) N_L^{\Phi} && (3.54) \end{aligned}$$

it follows that

$$N_L^{\Phi} = \frac{1}{\sum_k \int \frac{d^2l}{(2\pi)^2} \frac{[\mathrm{P}_{l,k}\, \mathbf{L}\cdot\mathbf{l} + \mathrm{P}_{L-l,k}\, \mathbf{L}\cdot(\mathbf{L}-\mathbf{l})]^2}{2 \tilde{\mathrm{P}}^{\mathrm{tot}}_{l,k} \tilde{\mathrm{P}}^{\mathrm{tot}}_{L-l,k}}} \qquad (3.55)$$

and since the variances of estimator D of the displacement $\langle D \rangle_{\mathrm{ens.}} = \delta\theta$ and Φ are just related by $\langle ||D(\mathbf{L})||^2 \rangle = L^2 \langle ||\Phi(\mathbf{L})||^2 \rangle$ we obtain

$$\begin{aligned} N_L^D &= \frac{1}{\sum_k \frac{1}{L^2} \int \frac{d^2l}{(2\pi)^2} \frac{[\mathrm{P}_{l,k} \mathbf{L}\cdot\mathbf{l} + \mathrm{P}_{L-l,k} \mathbf{L}\cdot(\mathbf{L}-\mathbf{l})]^2}{2 \tilde{\mathrm{P}}^{\mathrm{tot}}_{l,k} \tilde{\mathrm{P}}^{\mathrm{tot}}_{L-l,k}}} \\ &= \frac{1}{\sum_k N_{L,k}^{-1}} && (3.56) \end{aligned}$$

so we have justified that we can simply sum over seperate k modes to arrive at our final lensing noise.

3.7 Appendix B: Quadratic estimator lensing reconstruction in practice

In this section we would like to test how well the quadratic estimator performs in practice. We remind us of the form of this estimator

$$\hat{\psi}(\mathbf{L}) = N(\mathbf{L}) \int \frac{d^2 l}{2\pi} \tilde{\theta}(\mathbf{L}-\mathbf{l}) \tilde{\theta}^*(\mathbf{l}) g(\mathbf{L}, \mathbf{l}) \,. \tag{3.57}$$

By requiring the estimator to be unbiased and having maximal signal-to-noise, we had found that

$$g(\mathbf{L}, \mathbf{l}) = \frac{(\mathbf{L}-\mathbf{l}) \cdot \mathbf{L} C^{\theta}_{|\mathbf{L}-\mathbf{l}|} + \mathbf{l} \cdot \mathbf{L} C^{\theta}_{l}}{2 \tilde{C}^{tot}_{l} \tilde{C}^{tot}_{|\mathbf{L}-\mathbf{l}|}} \tag{3.58}$$

with the normalization

$$N(\mathbf{L}) = \left[\int \frac{d^2 \mathbf{l}}{(2\pi)^2} \frac{[(\mathbf{L}-\mathbf{l}) \cdot \mathbf{L} C^{\theta}_{|\mathbf{L}-\mathbf{l}|} + \mathbf{l} \cdot \mathbf{L} C^{\theta}_{l}]^2}{2 \tilde{C}^{tot}_{l} \tilde{C}^{tot}_{|\mathbf{L}-\mathbf{l}|}} \right]^{-1} \,. \tag{3.59}$$

Let us reshape the result for the estimator a little:

$$\hat{\psi}(\mathbf{L}) = N(\mathbf{L}) \, \mathbf{L} \cdot \int \frac{d^2 l}{2\pi} \frac{(\mathbf{L}-\mathbf{l}) C^{\theta}_{|\mathbf{L}-\mathbf{l}|} + \mathbf{l} C^{\theta}_{l}}{2 \tilde{C}^{tot}_{l} \tilde{C}^{tot}_{|\mathbf{L}-\mathbf{l}|}} \tilde{\theta}(\mathbf{l}) \tilde{\theta}^*(\mathbf{L}-\mathbf{l}) \tag{3.60}$$

For computational convenience, this convolution in harmonic space can be expressed as a product in real space. The advantage of this is that all integrals can be evaluated using FFT's. Let us look at the first term of Equation 3.60 (the second term will be the equivalent). We have

$$\hat{\psi}(\mathbf{L}) = N(\mathbf{L}) \mathbf{L} \frac{1}{-i} \cdot \int \frac{d^2 l}{2\pi} \left(\frac{-i \mathbf{l} C^{\theta}_{l} \tilde{\theta}(\mathbf{l})}{2 \tilde{C}^{tot}_{l}} \right) \left(\frac{\tilde{\theta}(\mathbf{L}-\mathbf{l})}{\tilde{C}^{tot}_{|\mathbf{L}-\mathbf{l}|}} \right) \tag{3.61}$$

Define $\mathbf{F}_1(\mathbf{l}) = \frac{-i l C^{\theta}_{l} \tilde{\theta}(\mathbf{l})}{\tilde{C}^{tot}_{l}}$ and $F_2(\mathbf{L}-\mathbf{l}) = \frac{\tilde{\theta}(\mathbf{L}-\mathbf{l})}{\tilde{C}^{tot}_{|\mathbf{L}-\mathbf{l}|}}$. Omit factor $\frac{1}{2}$ in $\mathbf{F}_1$ (because of second term in equation 3.60), so that the estimator of ψ becomes

$$\hat{\psi}(\mathbf{L}) = i N(\mathbf{L}) \mathbf{L} \cdot \int \frac{d^2 x}{2\pi} e^{-i \mathbf{L} \cdot \mathbf{x}} F_1(\mathbf{x}) F_2(\mathbf{x}) \tag{3.62}$$

The convergence can then simply be obtained through

$$\hat{\kappa}(\mathbf{L}) = -\frac{1}{2} L^2 \hat{\psi}(\mathbf{L}) \tag{3.63}$$

This algorithm can be applied to a three dimensional observable such as 21 cm radiation from both before and during the epoch of reionization[10]. Here we show the results of implementing the 3D algorithm to reconstruct a Gaussian convergence field.

The result of the lensing reconstruction for both Planck and for our 5 MHz 21cm data slice (the representative lensing reconstruction noise levels are shown in Figure 3.4) are shown in Figure 3.9. These maps have an angular extent of 10°. In the case of Planck (the left panel), no resemblance can be seen between input and reconstructed convergence. The 21 cm reconstruction is better (many degree scale features seen in the input are located in the reconstruction) in this case because of a slightly better angular resolution assumed in this experiment compared to Planck (3' versus 5'), but also because we are probing multiple planes in redshift. Finally, in Figure 3.10, we show two profiles of input and reconstructed convergence from the maps shown in Figure 3.9.

---

[10] although our quadratic estimator will be sub-optimal during the patchy regime

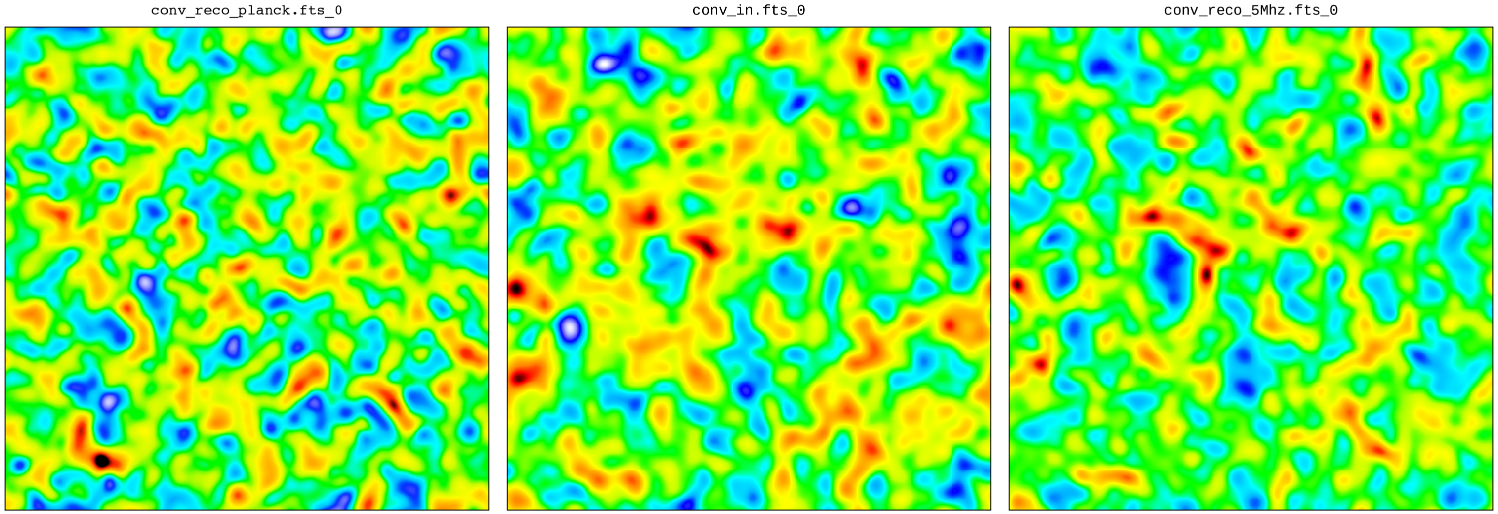

Figure 3.9 *Middle panel:* Input convergence, a Gaussian random field on 10°. The convergence power spectrum used was obtained from integrating over the matter power spectrum (from CMBFAST) to $z = 8$. The field looks qualitatively similar when integrating to $z = 1089$, only the temperature gradient has been adjusted. *Left panel:* the result of the lensing reconstruction using the specifications of Planck (polarization reconstruction is not very effective in this case). *Right panel:* result of lensing reconstruction using the quadratic estimator introduced in this chapter for a 5 MHz wide band centered around z=8, corresponding to $\Delta z = 0.26$. The corresponding lensing reconstruction noise level is shown in Figure 3.4. Notice that for the case of 21 cm we have only used a fraction of the redshift regime potentially accessible for the reconstruction. All three maps have been smoothed after the reconstruction with a 5' beam.

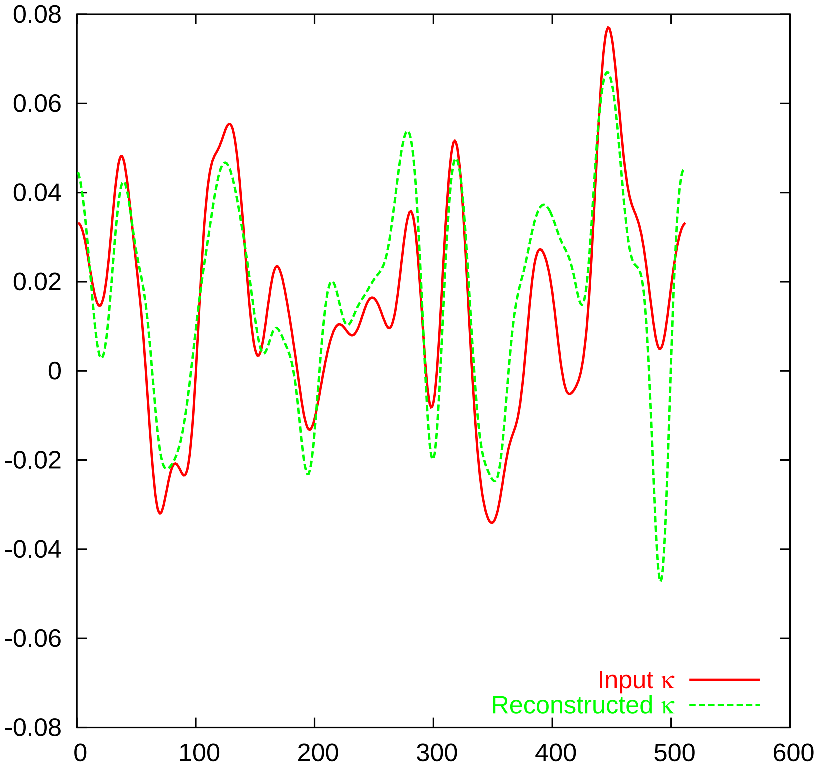

Figure 3.10 A random profile through input and 21 cm reconstructed convergence maps. The abscissa units are number of pixels. Even for our small redshift window probing the lensed EoR fluctuations, there is a clear match between original and reconstructed convergence profiles.

Chapter 4

The influence of inhomogeneous reionization on the CMB[1]

In this chapter we investigate the impact of spatial variations in the ionized fraction during reionization on temperature anisotropies in the CMB. To do so we combine simulations of large scale structure to describe the underlying density field with the analytic model based on extended Press-Schechter theory described in Chapter 2 to track the reionization process. We find that the power spectrum of the induced CMB anisotropies depends sensitively on the character of the reionization epoch. Models that differ in the extent of the "patchy phase" could be distinguished by future experiments such as the Atacama Cosmology Telescope (ACT) and the South Pole Telescope (SPT). In our models, the patchy signal peaks at $l \simeq 2000$, where it can be four times larger than the kinetic Sunyaev-Zel'dovich (kSZ)/Ostriker-Vishniac (OV) signal ($\Delta T_{\rm tot} \simeq 2.6\mu K$). On scales beyond $l \simeq 4000$ the total Doppler signal is dominated by kSZ/OV, but the patchy signal can contribute up to 30% to the power spectrum. The effect of patchy reionization is largest on scales where the primordial CMB anisotropies dominate. Ignoring this contribution could lead to significant biases in the determination of cosmological parameters derived from CMB temperature measurements. Improvements in the theoretical modeling of the reionization epoch will become increasingly important to interpret the results of upcoming experiments.

---

[1] Based in part on O. Zahn, M. Zaldarriaga, L. Hernquist, M. McQuinn, Astrophysical Journal, 630, 657 (2005)

4.1 Introduction

Cosmic Microwave Background (CMB) anisotropy experiments have now constrained temperature fluctuations down to scales of $4'$ [110, 111] resulting in a much improved understanding of inhomogeneities during the time of decoupling at $z \simeq 1100$ and of the global properties of the Universe. In combination with data from Supernovae Ia, measurements of the local expansion rate, galaxy clustering studies, and observations of the Lyman α forest, the CMB data has lead to the establishment of a “standard” cosmological model. We live in a Universe dominated by dark energy and with significantly more dark matter than baryons. Structure grew from a scale independent spectrum of primordial Gaussian fluctuations, in good agreement with predictions of inflationary models.

In the CMB community, theoretical and experimental interest is shifting to the study of secondary anisotropies on smaller angular scales, discussed in the preliminary chapter. We will overlook the effects, caused by fluctuations in the distribution of baryons and dark matter in the redshift regime $z \simeq 0 - 30$, here again briefly. Future data on the different secondary effects will constrain the way structure formation proceeded from the linear into the nonlinear regimes. Secondary anisotropies can be divided into three categories: gravitational lensing effects, inverse Compton scattering of CMB photons by hot plasma, and Doppler related anisotropies.

Mass concentrations along the line of sight such as clusters, sheets, and filaments lead to weak deflection of the CMB photons, or *Gravitational Lensing* (for a review see chapter 9 of [112]). Gravitational lensing of the CMB can be used as a cosmological probe in various ways. The lensing effect on the CMB power spectrum could help break degeneracies between cosmological parameters [113, 114]. Lensing induces departures from Gaussianity on CMB maps that can be used to reconstruct the spatial distribution of the lensing mass [115, 94]. The CMB lensing signal can be correlated with galaxy lensing shear providing additional information. Thus, lensing can be used to probe the evolution of gravitational clustering, constrain the properties of the dark energy, the shape of the matter power spectrum, and neutrino physics (see e.g. [116, 94, 117]).

Inverse Compton scattering in the hot intracluster medium, also called the thermal Sunyaev-Zel’dovich effect [118], changes the spectrum of the CMB photons, leading to cold spots (decrements) in the microwave background at frequencies below 217 GHz and to hot spots (increments) at frequencies above. The effect is proportional to the line-of-sight integrated pressure. Because it is independent of redshift, it is a unique probe of collapsing structures out to $z \simeq 3$ (see Figure 4.6). The thermal SZ effect has been measured in follow-up observations of X-ray clusters (see for instance [119, 120]). Comparison of the cluster SZ temperatures with the X-ray measured temperatures leads to constraints on the angular diameter distance. The SZ effect also leaves a signature in the CMB power spectrum on small scales where the primordial CMB vanishes. BIMA (the Berkeley Illinois Maryland Association) and CBI (the Cosmic Background Imager) claim detections of this effect at $\geq 2\sigma$ significance levels [110, 111]. CBI infers a LSS clustering amplitude on 8 Mpc/h scales of $\sigma_8 = 0.9$, which is at the upper level of constraints from cluster observations and weak lensing (for a recent compilation of experimental results see table 5 of [121]). Future large angular scale SZ surveys such as SPT promise to measure the cluster abundance as a function of mass and redshift, which will offer the possibility of constraining the matter density and the equation of state of the dark energy.

Finally, *Doppler* related effects are produced by the scattering of CMB photons off electrons moving as a result of the structure formation process. This process, also known as the kinetic Sunyaev-Zel'dovich effect when applied to clusters of galaxies [105], leads to hot or cold spots, depending on whether the ionized baryons move toward or away from the observer. The frequency dependence of the photons is left unchanged, except for tiny relativistic corrections. These "Doppler" induced anisotropies are the only known way to measure the high redshift large scale velocity field.

Several analytical models for the kinetic SZ effect due to patchy reionization have been presented in the literature. They vary significantly in the assumed size and time evolution of spherically shaped bubbles, and whether the ionized regions are correlated [122, 123] or not [124]. Some models employ a prescription for correlating the ionizing sources by using the bias that can be calculated for the dark matter halos in which they presumably reside [123]. All authors agree that on scales below $4'$, where the primordial CMB signal falls rapidly owing to photon diffusion, the Doppler effect induced by patchiness could contribute enough to use it as a tool to study the reionization epoch.

In this chapter, we use a hybrid approach between the analytic model for the formation of HII regions described in Chapter 2, and smoothed particle hydrodynamics (SPH) simulations of large scale structure. The advantage over purely analytic models of patchy reionization kinetic SZ is that our sources follow the complex clustering behavior of dark matter and baryons. An advantage over currently feasible full radiative transfer calculations of the reionization epoch is that we can investigate the morphological properties of reionization on scales an order of magnitude larger with rather small memory and CPU requirements. We re-iterate that our prescription does not directly address many of the (uncertain) physical details of reionization related to star formation, feedback processes, clumpiness, recombinations, and radiative transfer. However, by combining these properties into a single parameter, we are able to explore the basic parameter dependencies, and we believe it is a good starting point to help us understand the morphological properties of cosmological reionization and its influence on the CMB.

In Section 4.3, we explore different parametrizations of reionization. In one model we assume that the source properties are constant so that reionization evolves over a redshift interval of $\Delta z \simeq 4$. In a second model try to do justice on one hand to the rapid decline of the neutral fraction around $z = 6 - 7$, seen in measurements of the Gunn-Peterson optical depth by measuring spectra of distant quasars, while at the same time allowing for earlier onset of reionization, at the high end of the range of values allowed by WMAP [14]. We model this by assuming two succeeding reionization epochs, in which HII regions first are produced by low metallicity (Pop. III) stars, and later expand further during an epoch dominated by Pop. II stars, so that on the whole patchiness lasts longer.

In Section 4.4 we investigate whether the next generation of ground based bolometric arrays will be able to measure reionization and distinguish between different scenarios. The specifications of the Atacama Cosmology Telescope (ACT) [2] [88] and the South Pole Telescope (SPT)[3] [89] will be used to predict how well these experiments can measure CMB temperature power spectra in the region where secondary effects dominate over primordial CMB anisotropies. We find that ACT/SPT should be able to distinguish between sudden homogeneous reionization and patchy reionization at a high level of significance, even if the total optical depth in both scenarios were the same.

Since the patchy signal peaks on scales where the primordial anisotropy dominates, cosmological parameter estimation may become biased. We will show in Section 4.4.2 that precision experiments such as Planck should take this bias into account either by focusing on their polarization data or by adding a reionization parameter to their analysis.

Our numerical simulations of large scale structure and the power spectra we used to generate realizations of the primordial CMB assume a cosmology in agreement with WMAP constraints: $\Omega_{dm} = 0.26$, $\Omega_\Lambda = 0.7$, $\Omega_b = 0.04$, fluctuations on 8Mpc/h scales of $\sigma_8 = 0.9$, and no tilt ($n_S = 1$) or running ($\alpha_S = 0$) of the spectral index.

---

[2] see http://www.hep.upenn.edu/ angelica/act/act.html

[3] see http://astro.uchicago.edu/spt/

4.2 Simulation of secondary anisotropy and patchy reionization

Our approach is to use large scale simulations of the cosmic web as a basis for applying the model described in Chapter 2 as a post-processing step to generate HII regions during the reionization phase. The underlying large scale structure was simulated using the parallel Tree-PM/SPH solver GADGET [125], based on the fully conservative implementation of SPH by [126]. Here, we used the results of runs with a boxsize of 100Mpc/h and 216^3 particles, with parameters corresponding to the G-series runs of [127]. In what follows, we employ a simulation that included only "adiabatic" gas physics; i.e. the gas can heat or cool adiabatically and be shocked, but we do not include radiative effects or the consequences of star formation and associated feedback processes. Snapshots of the simulation are produced every light crossing time interval. This leads to 77 outputs between $z = 0$ and $z = 20$. These simulations are described in more detail in [128].

We implemented the model for the HII morphology as described in Chapter 2. As underlying density field we used the high redshift snapshots from our simulation. Although the analytic model by definition calls for a Gaussian random density field, the small non-linearities present in our box should not constitute a grave violation. We expect the ionized regions to be large in comparison to the non-linear scale, the former being 10 Mpc/h on average, the latter being below 1 Mpc/h. An advantage of using the non-linear field for the density is that the mode coupling effects described in Section **??** should be properly modeled. Through a detailed comparison we verified however that these effects are small on the level of the kinetic SZ effect.

To obtain the underlying density field, we discretize the matter fluctuations in our simulation boxes into 256^3 cells. The overdensity, δ, is then smoothed with a top hat window function.

To sample a wide range of bubble sizes, and obtain a smoothly varying ionization fraction, we varied the barrier in radial direction throughout each box by adjusting the redshift dependent minimal ionization radius. The reionization information for each of the 256^3 cells is stored. A 8 Mpc/h deep cut through the stacked outputs between $z \simeq 12$ and $z \simeq 17$ is shown in Figure 4.1, for one of the models we will describe in the next section, in which the ionization efficiency is constant, $\zeta = 60$. The periodic boundary conditions of our simulation boxes are apparent in this plot[4].

---

[4] note that to simulate maps of the CMB, we will randomly translate the simulation volumes before projecting them, see below

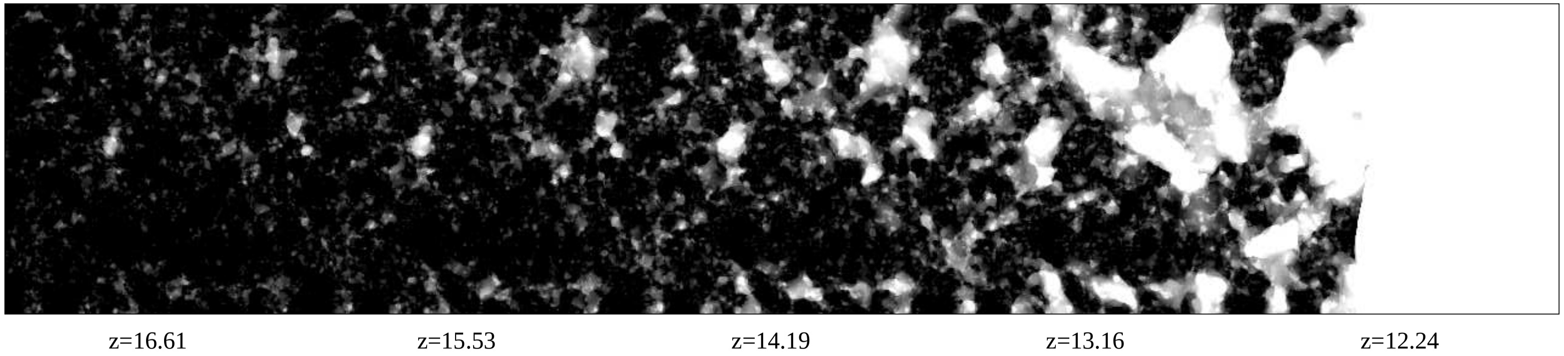

Figure 4.1 Time development between redshifts $z = 12$ and $z = 17$ of an 8Mpc/h deep slice through an inhomogeneously ionized $\zeta = 60$ (constant) box, with increasing ionization fraction. The outputs with periodic boundary conditions are simply stacked behind each other here. In order to obtain realistic maps, the individual outputs where randomly rotated and translated in our simulations. At the low redshift end, the bubbles become comparable in size to the box.

To compute the electron scattering and gravitational lensing effects from the content of the simulation boxes, we only need to store two-dimensional maps of the product of pressure and volume (Compton scattering), the velocity weighted free electron density (Doppler effect), and the matter density (lensing). We simulate regions on the sky with an angular extent of 1° each, at a resolution of 256^2 pixels. In the small angle approximation we can simply project the content of each simulation box onto a plane in its center. At high redshifts, $z > 5.7$, the field of view exceeds the boxsize, so we use the periodic boundary conditions to cover it. During the patchy regime, only those gas particles that are located in an ionized cell according to the information we stored earlier contribute to the signal. At later times all particles are assumed ionized. We translate and rotate the positions and velocities of the particles randomly before doing the projection onto the plane. The gas particle properties are distributed over surrounding pixels weighted by the SPH kernel. For dark matter particle masses we use the cloud-in-cell algorithm. Photons are traced through the planes from a regular grid close to the observer towards the last scattering surface. We produced Gaussian random fields of the primordial CMB using spherical harmonic decomposition coefficients generated with the publicly available code CMBFAST[5] [56].

In models of patchy reionization, CMB anisotropies are caused by two types of contributions induced by Doppler scatterings: perturbations in the baryon density ω_b, given by $\delta\omega_\mathrm{b} = \rho_\mathrm{b}/\rho_\mathrm{tot} - 1$, and local changes in the ionization fraction δx_e. These produce a change in temperature of the CMB blackbody. The total contribution to the temperature anisotropy is given by the integral over conformal time [6]

$$\frac{\Delta T_{kSZ}}{T_{CMB}}(\hat{\mathbf{n}}) = -\frac{\sigma_T}{c}\overline{n}_p(\eta_0)\int d\eta[a^{-2}e^{-\tau_{ri}(\eta)}\bar{x}_e(\eta)]\hat{\mathbf{n}}\cdot q \tag{4.1}$$

with

$$q = (1 + \frac{\delta x_e}{\bar{x}_e(\eta)})(1 + \delta\omega_\mathrm{b})\mathbf{v}\,. \tag{4.2}$$

The Thomson scattering optical depth is σ_T, τ_{ri} is the optical depth from the observer to conformal time η, and $\hat{\mathbf{n}}$ is the line of sight unit vector.

To implement patchy reionization, we use the semi-analytic model described in Chapter 2. We implement this model into the large scale structure realization given by the high redshift outputs of our SPH simulation. Besides the simplifications involved in the analytic modeling, there are two potential

---

[5] http://www.cmbfast.org

[6] During homogeneous reionization and at lower redshifts, where galaxy clusters are present, this is traditionally called the kinetic Sunyaev-Zel'dovich effect, at higher redshifts the Ostriker-Vishniac [129] effect

dynamical range limitations in our approach that we should address. First, because the mean overdensity on scales larger than the simulation box is artificially set to zero in numerical simulations, in order to achieve periodic boundary conditions, we expect a systematic bias in the overall ionization fraction. [45] estimated this effect and showed that it should be less than 1% in simulations of 100 Mpc/h size. A different bias arises from our finite mass resolution. Our lack of structure on scales smaller than $L_{box}/(N_{\rm part.})^{1/3}$ leads to a slight delay in the onset of reionization. Very small overdensities on scales below 0.5 Mpc/h, that could harbor ionizing sources with HII regions around them, are not captured by our analysis.

4.3 Results for various time dependence of ζ

In our analysis we will compare three different reionization scenarios. These are tuned such that they all lead to a comparable integrated optical depth, $\tau_{\rm ri} \simeq 0.125 - 0.133$[7] The different histories of the fraction of ionized volume elements $Q(z)$ are shown in Figure 4.2.

Model A describes a universe that undergoes homogeneous and instantaneous reionization at redshift 14. This is the standard scenario [56, 130] assumed in likelihood analyses of large scale CMB polarization anisotropy (in its correlation with temperature, see [3, 14]). This model has $\tau_{ri} = 0.133$.

Model B is the patchy model described above, with the assumption of constant source properties. An ionization efficiency $\zeta = 60$ leads to reionization beginning at $z = 19$ and concluding by $z = 12$. This model has $\tau_{ri} = 0.130$.

Model C exhibits extended patchiness. We describe this by assuming a first generation of metal free sources starting at redshift 20 with an ionization efficiency of $\zeta = 200$ (it has been suggested that their photon output could be 10-20 times higher than that of normal stars, see [131, 132, 133]). In our model, these sources sustain themselves only to redshifts around 15, because their hard photons dissociate fragile H_2 they need for cooling (e.g. [134, 135]). However, the first sources are assumed to leave pockets of ionized medium which begin to harbor Pop II stars. The initial mass function becomes less

---

[7] This value is at the high (1-σ) end of the currently preferred range of the WMAP analysis [14]. We chose our reionization optical depth before the release of this updated analysis, when the WMAP data pointed to an even higher value of $\tau_{\rm ri} = 0.17 \pm 0.05$ [3]. Our choice of $\boldsymbol{\tau_{\rm ri}}$ was a compromise between the CMB data and quasar spectra results at the time (pointing to a lower value of $\tau_{\rm ri} \simeq 0.06$. We repeated our analysis for a lower redshift scenario and find that the results are very similar. This is because the patchy kSZ signal we are simulating is determined by the extend of reionization more than its absolute redshift.

top heavy with time, and we describe the resulting Population II stars with an efficiency $\zeta = 12$. This leads to a total optical depth of $\tau_{ri} = 0.125$. Our model has a monotonically evolving ionization fraction. We note that another way of reconciling CMB with quasar spectra observations is by resorting to recombinations that leave 0.1% of the universe neutral until $z = 6 - 7$ [32].

In Figure 4.2, we plot for all three models the fraction of ionized volume elements as a function of redshift, $Q(z)$. In Model A, the neutral fraction drops instantaneously at $z = 14$, in Model B sources of a constant ionization efficiency $\zeta = 60$ lead to a brief partly ionized phase, and in Model C the ionization fraction "freezes in" for some time, while metal free Pop. III stars cease to exist and leave residual ionized bubbles for "normal" Pop. II stars to be created and to ionize the medium fully at $z = 7 - 8$.

We divide the total Doppler signal into three different redshift regimes in Figure 4.3. The maps have a side length of 1° and are smoothed with a Gaussian beam of width $\theta \simeq 1'$, corresponding to a multipole number of $l_{max} \simeq 10000$, comparable to the angular resolution of ACT, and slightly below that of SPT. It is expected that during the interval from $z = 0$ to $z = 3$, more strongly clustered regions make the Doppler effect maps highly non-Gaussian. We show this by the solid line (PDF) in Figure 4.4. In the picture in the center ($z = 3 - 11$) structure formation is less advanced. The corresponding histogram can be well-approximated by a Gaussian, as shown by the long-dashed curve in Figure 4.4. Signals created by radially moving inhomogeneities during this epoch are referred to as the Ostriker-Vishniac effect [129]. The plot on the right of Figure 4.3 is the patchy epoch of reionization Model B. Again, this epoch has a largely Gaussian morphology (short-dashed line of Figure 4.4), because structures on scales of the ionized bubbles are just beginning to collapse. According to this figure, large bubbles form on scales of tens of Mpc. The redshift regimes represented by the left and middle picture have the same properties in all three of our reionization scenarios.

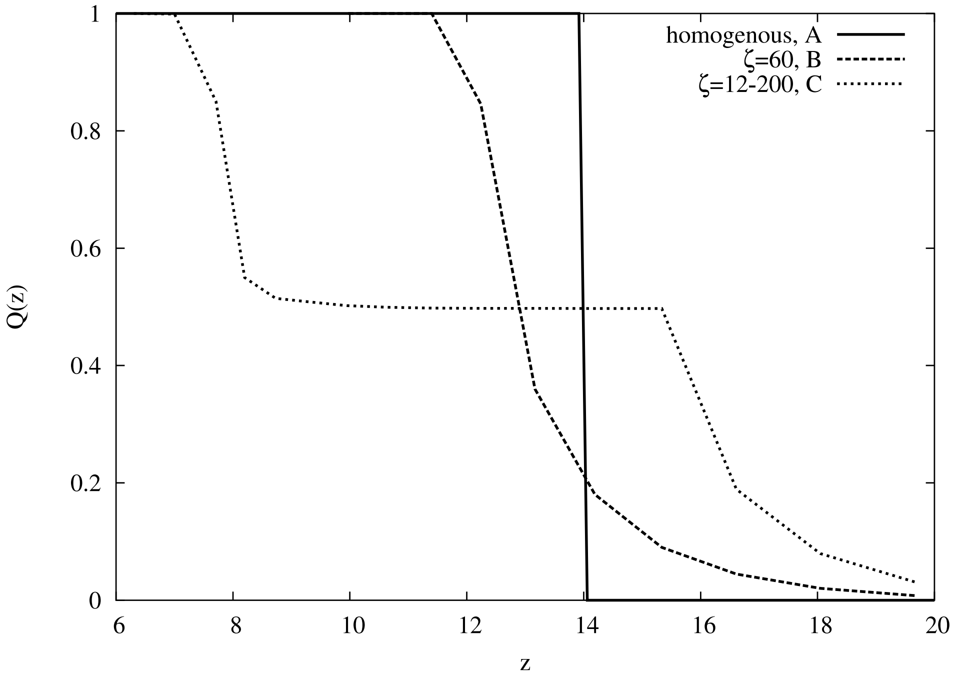

Figure 4.2 Evolution of the fraction of ionized volume elements $Q(z)$ in our calculations of reionization. Solid curve corresponds to instantaneous reionization at redshift $z = 14$, yielding an optical depth of $\tau_{ri} \simeq 0.125$ for standard cosmological parameters. The dashed curve represents our patchy model in the case of a constant ionizing efficiency of sources. The dotted curve is for a model where a first generation of metal-free stars can survive the negative feedback of H_2 photodissociation for a limited period of time, then formation of these stars comes to a halt, leaving a network of HII regions. After a while, Population II stars are born inside these regions and their photons gradually lead to a homogeneously ionized universe (Model C). Model C spends the longest time in the partly ionized regime and will therefore lead to the largest signal of the three models which have comparable total optical depth.

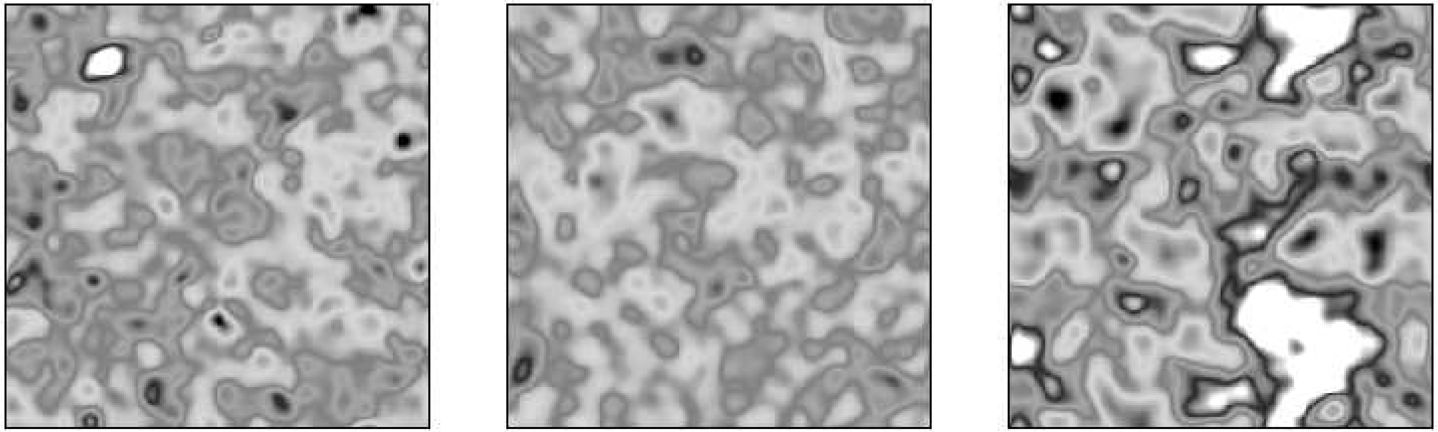

Figure 4.3 Based on the implementation of Model B with a constant value of ζ, we divide the Doppler signal into three redshift epochs. Plot on the left shows the kinetic Sunyaev-Zel'dovich effect out to redshift 3, in the middle the Ostriker-Vishniac regime from $z = 3$ out to $z = 11$ is shown, and on the right the regime of non-uniform (patchy) reionization. Each picture shows the same angular extent, 1°. The left panel exhibits highly clustered structures. With increasing redshift, the clustering becomes more linear and patchy reionization leads to CMB signals on large scales. We smoothed the maps obtained from our simulations by a Gaussian beam corresponding to $l = 10000 \simeq 1'$, comparable to the angular resolutions of ACT and SPT.

The upper panel of Figure 4.5 shows that in the homogeneously reionizing universe, the largest portion of the Doppler signal comes from low redshifts, the kSZ regime. The upper panel represents the case of homogeneous reionization, Model A. Contrary to the thermal SZ effect, the signal still carries information about higher redshifts, $z \leq 10$. We can use this principle to gain knowledge about the details of reionization taking place at high redshifts. The additional contributions from larger redshifts ($z > 10$) in Model C are shown in the lower panel of the figure.

For comparison, we show in Figure 4.6 how different redshift regimes contribute to the thermal SZ effect (where $\Delta T/T = -2y$ for low frequencies). The plot shows that this signal is basically saturated at $z = 3$; the thermal SZ effect receives most of its contribution from galaxy clusters in the more nearby universe.

4.4 Observability of patchy reionization with future CMB experiments

In this section, we assess the observability of patchy reionization with future experiments. ACT and SPT should be able to distinguish different reionization scenarios with high significance by measuring temperature power spectra. In their cosmological parameter analyses, all-sky experiments such as Planck will have to account for patchy reionization as a possible source of bias and need to rely on their polarization data in order to obtain proper constraints.

4.4.1 Power spectral constraints from ACT and SPT

The effect of patchy reionization on the CMB power spectrum is of similar magnitude to that of the Doppler effect induced by variations in the mean density. The first source population is heavily biased so the patchy reionization signal peaks on larger angular scales. Figure 4.1 shows that for the regime in which the ionization fraction is roughly 50% (which is where most of the signal comes from) the bubbles reach sizes of tens of comoving Mpc. In Figure 4.7 we plot the different contributions to the Doppler power spectrum. Patchy reionization in Model C with $\zeta = 12 - 200$ lasts from redshifts 20 to 7. The signal imprinted in the CMB from this epoch is shown in solid. At later times, the universe is homogeneously reionized and the dashed line shows the kinetic SZ effect for this period.

Inverse Compton scattering in galaxy clusters leads to a larger signal than that caused by Doppler scattering. Because only a small fraction of the

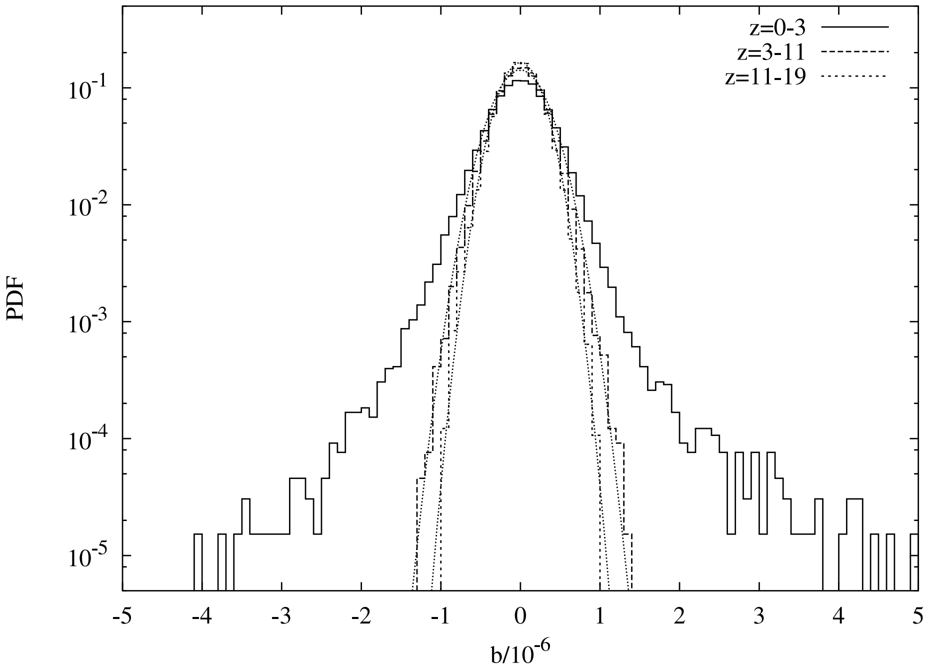

Figure 4.4 The probability distribution functions for the three maps in Figure 4.3 are shown. The solid line is for the kinetic SZ regime z=0-3, the long-dashed line for the Ostriker-Vishniac era z=3-11, the short-dashed line for the patchy epoch of model B with constant ionization efficiency, z=11-19. The two histograms representing the earlier cosmological epochs are well-approximated by Gaussians.

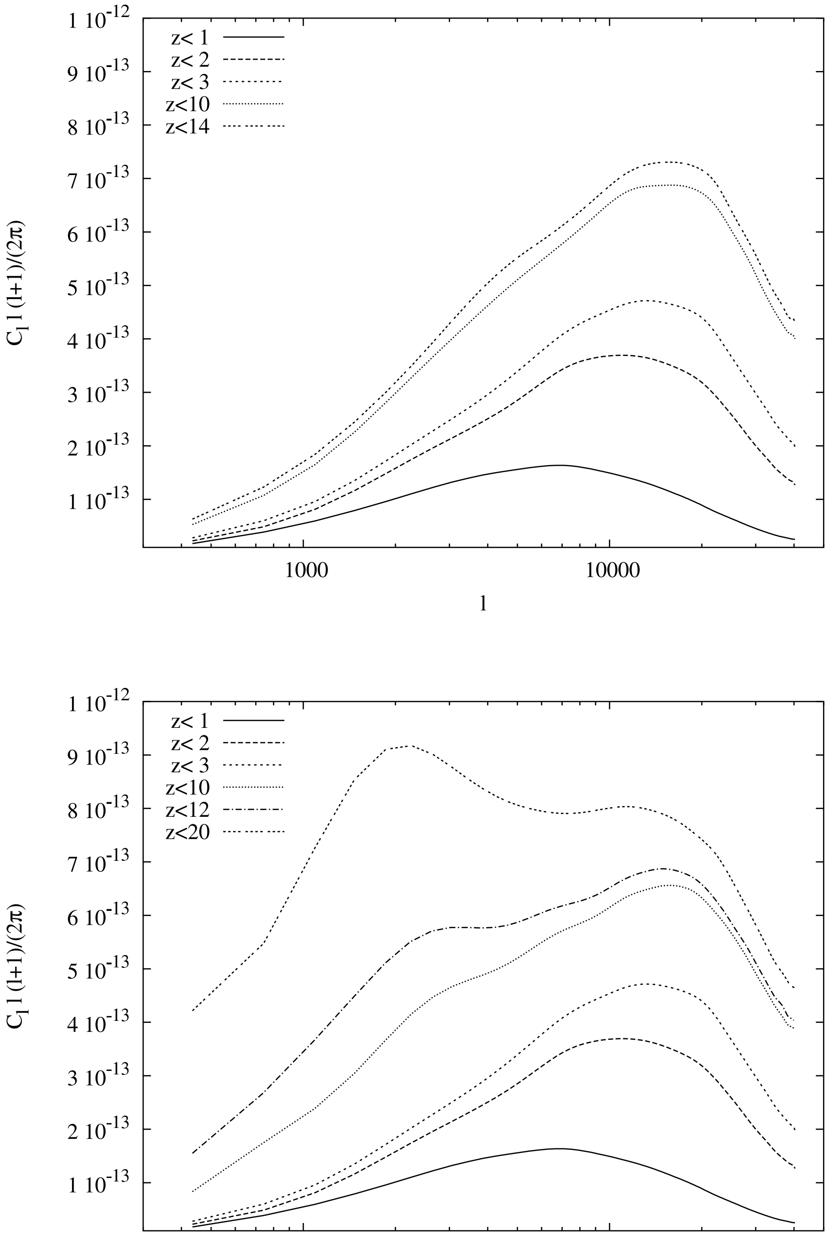

Figure 4.5 Contribution to the kinetic SZ signal for Models A (upper panel) and C (lower panel) out to different redshifts. Although a large fraction of the total Doppler effect comes from low redshift, high overdensity regions, there is a significant contribution out to $z \simeq 10$. In the patchy model (bottom) the regime $z = 11 - 19$ leads to further enhancement of the signal.

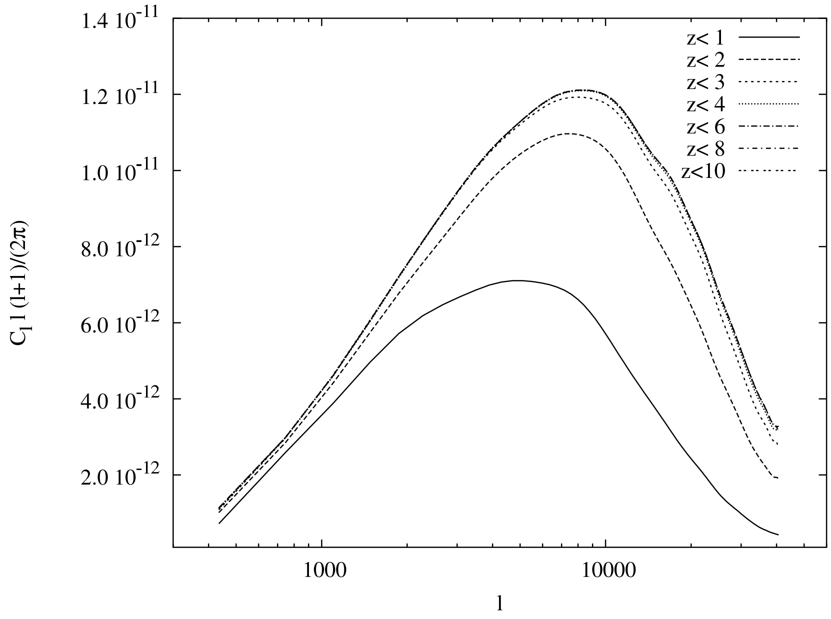

Figure 4.6 Redshift dependence of the thermal Sunyaev-Zel'dovich $\Delta T/T = -2y$ effect as generated with our simulations. The major contribution comes from galaxy clusters in the regime $z < 3$. Hence, the thermal SZ effect is less suited for studying the reionization epoch than is the kinetic SZ effect.

CMB photons present are likely to scatter inside the cluster medium ($\simeq 1\%$ for a massive 15 keV cluster), the distribution will not thermalize to that of the hot gas. The effect has a characteristic frequency dependence, and it can be distinguished from Doppler scatterings which leave the frequency distribution of the photons unchanged. The dot-dashed line in Figure 4.7 is the combination of the secondary signal with the primordial CMB, once the thermal SZ with its characteristic frequency distribution has been removed.

On scales where patchiness during reionization contributes more to the total signal than the Doppler effect owing to modulations in the density, ($l < 4000$), the primordial anisotropies dominate. To study the secondary anisotropies created during reionization one has to observe angular scales where photon diffusion smoothes out the primary anisotropies.

Upcoming experiments such as ACT and SPT will observe the sky in a number of frequency bands with comparable sensitivity and angular resolution. ACT [88] will observe in three frequency bands: 145, 225, and 265 GHz, with FWHM beam-widths θ_{FWHM} of 1.7, 1.1, and 0.9 arcminutes, respectively. We use the specifications of the 225 GHz channel for our power spectrum analysis because the thermal SZ effect almost vanishes in this frequency regime, its zero being at $\nu \simeq 218\ GHz$. The sensitivity per resolution pixel for this channel is $\sigma = 2\ \mu K$. The South Pole Telescope [89] will observe in five bands at 95, 150, 219, 274, and 345 GHz. The 219 GHz channel will have an angular resolution of $\theta_{FWHM} = 0.69'$ and a sensitivity of $10\mu K$ [8]. We assume sky coverages of 0.5% and 10% for ACT and SPT, respectively.

From these specifications and a template for the power spectrum of primary and secondary anisotropies at arcminute scales (which we obtain from our simulations), we can calculate the errors in the C_l determination, including noise as additional random field on the sky [136]):

$$\Delta C_l = \sqrt{\frac{2}{f_{sky}(2l+1)}} \left[C_l + \frac{f_{sky}}{w B_l^2} \right] , \tag{4.3}$$

where we assume errors bars corresponding to a Gaussian map. Here, $w = (\theta_{fwhm}\sigma)^{-2}$, and B_l is a beam profile (assumed Gaussian) given by $B_l = e^{-\theta_b^2 l(l+1)/2}$ (with $\theta_b = \theta_{fwhm}/\sqrt{8\ln 2}$).

We assume that experiments such as ALMA [9] will lead to a good understanding of the point source frequency spectrum and angular clustering. In more pessimistic scenarios where only the frequency dependence or nothing is known about point sources, they can strongly degrade our ability to detect the kinetic SZ [137] (we included their estimate for the IR source power

---

[8] J.E. Ruhl, private communication.

[9] http://www.eso.org/projects/alma/science/alma-science.pdf

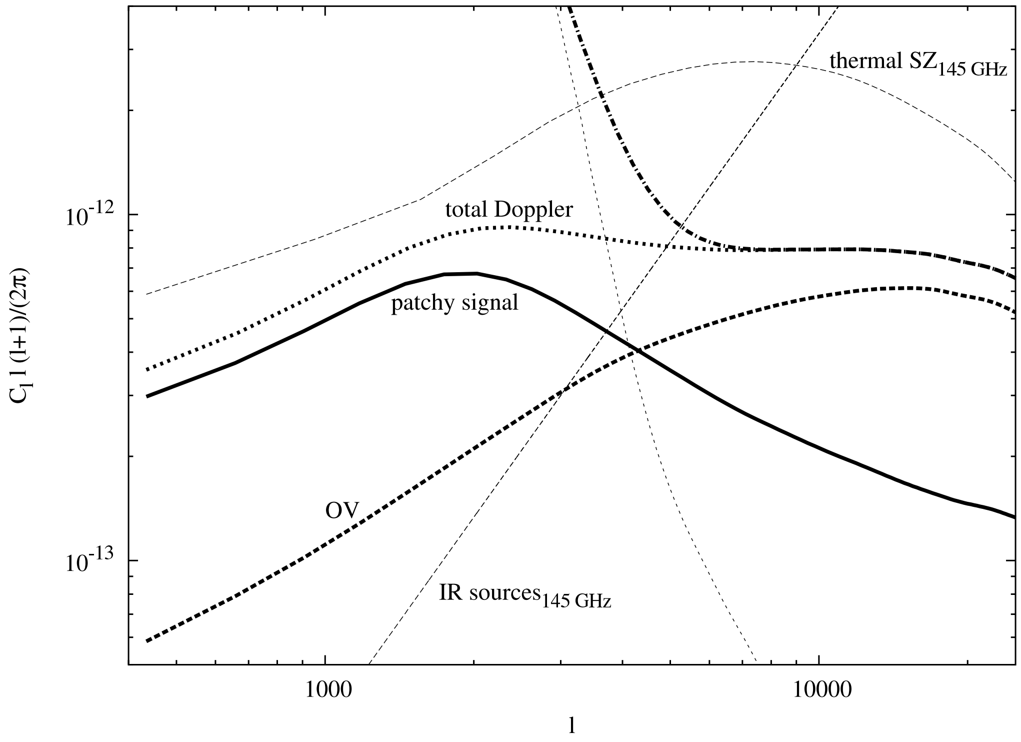

Figure 4.7 Different contributions to the total Doppler signal (kinetic SZ) in our extended patchy reionization Model C. The solid curve is the contribution to temperature anisotropies from the patchy regime alone at $z = 7 - 20$. The dashed curve gives the Doppler effect from density modulations at homogeneous ionization out to $z = 11$. The dotted curve sums up those contributions to the total Doppler signal. The total temperature fluctuations, cleaned of the thermal SZ and IR sources (shown at 145 GHz in the thin dashed lines), is given by the dot-dashed curve. These curves are smoothed versions of the power spectra generated from 50 maps.

spectrum at 145 GHz in Figure 4.7). On the other hand the assumption of perfect cleaning of the thermal SZ effect is safer because we understand its frequency dependence well.

To compare the experimental constraints with the power spectra extracted from our simulations on degree patches on the sky, we bin the errors into bands of width $\Delta l = 360$. The predicted measurements errors are plotted in Figure 4.8, together with power spectra generated from the "cleaned" maps of primordial CMB and kinetic SZ combined. Since the kinetic SZ appears almost featureless on the scales accessible to the next generation of experiments, reionization models can be distinguished by their average amplitude on these scales. The error bars in the relevant band-powers of ACT are combined using $\sigma^2_{tot} = (\sum_i \sigma_i^{-2})^{-1}$. It follows that the overall amplitude can be measured with an accuracy of $\sigma_{\Delta T} = 0.011\mu K$ (we assumed a 1% calibration uncertainty). Given that the plateau of the extended patchy model (Model C) lies at $\Delta T \simeq 2.407\mu K$, while Model A has an average amplitude on these scales of $\Delta T \simeq 2.076\mu K$, the two will be distinguishable at the 30σ level with ACT, if we ignore contamination by point sources and by the thermal SZ, which is not a realistic assumption. This is the same for the South Pole Telescope, which has better angular resolution, but will look less deep (it has a much larger survey area).

It is also of interest to ask whether additional constraints on reionization scenarios could be achieved by using non-Gaussian statistics, in particular the four point function (the skewness arising from a line-of-sight velocity effect should vanish). It may be expected, that because the HII regions are created inside large overdensities at high redshift, patchy models are more Gaussian on the whole. The main problem with this notion is that in any patchy model with a comoving bubble size comparable to ours this effect will suffer from "washing out" by the primordial CMB. On scales where Doppler induced fluctuations become larger than the primordial CMB, the impact of patchiness amounts only to a fraction of the total signal (15% in Model B, 30% in Model C), the rest being attributed to scatterings owing to density modulations alone. Also, the majority of non Gaussian contributions comes from clusters and filaments at $z < 3$, compare Figure 4.4. We computed the kurtosis

$$\Theta_4 \equiv \frac{\langle (\Delta T/T)^4 \rangle}{\sigma_T^4} - 3 \tag{4.4}$$

of thermal SZ "cleaned" maps (i.e. primordial CMB+Doppler) that were filtered with a Gaussian in Fourier space, approximately cutting out "contamination" by the primordial CMB anisotropies below $l \simeq 3500$, and beam smearing at scales of $l \simeq 9000$ comparable to the angular resolution of ACT

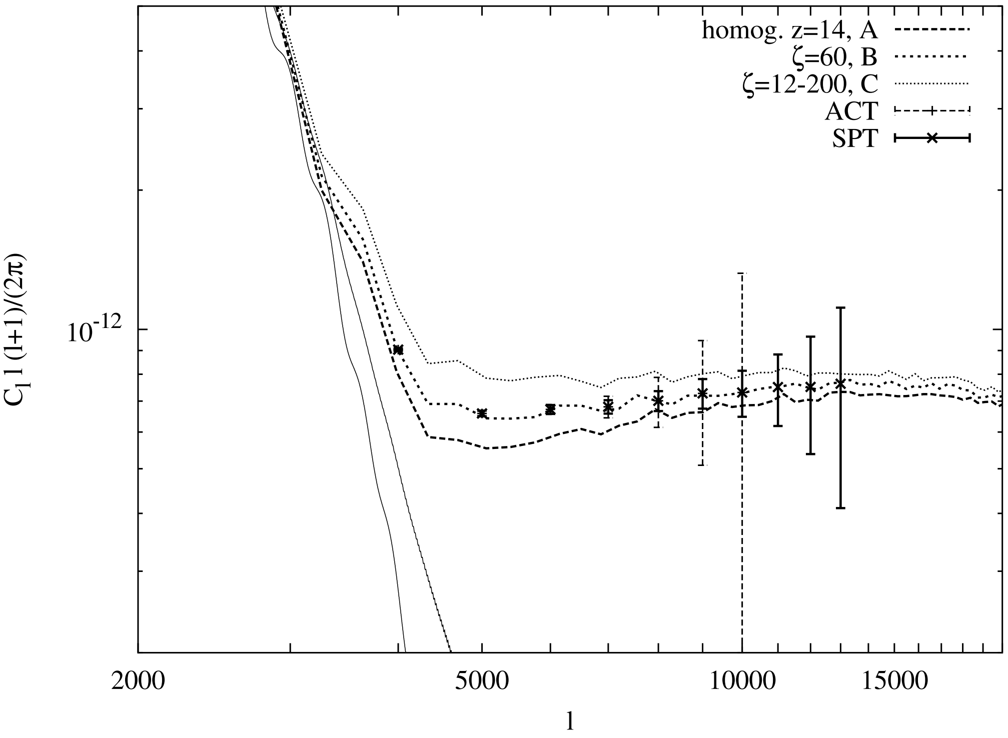

Figure 4.8 With future experiments like ACT, the various reionization models should be easily distinguishable by measuring the temperature power spectrum. Since the kinetic SZ signal is almost featureless on the scales of experimental relevance, the band-powers can be combined to a simple amplitude when distinguishing the different models. We find that the double reionization scenario (given by the upper power spectrum) could thus be distinguished at high significance from a uniform, instantaneous model where the universe reionizes at $z = 14$ (bottom curve). The change of the ionizing efficiency with time $\dot{\zeta}$ affects the slope of the secondary anisotropy power spectra.

(similar to the window function proposed by [137]). Using this method, we do unfortunately not find a statistically significant difference between patchy and homogeneous models of reionization.

4.4.2 Expected bias in cosmological parameter determination from Planck

Cosmic microwave background measurements have been and will likely remain the most precise tools for the measurement of cosmological parameters. The best constraints will come from a combination of CMB temperature and polarization power spectra which encapsulate all the relevant information in the sky maps. The aim is to make the data cosmic variance limited to as high as possible multipole numbers. WMAP is cosmic variance limited up to $l \simeq 500$.

The Planck satellite should achieve cosmic variance limitation out to $l = 2500$ for its temperature power spectrum measurement. Hence, Planck will reach into the regime where the secondary anisotropies become important. To avoid biases in parameter estimation, systematic changes that the secondaries may produce in the power spectra need to be considered.

The contribution to the power spectrum from patchy reionization is one to two orders of magnitude smaller than the primordial CMB anisotropies on the relevant scales, but owing to the exquisite sensitivity of these experiments it biases parameter estimates. For the analytic models of patchy reionization suggested by [122] and [123] this parameter bias was estimated. In these models the mean bubble size is smaller than in our computation, and the signal peaks at higher multipoles.

The bias can be estimated from the Fisher matrix coefficients

$$F_{ij} = \sum_l \frac{\partial C_l}{\partial p_i} w_l \frac{\partial C_l}{\partial p_j} \tag{4.5}$$

in the following manner:

$$\mathcal{B}_i \equiv \frac{\Delta p_i}{\sigma_i} = \frac{\sum_j F^{-1}_{ij} \sum_l \frac{\partial C_l}{\partial p_j} C_l^{\mathrm{D}}}{\sqrt{F^{-1}_{ii}}} \tag{4.6}$$

where Δp_i are the systematic biases in the determination of parameters p_i, w_l are the inverse squares of the statistical errors in the C_l estimation, given by Equation 4.3 and $\sigma_i = \sqrt{F^{-1}_{ii}}$ is the estimate of the error bars for parameter i. In this expression, C_l^{D} denotes the combined Doppler power spectrum owing to kSZ/OV and patchy reionization.

---

model	τ_{ri}	Ω_Λ	ω_{dm}	ω_b	n_s	A_s
1σ	0.0035	0.010	0.0017	0.00018	0.0045	0.0050
A	0.40	1.18	-1.10	1.71	2.14	0.16
B	1.26	1.66	-1.54	2.40	3.05	0.78
C	2.25	2.89	-2.69	4.20	5.62	1.58

Table 4.1 Bias in units of the statistical error ($\mathcal{B}_i$) expected for cosmological parameter estimation with Planck, if temperature and polarization power spectra are used and the influences of kSZ/OV and patchy reionization are neglected in the power spectrum analysis. The maximum multipole in our analysis was $l = 4000$.

We combined the three frequency channels of Planck with the highest angular resolution and took into account the number of polarized instruments. For a one year observation period, the three channels (217, 143 and 100 GHz) have $\theta_{\rm fwhm} = 5.0$,7.1 and 9.2 arcminutes. This leads to the raw sensitivities:

$$\begin{aligned} w_T^{-1} &= (0.0084\mu K)^2 \\ w_P^{-1} &= (0.0200\mu K)^2 \,. \end{aligned}$$

We assumed a sky coverage of $f_{Sky} = 0.8$.

In Table 4.1 we show the results of our analysis, using the power spectra for our different models as bias. The first line shows the statistical error alone, $\sqrt{F_{ii}^{-1}}$, the following lines show the parameter bias $\mathcal{B}_i$ for Models A, B, and C. For Planck, we used the specifications of the High Frequency Instrument [10]. The power spectra derivatives for the Fisher analysis were computed for the fiducial cosmological model given in the introduction.

It is clear from Table 4.1 that secondary anisotropies need to be taken into account. This is the case in particular for parameters that influence the shape of the power spectra at intermediate scales ($\omega_b, \omega_{dm}, n_s$). Constraints on the amplitude A_s and the optical depth owing to reionization $\tau_{\rm ri}$ are less heavily biased (besides the amplitude, the reionization optical depth only affects CMB polarization on large scales). Note that even in a simple homogeneous reionization model, as our Model A, most of the biases are of order unity. The individual systematic shifts depend strongly on what parameters are used. The analysis of [123] has extra parameters that make the biasing source (the patchy power spectrum) distribute differently into each parameter offset.

The polarization anisotropies generated during the reionization epoch are expected to be four orders of magnitude smaller than the temperature power

---

[10] http://www.rssd.esa.int/index.php?project=PLANCK&page=perf_top

model	τ_{ri}	Ω_Λ	ω_{dm}	ω_b	n_s	A_s
1σ	0.0041	0.013	0.0020	0.00026	0.0079	0.0056
A	0.010	-0.018	0.017	0.024	0.086	0.068
B	0.027	-0.028	0.026	0.037	0.135	0.196
C	0.050	-0.070	0.067	0.058	0.301	0.487

Table 4.2 Bias in cosmological parameter estimation with Planck is reduced significantly, when temperature power spectra are used only until $l = 1000$ and polarization power spectra are used in the whole range (Planck should be able to measure C_l^{EE} out to $l \simeq 1800$). On the other hand, the parameter errors become only slightly larger by leaving out the high l temperature information.

spectra [138]. This suggests that to avoid biases one could use temperature information down to an angular scale where the Doppler contamination is still negligible but use the polarization data for all l. We show the results of an analysis in which we used temperature information only out to $l \simeq 1000$, but polarization in the full range accessible to Planck (this will be out to $l \simeq 1800$) in Table 4.2. The 1σ error bars for the parameters are only slightly larger than in Table 4.1, indicating that the parameter estimates are more or less "saturated" at $l \simeq 1000$. On the other hand, the expected parameter biases owing to reionization are much smaller. The use of polarization information in future CMB experiments thus can play an important role beyond breaking degeneracies between traditional cosmological parameters and improving the error bars.

The other strategy is to include an extra parameter to model the effect of the Doppler contributions. This approach has the added advantage that a positive constraint on reionization could be obtained with Planck alone. Patchiness shifts the power spectrum on small scales, and we model this by a "patchy amplitude" parameter. This parameter is included by adding the Doppler spectra given in the last section with a variable amplitude A_D to the primordial CMB. If the parameter derivatives in the Fisher matrix center ($A_D = 1$) around Model B, we find that the amplitude parameter could be constrained with $\sigma_{A_D} = 0.51$. The model is only $\simeq 0.3\sigma$ away from homogeneous reionization (Model A), so Planck will not be able to make a strong statement. If patchy reionization turns out to be extended, similar to Model C, Planck should observe this at higher significance $\sigma_{A_D} = 0.20$, amounting to a 5σ detection of Doppler induced secondary anisotropies, with the amplitude of Model C being 3σ away from homogeneous reionization. Finally, if reionization proceeded homogeneously, Planck will not gain knowledge beyond its large scale polarization measurements of τ_{ri} by using small scale temperature fluctuations, given that the uncertainty for our Model A lies at $\sigma_{A_D} = 0.71$.

When Planck's power spectra are modeled with the "patchy amplitude" parameter, constraints for the standard cosmological parameters are slightly improved over the analysis that abandoned temperature data beyond $l = 1000$ (Table 4.2), despite the introduction of an extra parameter. Concretely, we find in this analysis that $\sigma_{\tau_{ri}}$=0.037, σ_{Ω_Λ}=0.011, $\sigma_{\omega_{dm}}$=0.0018, σ_{ω_b}=0.00021, $\sigma_{\Omega_{n_s}}$=0.0058, σ_{A_s}=0.0052.

The Doppler power spectrum can bias the result of parameter analyses with future CMB surveys. Planck may be able to improve constraints on models with an extended epoch of patchiness. We hope to have shown in this section that careful modeling of the epoch of first stars will become crucial for doing precision cosmology with progressively more refined CMB experiments.

4.5 Conclusions and Outlook

In this chapter we have presented simulations of secondary anisotropies in the cosmic microwave background calculated using smoothed particle hydrodynamics simulations of large scale structure, focusing on the effect produced by patchy reionization. We incorporated our semi-analytic model for the morphology of the HII regions into our numerical treatment and investigated whether such patchy scenarios can be distinguished from homogeneous reionization.

An important advantage of our technique over pure analytical predictions of patchy reionization kinetic SZ is that we follow the complicated clustering of dark matter and baryons into the slightly non-linear regime. In contrast to full radiative transfer calculations of the reionization epoch, we combine uncertainties in the physics of source formation, feedback processes and radiative transfer into a single parameter and explore the consequences of varying this parameter. This simplification allows us to make predictions on scales an order of magnitude larger than current radiative transfer schemes can accomplish with a small expense of memory and CPU.

We extracted power spectra from sky maps produced by tracing rays across our simulation volumes. The patchy reionization signal peaks on multipole scales of $l \simeq 2000$, and it increases the amplitude of the "cleaned" CMB power spectrum by up to 30% on scales $l \geq 4000$, so that the total level of Doppler related anisotropies is $\Delta T \simeq 2.4\mu K$. We found that with the next generation of ground based CMB experiments (ACT, SPT) the different reionization models we investigated could be distinguished with high significance by using the power spectrum. Additional information about the morphological properties of that epoch that could be obtained for instance by measuring the four point function or other deviations from Gaussianity will probably be difficult to obtain, because the reionization signal peaks on angular scales where the primordial CMB anisotropies dominate. In the future, it may be possible to combine measurements of the CMB with other observations such as 21 cm fluctuations from neutral hydrogen [75] or Lyman-alpha emission from high redshift galaxies (e.g. [19]) to further constrain the topology of the reionization process.

We investigated the bias in the determination of cosmological parameters that will be produced by the additional patchy reionization signal, when extracting cosmological parameters from CMB anisotropy measurements. We find that for Planck this bias is significant. The bias may be circumvented by focusing completely on polarization information in the multipole regime where patchiness peaks, with only a slight disadvantage in parameter constraints. Alternatively, a template for the Doppler spectrum could be introduced in the parameter analysis which may lead to a detection of the effects of an extended reionization phase.

4.6 Appendix: Simulations of the thermal Sunyaev-Zel'dovich effect and comparison to other authors

The thermal Sunyaev-Zel'dovich effect (tSZ) is caused by the hot thermal distribution of electrons in the intra-cluster medium (ICM) of clusters of galaxies. For a massive cluster, the probability of a CMB photon passing through to encounter a single interaction with an ICM electron is about 1%. Inverse Compton scattering increases the energy of the CMB photon by roughly $k_B T_e / m_e c^2$, leading to a small distortion in the CMB spectrum. This leads to a decrement in comparison to the primordial CMB at frequencies below 217 GHz, and an increment above. This follows from the derivation in [139], leading to the following result

$$\frac{\Delta T_{\mathrm{th.SZ}}}{T_{\mathrm{CMB}}}(\theta) = f(x)\; y(\theta) \text{ where} \tag{4.7}$$

$$y(\theta) = \frac{\sigma_T k_B}{m_e c^2} \int dl n_e(\theta, l) T_e(\theta, l) \tag{4.8}$$

where the amplitude y is commonly referred to as the thermal Comptonization parameter. For an isothermal cluster it equals the optical depth, τ_e, times the fractional energy gain per scattering. The Thomson cross-section is denoted σ_T, n_e is the electron number density, T_e the electron temperature, k_B Boltzmann's constant, and $m_e c^2$ the electron rest mass energy in the line of sight integral. The characteristic frequency dependence of the thermal SZ is

$$f(x) = \left(x \frac{e^x + 1}{e^x - 1} - 4 \right) (1 + \delta_{\mathrm{SZE}}(x, T_e)), \tag{4.9}$$

where $\delta_{SZE}(x, T_e)$ is a correction due to relativistic electron velocities in the ICM. Note that $f(x) \to -2$ in the non-relativistic and Rayleigh-Jeans (RJ) limits so the equations simplify to $\frac{\Delta T_{\mathrm{SZE}}}{T_{\mathrm{CMB}}} \simeq -2y$.

From the above expression we realize that $\Delta T_{\mathrm{SZE}}/T_{\mathrm{CMB}}$ is independent of redshift. This feature of the SZE makes it a unique tool for investigating the high redshift universe.

To give a rough order of magnitude estimate of the thermal SZE, note that the probability of scattering is 1%, and the spectral distortion for a 5 keV cluster is roughly 0.01, so the temperature fluctuation imprinted in the CMB in this case would be of order 10^{-4}.

Our simulation of the thermal SZ effect was decribed in Section 4.2. We show the map resulting from our simulation in Figures 4.9 (the Compton-y parameter). It is the result of ray tracing through 76 simulation boxes, while including the effect of weak gravitational lensing. Each data cube is randomly rotated and translated along the line of sight before computation of its SZ contribution. The final map has been smoothed with a beam corresponding to a half arcminute, slightly smaller than the nominal resolutions of ACT and SPT.

In Figure 4.10, we show the angular power spectrum, $C_l l(l+1)/2\pi$ of our simulation in the gray curve. This is the result of running our ray tracing algorithm ten times while using different seeds for the random orientations of each box, to make the power spectrum smoother. We note that the effects of gravitational lensing on the relatively featureless SZ power spectrum is small.

As the simulation of the thermal SZ effect has a long history of analytic and numerical modeling attempts, we wanted to compare our results to other predictions. In particular we obtained the angular power spectra results of [140, 141, 142, 143]. We included these results in Figure 4.10. We made one slight modification to make this comparison more realistic: the different authors have used different cosmologies. In particular their values for the overall normalization of the matter power spectrum, σ_8, which denotes fluctuation amplitude on an 8 Mpc/h scale, is different. Also the baryon density

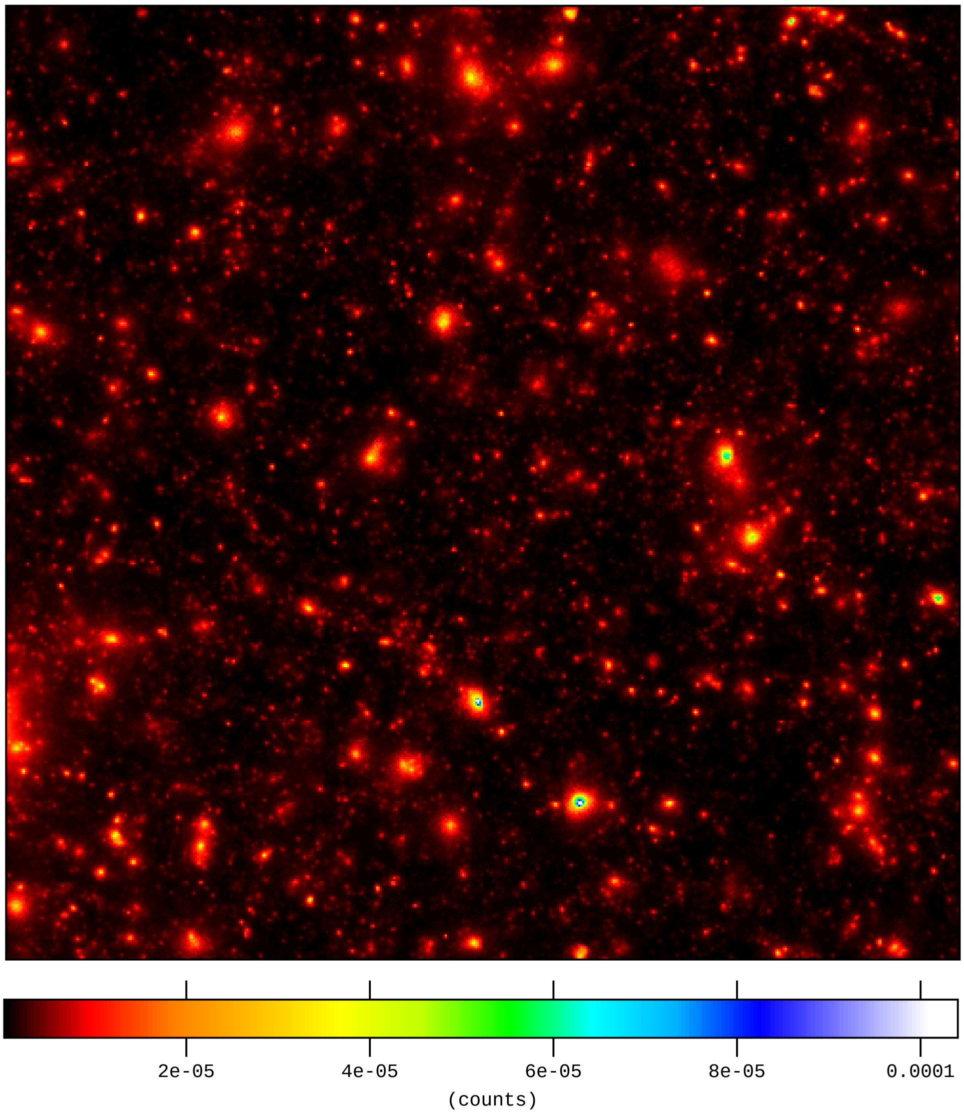

Figure 4.9 Map of the thermal SZ effect, on a 1° map, extracted from our simulations. This is the result of tracing 512^3 rays through the 76 simulation volumes between z=0-20. The color scheme shows the Compton-y parameter for the thermal SZ (which corresponds in the Rayleigh-Jeans regime to 50% of the temperature fluctuation).

which enters in the power spectra simply as $\omega_b \equiv \Omega_b h$, is different. Reference [144] found a scaling of the thermal SZ with σ_8 of $C_l^{\mathrm{th.SZ}} \propto \sigma_8^7$. Although this is probably not the final answer, and other authors find scaling between σ_8^{6-8}, we adopt the [144] scaling and multiply the curves obtained from the authors by

$$C_l^{\mathrm{rescaled}} = C_l^{\mathrm{authors}} \times \frac{0.9^7}{\sigma^7_{8,\mathrm{authors}}} \times \frac{0.028^2}{\omega^2_{b,\mathrm{authors}}}$$

($\sigma_8 = 0.9$ and $\omega_b = 0.028$ being the parameters in our simulation) to achieve a more proper comparison. We plan to investigate these scaling relation further in future work. We find that the the re-scaled predictions for the thermal effect differ from each other by a large factor, up to 70% on large as well as small scales. In part this can be ascribed to modeling differences in the gas distribution throughout the intracluster medium (ICM), in other cases the analytic models have an advantage in that they can assemble more massive objects, whereas the largest cluster we find in our simulation has a mass of $\simeq 8 \times 10^{14} M_\odot$ at z=0, and there is a gap in the mass function down to $\simeq 2 \times 10^{14} M_\odot$. Massive clusters contribute a substantial fraction to the signal [144], and their abundance needs to be modeled carefully.

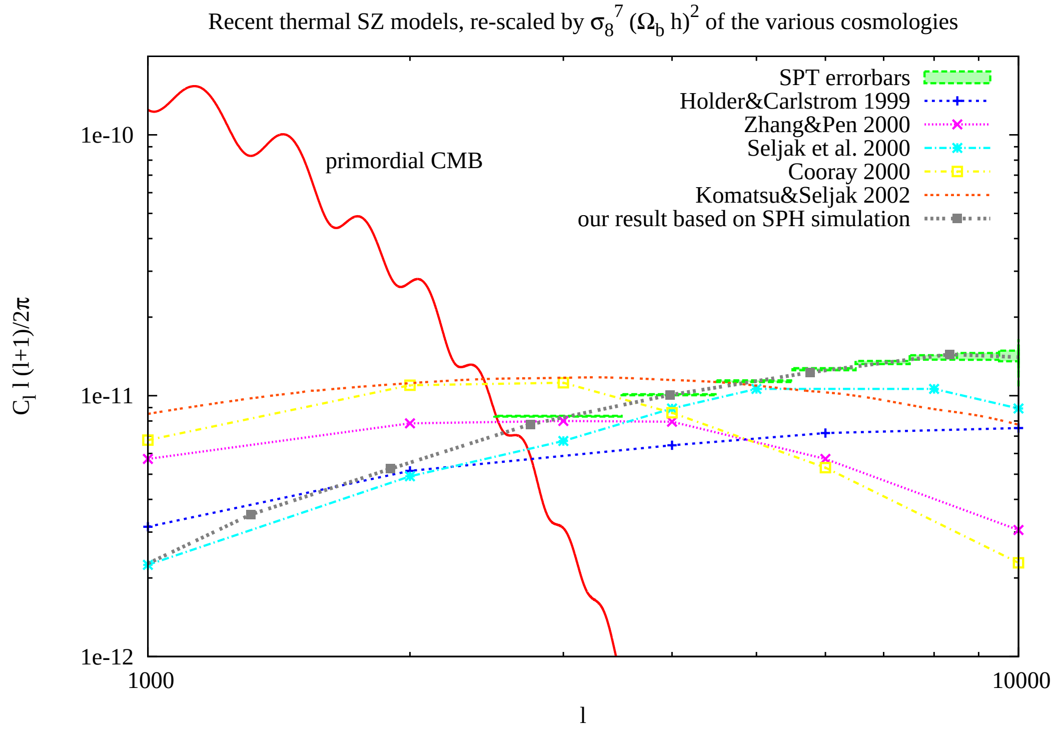

Figure 4.10 Recent estimates of the thermal Sunyaev-Zel'dovich angular power spectrum based on various analytic and numerical modeling schemes, as referenced in the key. The result from our simulation is shown in the gray line. The various results differ significantly in amplitude and shape, even after accounting for the different cosmological parametrizations used. The green errorbars are estimated sensitivities for the Atacama Cosmology Telescope. This shows that models have to improve substantially before the scientific harvest from upcoming experiments can be fully realized.

Chapter 5

Simulations and Analytic Calculations of Reionization Morphology [1]

In this chapter we present results from a large volume simulation of Hydrogen reionization. We combine 3d radiative transfer calculations and an N-body simulation, describing structure formation in the intergalactic medium (IGM), to detail the growth of HII regions around high redshift galaxies. Our N-body simulation tracks 1024^3 dark matter particles, in a cubical box of co-moving side length $L_{\mathrm{box}} = 65.6$ Mpc h^{-1}. This large volume allows us to accurately characterize the size distribution of HII regions throughout most of the reionization process. At the same time, our simulation resolves many of the small galaxies likely responsible for reionization. It confirms a picture anticipated by analytic models: HII regions grow collectively around highly-clustered sources, and have a well-defined characteristic size, which evolves from a sub-Mpc scale at the beginning of reionization to $R \gtrsim 10$ co-moving Mpc towards the end. We show that in order to obtain this qualitative picture, source resolution must not be sacrificed at too great a level. We present a detailed statistical description of our results, and compare them with our numerical hybrid scheme based on semi-analytic modeling, described in Chapter 2. We find that the analytic calculation reproduces the size distribution of HII regions, the power spectrum of the ionization field, and the 21 cm power spectrum of the full radiative transfer simulation remarkably well. The ionization field from the radiative transfer simulation, however, has more small scale structure than the analytic calculation, owing to Poisson

---

[1] Based in part on O. Zahn, A. Lidz, M. McQuinn, S. Dutta, L. Hernquist, M. Zaldarriaga, S. Furlanetto, Astrophysical Journal, 654, in press (2006)

scatter in the simulated abundance of galaxies on small scales. We propose and validate a simple scheme to incorporate this scatter into our calculations. Our results suggest that analytic calculations are sufficiently accurate to aid in predicting and interpreting the results of future 21 cm surveys. In particular, our fast numerical scheme is useful for forecasting constraints from future 21 cm surveys, and in constructing mock surveys to test data analysis procedures.

5.1 Introduction

In Chapter 2 we motivated the introduction of analytic models to describe the morphology of reionization: modeling the largest scales while resolving the smallest sources responsible is challenging. In this chapter, we push forward by running a large volume radiative transfer simulation. Our work represents progress on several fronts. First, we simulate reionization in a larger volume than most previous works (although see [34, 35]), while maintaining high mass resolution. This allows us to reliably calculate the size distribution of HII regions as well as power spectra of ionization and 21 cm fields, impossible with previous small volume simulations. Second, we compare our results with the analytic calculations based on FZH04. These models are now widely used, and while elegant and inspired by previous small volume reionization simulations [32, 33], they remain untested. Our comparison also gauges the level of theoretical control in our modeling of reionization – i.e., how robust are our conclusions to the details of our modeling? One convincing way to dissuade the above-mentioned skeptic is to demonstrate that we can understand the gross features of our radiative transfer simulations *analytically.* Additionally, if analytic models are sufficiently accurate then they are useful tools to forecast constraints from future experiments, and to construct mock surveys, providing important tests of data analysis procedures. This is important given our ignorance of the nature of the ionizing sources: we would like to cover a large parameter space in the source properties, prohibitive with time-consuming radiative transfer simulations. Furthermore, future surveys will span volumes of several cubic Giga-parsecs, a challenging task for detailed simulations.

We emphasize that our present work is only a first step towards more realistic simulations of Hydrogen reionization. As we describe subsequently, our radiative transfer simulations miss potentially important aspects of the physics of reionization. Specifically, we include only a crude prescription for the sources of ionizing photons, our coarse resolution underestimates the importance of recombinations – especially if mini-halos are present during

---

reionization [145, 146, 147] – and misses small galaxies that may contribute ionizing photons, and we ignore feedback effects entirely. We intend to model some of these effects in the near future.

Our work has overlap with the recent simulation and analysis of [35]. In comparison to these authors, reionization finishes significantly later in our simulation, near $z \sim 6.5$, as compared to $z \sim 12$, a consequence of our more conservative prescription for the ionizing sources. Besides improving the accuracy of simulations of the reionization epoch, an important emphasis of our present work is in comparing our radiative transfer simulation results with 'hybrid simulations' based on analytic models.

The layout of this chapter is as follows. In Section 5.2 we describe our N-body simulation, source prescription and radiative transfer calculation. In Section 5.3 we describe our 'analytic model simulation', which is more precisely an implementation of a model based on FZH04 into the cosmological realization used for the radiative transfer simulation. We will sometimes refer to this scheme losely as an 'analytic calculation' although the implementation of the model is entirely numerical. In Section 5.4 we present a detailed statistical description of our radiative transfer and analytic results. We describe a numerical scheme that incorporates the stochasticity of the source distribution into our analytic calculations in Section 5.5. We also show that if extremely bright and rare sources reionize the IGM, bubble growth is less collective than in our fiducial model.

In Section 5.6 we compare radiative transfer and analytic model predictions for the 21 cm signal. We conclude in §5.7, mentioning future research directions and emphasizing possible improvements to our simulations.

Throughout we assume a flat, ΛCDM cosmology parameterized by: $\Omega_m = 0.3$, $\Omega_\Lambda = 0.7$, $\Omega_b = 0.04$, $H_0 = 100h$ km/s/Mpc with $h = 0.7$, and a scale-invariant primordial power spectrum with $n = 1$, normalized to $\sigma_8(z = 0) = 0.9$ [2]

5.2 Simulations

We begin by running a large N-body simulation to locate dark matter halos, and produce a cosmological density field. Next, we populate the dark mat-

---

[2] This value for σ_8 is slightly different than the value preferred by the WMAP satellite alone of 0.76 ± 0.05 [14]. When combined with other datasets, such as the Lyman-α forest [148, 149], and weak lensing (see e.g. section 4.1.7 and Table 6 of [14]), a higher value of σ_8 can be found. Furthermore, changes in the fluctuation amplitude within this experimental range can be incorporated in our comparison between radiative transfer and "analytic" schemes by changing slightly the ionization efficiency parameter. This does not qualitatively affect our results.

ter halos with ionizing sources, using a simple prescription to connect mass and light (Section 5.2.2). In a subsequent post-processing step, we perform a radiative transfer calculation, casting rays of ionizing photons from our sources through the cosmological density field (Section 5.2.3). We make two approximations with this approach. First, we assume that the gas distribution perfectly traces the dark matter distribution, as characterized by our N-body simulation. Second, we neglect the interplay between gas dynamics and radiation transport – i.e, in reality, structure formation responds to the passage of ionization fronts, and gas motions in turn influence the propagation of the fronts. These effects are essential in calculating the detailed small-scale behavior of ionization fronts, as fronts slow down upon impacting dense clumps [147], but are less important for our goal of capturing the large-scale size distribution of HII regions.

5.2.1 N-body simulations

As noted in the introduction, we require a cosmological simulation with a large dynamic range, in order to adequately sample the distribution of HII regions, while simultaneously resolving small galaxies. Ideally, we would resolve halos with virial temperatures of $T_{\rm vir} \gtrsim 10^4$ K – corresponding to a dark matter halo mass of $M_{\rm dm} \sim 10^8 M_\odot$ at $z \sim 6$ – above which atomic line cooling is efficient. In halos more massive than this, gas can cool, condense to form stars, and produce ionizing photons. This 'cooling mass' therefore represents a plausible guess as to the minimum host halo mass for ionizing sources. If molecular Hydrogen cooling is efficient despite radiative feedback, however, even smaller mass halos should host sources [150]. Presently, we ignore this possibility. Additionally, high resolution is required to capture the clumpiness of the IGM, and properly account for recombinations during reionization. On the other hand, HII regions may be larger than $R \gtrsim 20$ Mpc h^{-1} at the end of reionization [50], necessitating a large volume simulation. As described in Chapter 2, to resolve a $10^8 M_\odot$ halo with 32 particles, in a simulation box of side-length $L = 100$ Mpc h^{-1}, for example, requires a prohibitively large number of particles, $N_p \sim 3500^3$!

Our present N-body simulation is meant to represent a compromise between these competing requirements of large volume, and high mass resolution. Specifically, our N-body simulation follows 1024^3 dark matter particles in a box of side-length, $L = 65.6$ Mpc h^{-1}, using an enhanced version of the TreePM code, Gadget-2 [151]. We run the simulation assuming the flat LCDM cosmology specified in the introduction, with initial conditions generated using the [152] transfer function.

Dark matter halos are identified from simulation snapshots, using a friends-

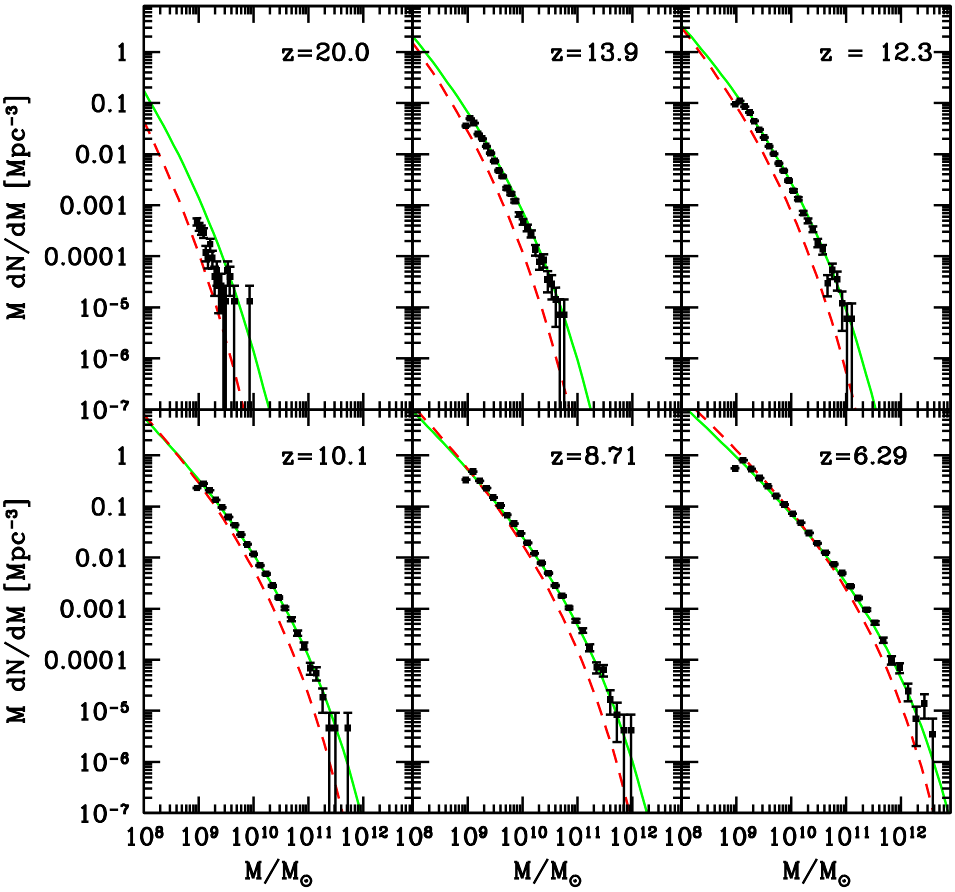

Figure 5.1 Halo mass function from our N-body simulation. The black points with (Poisson) error bars indicate the halo mass function from our simulation as a function of redshift. The green curve is the Sheth-Tormen fitting function for the halo mass function, while the red dashed line shows the Press-Schechter fitting function.

of-friends algorithm (e.g., [153]). Specifically, particles are grouped into halos using a linking length of $b = 0.2$ times the mean interparticle separation. Linked groups of greater than 32 particles are considered resolved, and to constitute dark matter halos. This corresponds to a minimum halo mass of $10^9 M_\odot$, just an order of magnitude above the cooling mass.

The resulting mass function is shown in Figure 5.1, spanning a broad redshift range between $z \sim 6-20$. [45] showed that if a simulation is normalized to the cosmic mean density, the halo mass functions will be biased. According to Figure 3 of [45] the bias introduced in our calculations should only be of order 0.1 %. The halo mass function is sampled with large dynamic range, roughly three orders of magnitude near $z \sim 6$. The simulated mass function is always larger than predicted by the Press-Schechter formalism [52], but generally in good agreement with the Sheth-Tormen [154] fitting formula. At the highest redshifts sampled, however, our results fall in between the two fitting formula. This is in qualitative agreement with recent measurements from [155], and [156], although our mass function appears systematically higher than that of [35]. The figure shows that the abundance of our lowest mass halos is systematically below theoretical expectations, likely a consequence of our limited mass resolution. As a conservative measure, we therefore place ionizing sources only in halos of mass larger than $M_{\rm min} = 2 \times 10^9 M_\odot$, corresponding to a $64-$particle halo.

5.2.2 Ionizing Sources

Our next step is to connect mass with light – that is, we wish to populate the dark matter halos from our N-body simulation with ionizing sources. In this thesis, we will adopt a very crude prescription for our ionizing sources, leaving a more sophisticated prescription to future work. This will facilitate comparison with the analytic models (see Section 5.3). Specifically, we populate each dark matter halo with a single source whose luminosity in Hydrogen ionizing photons is directly proportional to the host halo mass, $\dot{N} = c M_{\rm halo}$. Clearly the parameter c encodes a good deal of complicated physics, involving the efficiency of star formation, the efficiency of producing ionizing photons, the fraction of ionizing photons that escape from the host halo, etc. With this single simplifying assumption, the cumulative number of ionizing photons released by the sources, per hydrogen atom in the IGM, at time t is $N_{\rm ph}/N_H \propto \int_0^t dt' f_{\rm coll}(t')$. Here $f_{\rm coll}(t')$ is the fraction of mass in halos with mass $M \geq M_{\rm min} = 2 \times 10^9 M_\odot$. Using the [154] mass function, which closely matches our simulation results (Figure 5.1), we find that $c = 3.1 \times 10^{41}$ photons/sec/$M_\odot$ yields one photon per hydrogen atom at $z = 6.5$. (See Figure 5.2 and associated text for a discussion). This choice of

c corresponds roughly, for example, to Pop II stars, forming with an efficiency of $f_\star = 0.1$ from a Salpeter IMF, with a stellar lifetime of $\Delta t \sim 5 \times 10^7$ yrs, and a modest escape fraction of $f_{\rm esc} \sim 0.01$ [157]. We adopt this conversion in all subsequent calculations.

5.2.3 Radiative Transfer

We next form a coarse density field for many snapshots, spaced in equal time intervals of $\Delta t = 5 \times 10^7$ years and spanning a broad redshift range from $z \sim 6 - 16$, by gridding our dark matter particles onto a uniform, Cartesian grid with 256^3 mesh points. Our sources (Section 5.2.1 and Section 5.2.2) are tabulated at the same time-sampling, and moved close to the center of their corresponding cell, with a slight offset of a fraction of a cell to avoid grid artifacts. Occasionally, several sources land in a single cell and our considered to be a sole, more luminous source. At $z \sim 6.5$, near our assumed completion of reionization, there are $\simeq 330,000$ ionizing sources in our simulation.

With the ionizing sources and cosmological density field in hand, we trace rays of ionizing photons through the simulation box using the adaptive ray-tracing scheme of [158], and the code of Sokasian et al. [159, 32]. We refer the reader to these papers for the details of this code, but give a brief summary here. In short, the code assumes a sharp ionization front, and tracks the position of the front by casting rays and integrating over the ionization front jump condition [160]. The jump condition amounts to tabulating the number of photoionizations and recombinations along a ray, halting the ray when its photon supply is exhausted. Each source is considered separately, although the order in which sources are processed is randomized at each timestep to avoid artifacts [32].

Behind the ionization front, each source hitting a given cell contributes a photoionization rate of $\Gamma_{\rm HI,s} = \bar{\sigma}\dot{N}/(4\pi r_s^2)$, i.e. assuming optically thin conditions within the front. Here r_s is the distance from the cell in question to a source, $\dot{N}$ is the number of Hydrogen photons per second from a source, and $\bar{\sigma}$ is a frequency-averaged cross section, computed here assuming each source has a spectrum $\propto \nu^{-4}$ [159]. Within the front, ionization fractions are computed assuming ionization equilibrium, a uniform temperature of $T = 10^4 K$, case A recombination rates [159], and neglecting sub-grid clumping. Helium is assumed to be at most singly-ionized by our soft sources, and we assume that the HeII front precisely tracks the HII front. Similarly, inside the front we assume that the ionized Helium (HeII) fraction traces the HII fraction [32]. Note that all of these assumptions impact mainly the detailed ionization fractions within the front, and are less important for tracking the overall size distribution of HII regions. In contrast to [159, 32], we do not include a diffuse background radiation field, simply allowing rays to wrap around the periodic box.

Our assumption of a sharp ionizing front is justified given the short mean free path of Hydrogen ionizing photons in the pre-reionization IGM. [161] present explicit comparisons between 'ionization front tracking' and more detailed calculations that self consistently solve for the optical depth, ionization fraction, and temperature. At least in the case of a single source (their Figure 16), ionization front tracking reproduces very closely the results of more detailed calculations, further justifying our approach.

In Figure 5.2 we plot the redshift evolution of the ionization fraction in our simulation. The black circles show the mass-weighted ionization fraction, while the blue squares show the volume-weighted ionization fraction. The mass-weighted ionization fraction is somewhat larger than the volume-weighted ionization fraction. This is because the ionizing sources in our simulation are highly biased, and ionize their overdense environs before breaking-free to ionize neighboring voids (e.g. [32, 35]). The reionization process takes a fairly significant stretch of cosmic time, with the mass-weighted ionization fraction at the level of $x_{\rm i,m} \sim 0.1$ at $z \sim 9$, and attaining $x_{\rm i,m} \sim 1$ only by $z \sim 6.5$.

The evolution of the neutral fraction in our model is consistent with, although not required by the measurements of e.g. [8], which demand only that the IGM reionize sometime before $z \gtrsim 6$. Our model produces an electron scattering optical depth of $\tau_e = 0.06$, on the low side of CMB constraints [7], which suggest $\tau_e = 0.09 \pm 0.03$. We emphasize that our choice of c (Section 5.2.2) was calibrated so that reionization ends slightly above $z \gtrsim 6$, so this should be viewed as a consequence of our assumptions, rather than a theoretical prediction. Although our model is tuned to give late reionization, analytic models find that the size distribution of HII regions depends primarily on the bias of the ionizing sources, with only an implicit dependence on redshift [57]. The size distribution of HII regions at a given ionization fraction is therefore expected to be a robust result, independent of our detailed assumptions about the efficiency of the ionizing sources, (although see [57], Section 5.5 for caveats).

Note that our simulation terminates slightly before reionization completes ($x_i(z) \sim 1$). We stop our calculation early because we do not include a 'diffuse background' in our simulation [159], and so our calculation becomes very expensive at the end of reionization when rays wrap around the simulation box several times. In any event, the tail end of reionization is likely poorly modeled in our simulation, since this stage may be regulated primarily by Lyman limit systems [42, 55], which are missing in our analysis.

In our simulation, the mass-weighted ionization fraction closely tracks

---

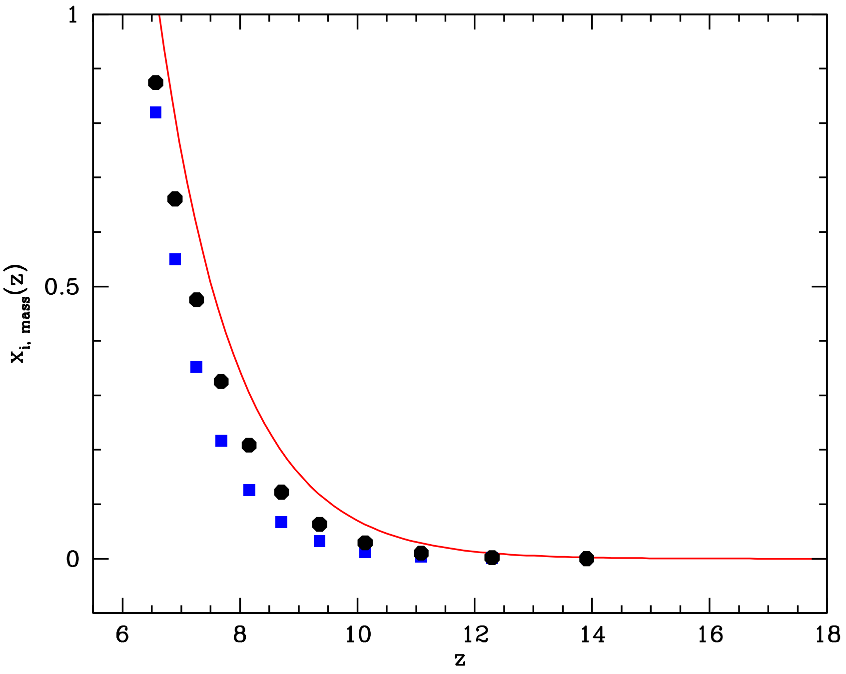

Figure 5.2 Ionization fraction as a function of redshift. The black circles show the mass-weighted ionization fraction from the simulation, while the blue squares show the volume-weighted ionization fraction. The red line is the cumulative number of ionizing photons per hydrogen atom expected for our ionizing sources. The close resemblance between the number of photons per atom and the measured ionization fractions owes to the poor resolution of our radiative transfer calculation, which underestimates the importance of recombinations.

the cumulative number of ionizing photons per Hydrogen atom emitted by our ionizing sources (see the solid red line in Figure 5.2), but this is partly an artifact of the poor resolution of our radiative transfer calculation. Our low grid resolution underestimates the amount of small scale structure in the density field, and hence the importance of recombinations. In the future, we intend to model recombinations as ‘subgrid physics’, accounting for enhancements in the recombination rate owing to unresolved small scale structure (see e.g. [34]). Presently, we caution that we are under-estimating the number of ionizing photons per Hydrogen atom required to complete reionization. Furthermore, we expect reionization to be even more extended than in our calculation, since recombinations should slow the growth of HII regions.

5.3 Numerical scheme based on analytic considerations

As motivated in the introduction, we compare our results with the hybrid scheme inspired by the analytic model of FZH04. In this chapter we only give a brief review of this model and describe a modification we use to be able to better compare it to the radiative transfer simulation. The major advantage of our implementation over a purely analytic calculation is that the hybrid scheme, which amounts to a Monte-Carlo realization of the analytic model, can capture the asphericity of HII regions during reionization.

To remind ourselves briefly, the ionization criterion described in Chapter 2 compares the instantaneous luminosity of sources to the amount of neutral hydrogen present in a region. The criterion was

$$\delta_r \geq \delta_x(m, z) \equiv \delta_c(z) - \sqrt{2}\mathrm{erfc}^{-1}(\zeta^{-1})[\sigma^2(r_{\min}) - \sigma^2(r)]^{1/2}\,. \tag{5.1}$$

For constant mass to light sources, the criterion for a region to self-ionize is modified to capture the integrated flux over collapsed objects at all time instead of the luminosity of the present sources alone

$$\alpha \int_0^t dt' f_{\mathrm{coll.}}(m \geq m_{\min}|\delta_m, t') \geq 1\,, \tag{5.2}$$

where α is an efficiency factor linking halo mass and ionizing photon yield. A region can self-ionize if it is sufficiently overdense to satisfy the inequality in Equation (5.2). In practice we find that the threshold criterion of Equation (5.2) gives quantitatively similar results to that of FZH04, although it produces slightly larger HII regions. We show the new barrier in Figure 5.3, together with a number of ‘random walks’ from our simulation. This content

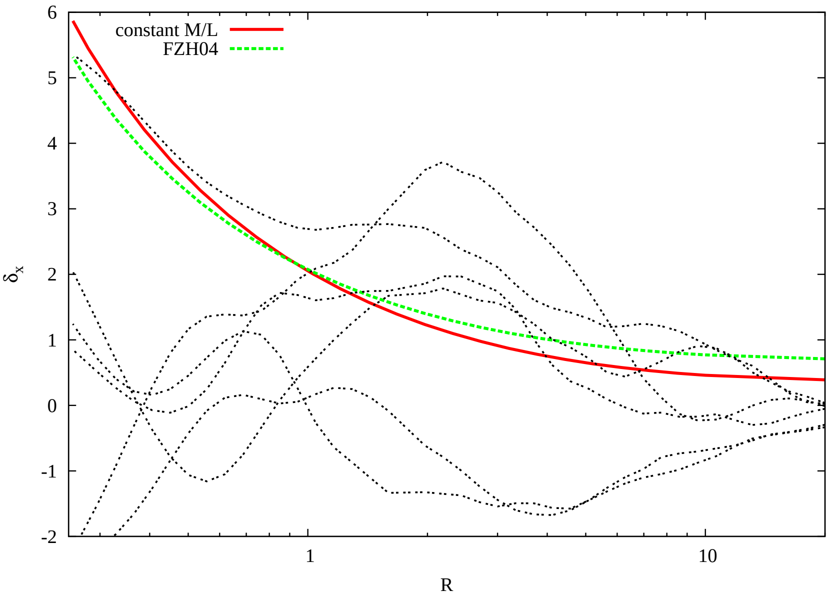

Figure 5.3 Figure comparing the constant mass-to-light barrier with the barrier used in Chapter 4, where the instantaneous luminosity was compared to the amount of neutral hydrogen seen. The new scheme produces slightly larger bubbles, but the difference is not large. Both schemes are extreme examples of what we would expect to see in reality: gas collapsing into halos will take a finite amount of time to be converted into stars, however due to feedback effects we expect the influence of small sources formed at the beginning stages of reionization to cease toward the end.

of this figure is similar to Figure 2.3 in Chapter 2, but complementary in that it plots the smoothed overdensities against the radius of the region of influence of ionizing sources, as opposed to the variance of the density field on that scale.

We described the numerical implementation of our semi-analytic simulations scheme in detail in Chapter 2.

In comparison to our radiative transfer simulation, the hybrid scheme is quite fast: for our present 256^3 grid calculation, with 50 logarithmic smoothing steps, the computation (at a given redshift) takes only $\sim$ 10 minutes on a desktop computer with a 3 GHz processor. This is vastly more efficient than our full radiative transfer calculation: our N-body simulation takes 38 hours to run down to $z \sim 6$ using 134 2 GHz processors, and our post-processing calculation requires a few additional days of running time on a large memory computer. With our rapid numerical scheme, we can produce an ionization map based on the analytic model and compare with our radiative transfer simulations. Using precisely the initial conditions from our N-body simulation in our hybrid calculation allows us to compare radiative transfer and analytic ionization fields on a cell-by-cell basis.

Before presenting this comparison, there are a few more pertinent technical details. Ideally, we would compare the analytic and radiative transfer calculations with identical assumptions regarding the ionizing efficiency of our sources, i.e. we should calibrate α in Equation (5.2) based on the source prescription of Section 5.2.2. In practice there are several difficulties with matching precisely the simulated source prescription. Most importantly, Equation (2.4) is derived assuming sharp k-space filtering, while our smoothing procedure adopts a spherical top-hat in *real space*. This slight inconsistency in our modeling means that our model does not conserve photons precisely, affecting the ionization fraction for a given source efficiency, α (see the Appendix). Further, our simulated mass function is closer to the Sheth-Tormen fitting formula [154] than the Press-Schechter [52] mass function, and we require an analogue of Equation (2.4) for the Sheth-Tormen mass function [45, 57]. We improve on some of these shortcomings in Section 5.5. The upshot of this is that, in order to compare with our radiative transfer simulations, we adjust α in Equation (5.2) at each redshift to match the (volume-weighted) ionization fraction. This readjustment is usually of order 20%.

We show examples of the resulting ionization maps in Figure 5.4. The *left column* shows thin slices through the radiative transfer simulation at three different stages in the reionization process: $z = 8.16$, 7.26 and 6.89 when the (volume-weighted) ionization fraction is $x_{\rm i,v} = 0.13, 0.35$, and 0.55 respectively. The *right column* shows corresponding slices from the hybrid simulation scheme. Several conclusions are immediately apparent.

First, the ionized regions are quite large at the intermediate and late stages of reionization. The ionizing sources are highly clustered, and HII regions quickly start growing collectively around the sources, rapidly reaching much larger sizes than can be achieved by individual sources (FZH04). Second, the hybrid simulation is in good general agreement with the radiative transfer simulation. The hybrid scheme seems to 'locate' the HII regions found in the radiative transfer calculation, and additionally reproduces their general morphology. Third, the HII regions in the analytic calculation are a bit more 'connected' than those in the radiative transfer simulation. Equivalently, the ionization field in the radiative transfer simulation appears to have more small scale structure than the ionization field from the hybrid scheme. In the following sections, we will quantify the visual comparison of Figure 5.4, diagnose differences found, and refine our numerical scheme. We contrast the morphology seen here with that from [35] in Section 5.5.

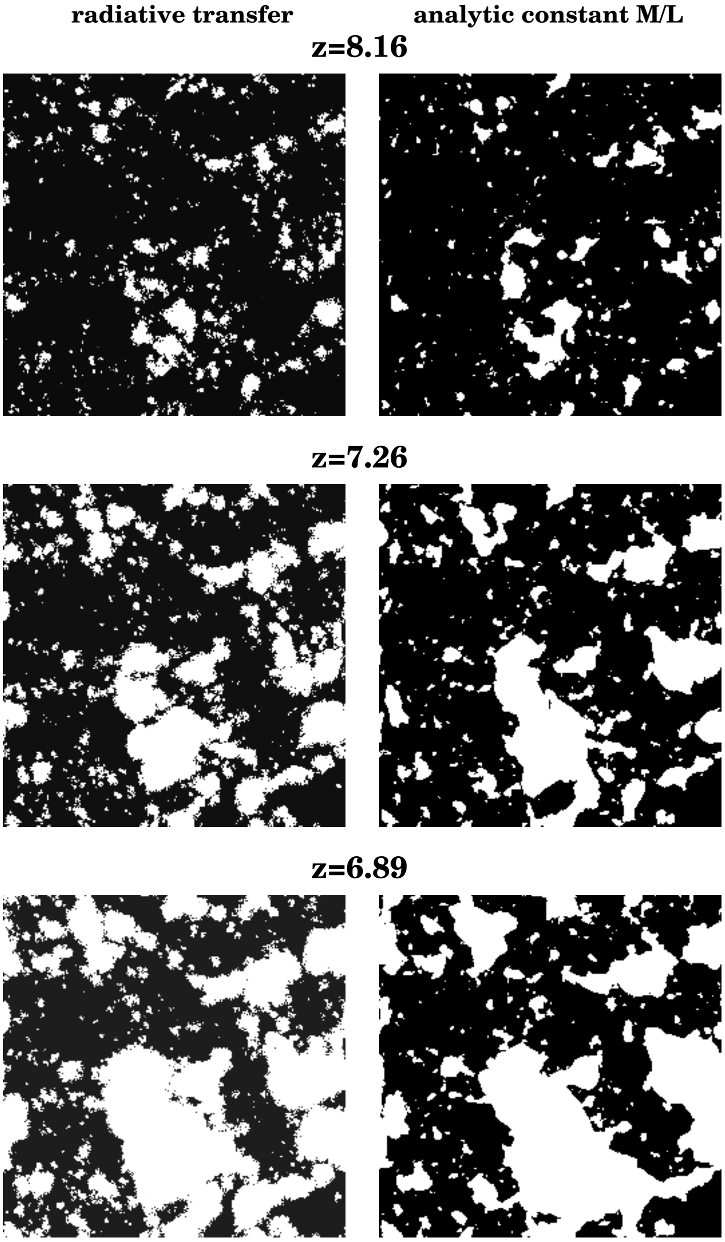

Figure 5.4 Maps of the ionization field. The left column shows HII regions for a thin slice through our radiative transfer simulations at redshifts z=8.16, z=7.26, and z=6.89 (top to bottom). The volume-weighted ionization fraction at these redshifts is $x_{\rm i,v} = 0.13, 0.35$ and 0.55, respectively. The slices are 0.25 Mpc/h deep, and 65.6 Mpc/h on a side. The right panel shows the same using our hybrid simulation scheme, as applied to the initial conditions used in our radiative transfer simulation. The analytic modeling agrees well with the more detailed simulation, although there is more small scale structure in the map from the radiative transfer simulation (see text).

5.4 Statistical Description

In this section we present a detailed statistical description of our results. Throughout we will compare with our hybrid scheme rather than the purely analytic calculations for two reasons. First, there are technical difficulties in the analytic calculations at intermediate ionization fractions [54], and second, we would like to be able to model non-spherical bubble shapes.

5.4.1 The Bubble PDF

The first statistic we consider is the probability distribution of bubble sizes. That is, we calculate how large the HII regions are at different stages of reionization. This depends somewhat on how one chooses to define contiguous ionized volumes – Figure 5.4 clearly illustrates that the ionized regions are not spherical, particularly at the end of reionization. The ionized regions do, however, obtain a reasonably well-defined characteristic size at each redshift. In order to quantify this, we require a convenient and well-motivated definition of 'bubble' that we can apply consistently to the radiative transfer simulation and the hybrid scheme.

Here we adopt a definition of bubble size inspired by the excursion set formalism, upon which our analytic calculation is based (see [35] for an alternate approach). Specifically, we 'draw' spheres around each point in our simulation box of varying radius, R, and average (smooth) the ionization field within each such sphere. We start by considering large spheres, of volume comparable to that of our simulation box, and step downward in size until we eventually get to the size of our simulation pixels. At each smoothing radius, R, we compare the average ionization in each sphere to a threshold ionization, $x_{\rm th}$. A pixel is marked as 'ionized' and belonging to a bubble of radius R, when R is the *largest smoothing radius* at which the pixel's smoothed ionization exceeds the threshold ionization, $x_{\rm th}$. If a given pixel fails to exceed the threshold ionization at all smoothing scales, it is considered neutral (not ionized).

The bubble pdf is then derived by tabulating the fraction of ionized pixels that lie within bubbles with radius between R and $R+dR$. With this convention, the bubble pdf is normalized to unity rather than to the mean ionization fraction. The results of this calculation are shown in Figure 5.5, for an ionization threshold of $x_{\rm th} = 0.9$. The figure illustrates quantitatively the visual impression of Figure 5.4 : the HII regions have a well-defined characteristic size at each stage of reionization, and this characteristic scale evolves as bubbles around neighboring sources overlap and grow collectively (FZH04, [57]). The characteristic scale evolves from sub-Mpc scales at $z = 8.16$, when the

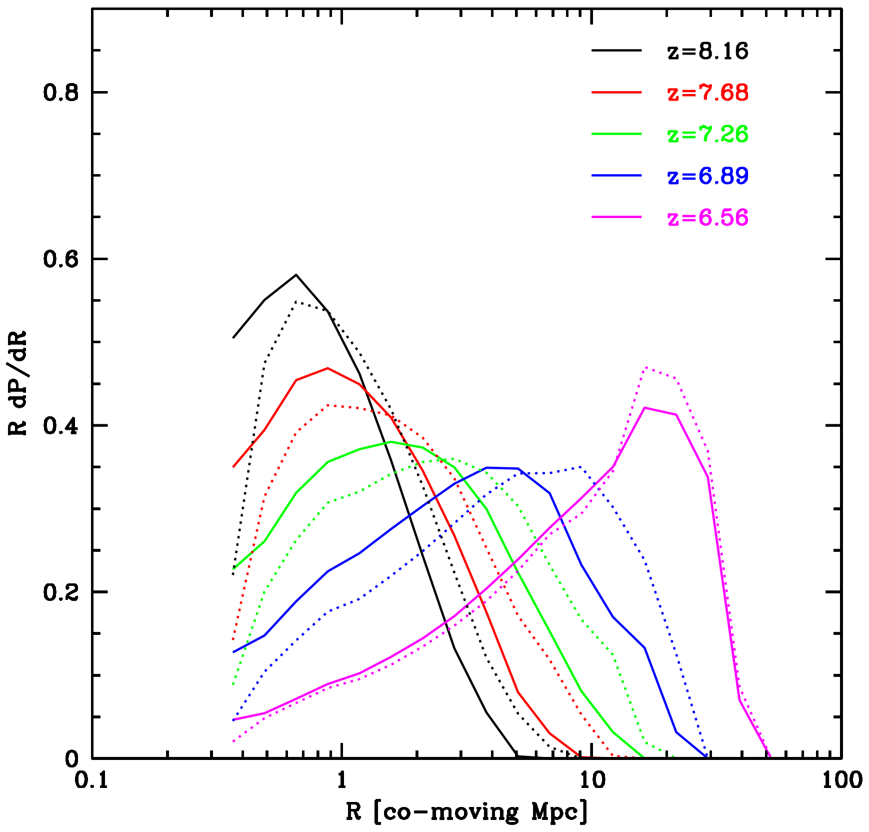

Figure 5.5 Size distribution of HII regions as a function of redshift. The solid curves show results from the radiative transfer simulation, while the dotted curves are from the analytic calculation. We adopt a threshold ionization of $x_{\rm th} = 0.9$ (see text). The volume-weighted ionization fractions at the redshifts shown are $x_{\rm i,v} = 0.13, 0.22, 0.35, 0.55, 0.82$ at $z = 8.16, 7.68, 7.26, 6.89$ and $z = 6.56$ respectively.

volume-weighted ionization fraction is $x_{\mathrm{i,v}} = 0.13$ to $R \gtrsim 10$ Mpc co-moving at $z = 6.56$ when the volume-weighted ionization fraction is $x_{\mathrm{i,v}} = 0.82$. The large size of HII regions at high ionization fraction implies that large volume simulations are required to adequately sample this stage of reionization ([45], FZH04, [35]). The precise value of the characteristic bubble size depends somewhat on the number we adopt for the threshold ionization. For instance, if we instead adopt the less stringent threshold of $x_{\mathrm{th}} = 0.7$, the characteristic size increases by a factor of ~ 2 near $z = 8.16$. Again, while our definition of bubble-size is somewhat arbitrary, the bubbles nevertheless have a well-defined characteristic scale [57], and our algorithm can be applied consistently to each of the analytic model and radiative transfer ionization maps.

The dotted lines indicate that our hybrid scheme reproduces the bubble pdf simulated through radiative transfer quite accurately, roughly matching the characteristic bubble size and its trend with redshift. The hybrid scheme however leads to slightly larger HII regions at all but the final redshift. We will discuss this difference in future sections. At the final redshift, the agreement is almost exact, however here our simulated volume is too small to provide a representative sample.

5.4.2 Power Spectra of the ionized fraction

For further comparison, we measure the (spherically averaged) 3d ionization power spectrum as a function of redshift. We consider the ionization field $\delta_x = x(\vec{r}) - \langle x \rangle$, where $x(\vec{r})$ denotes the ionization at spatial position $\vec{r}$, and $\langle x \rangle$ denotes the volume-averaged ionization. Note that we do not normalize by the mean ionization here, i.e. we consider the absolute ionization fluctuation, rather than the fractional fluctuation. The result of the power spectrum calculation is shown in Figure 5.6, with power spectra calculated from the radiative transfer simulation plotted in red. Throughout this chapter we plot the dimensionless power spectrum, $\Delta^2(k) = k^3 P(k)/(2\pi^2)$, which yields the contribution to the variance per logarithmic interval in k. On large scales at high redshift the ionization power spectrum is proportional to the density power spectrum, while it turns over or flattens on scales in which there are ionized bubbles. Finally, on very small scales ($k \simeq 10\,h\,\mathrm{Mpc}^{-1}$) the power spectra ramp up, an artifact of discreteness noise. The bubble 'feature' moves to progressively larger scales (small k) as reionization proceeds, a further illustration of the bubble growth seen in Figure 5.5. The blue dashed curves show power spectra from our hybrid simulation, which are similar to the radiative transfer power spectra, except with slightly more large scale power, and slightly less small scale power. One can also infer from the figure that

---

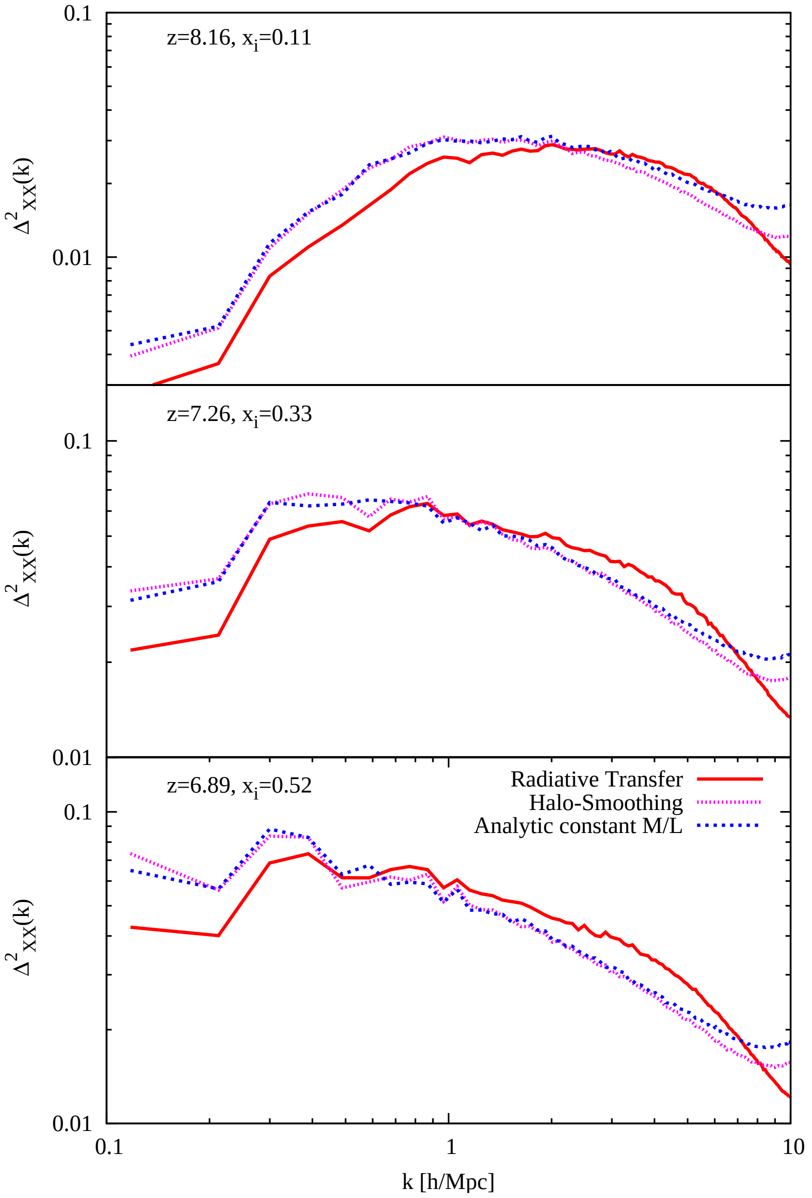

Figure 5.6 Power spectra of the ionized fraction, going from large redshift (small ionization fraction) to small redshift (large ionization fraction). The red lines are from the radiative transfer simulation, the blue dashed lines are from the analytic hybrid calculation, while the purple dotted lines show results from the improved scheme of the next section. The high-k behavior ($k \gtrsim 10h$ Mpc^{-1}) is an artifact from discreteness noise.

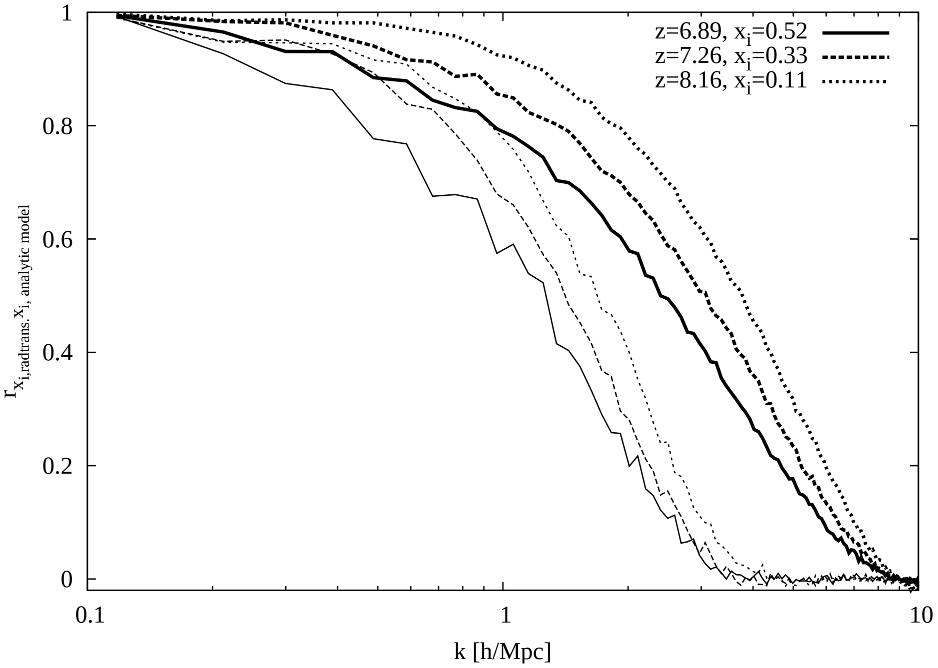

Figure 5.7 Cross correlation coefficient between the ionization fields from the radiative transfer simulation and the analytic model calculations. The thin lines show the cross correlation coefficient between the radiative transfer and hybrid simulations at a few different redshifts. The thick lines show corresponding results from the improved hybrid simulation described in the next section.

an even larger volume simulation is preferable, in order to better sample the large scale ionization power spectrum. Finally, the purple dotted lines are from an improved numerical scheme which we discuss in the next section.

In order to further quantify the agreement between the radiative transfer simulation and the hybrid scheme, we calculate the cross correlation coefficient between the two ionization fields. The cross correlation coefficient is defined by $r(k) = \Delta^2_{\mathrm{x1,x2}}(k) / \left[\Delta^2_{\mathrm{x1}}(k)\Delta^2_{\mathrm{x2}}(k)\right]^{1/2}$. In this equation $\Delta^2_{\mathrm{x1,x2}}(k)$ is the cross power spectrum between the radiative transfer simulation and hybrid scheme ionization fields, while $\Delta^2_{\mathrm{x1}}(k)$, and $\Delta^2_{\mathrm{x2}}(k)$ are their respective power spectra. The cross correlation coefficient is bounded between 1 and -1, with $r(k) = 1$ indicating perfectly correlated modes, and $r(k) = -1$ designating perfectly anti-correlated modes. The results of this calculation are shown as thin lines in Figure 5.7 (ignore, for now, the thick lines which show results from the improved hybrid scheme introduced in the next section).

The correlation coefficient is always larger than $r \sim 0.5$ for scales larger than $k \lesssim 1h$ Mpc^{-1}, while it drops off on smaller scales. This quantifies the qualitative agreement suggested by Figure 5.4: the radiative transfer and hybrid scheme ionization fields trace each other closely on scales larger than $k \lesssim 1h$ Mpc^{-1}. The cross correlation between the two fields becomes slightly weaker at low redshift, as the average ionization increase. A plausible explanation for the slightly worse agreement at low redshift is that our hybrid simulation scheme has difficulty with 'bubble mergers' (see the Appendix), which are more frequent at high ionization fraction.

Why does the cross correlation between the two fields drop off around $k \gtrsim 1h$ Mpc^{-1}? The analytic model assumes a one-to-one correspondence between the abundance of halos and the (Lagrangian) matter overdensity on a given smoothing scale. We know this is inexact. For one, the abundance of our minimum mass sources is $Mdn/dM \lesssim 1$ Mpc^{-3}. On ~ 1 Mpc scales, we therefore expect significant Poisson scatter in the abundance of ionizing sources in our radiative transfer simulation (see also [57, 162]). To explore this further, we compute the cross power spectrum between the halo density field and the matter density field. The cross correlation coefficient between the halo and matter density fields qualitatively mirrors the cross correlation between the two ionization fields seen in Figure 5.7, dropping off at $k \gtrsim 1h$ Mpc^{-1}. In other words, the *halo bias is stochastic* on scales of $k \gtrsim 1h$ Mpc^{-1} for our assumed source population. This stochasticity is not incorporated in our analytic hybrid scheme, and likely leads to the lack of small scale structure compared to the ionization field simulated through radiative transfer. We will return to this issue in Section 5.5. We note here, however, that this Poisson scatter would presumably be less important if our radiative transfer simulation resolved smaller, more abundant galaxies.

The analytic model connects ionized regions with large scale overdensities, which contain more sources and are reionized before underdense regions (FZH04, [45]). The model therefore predicts that the ionization field is positively correlated with the matter density (e.g. McQuinn et al. 2005b), before turning over on scales comparable to that of the ionized bubbles (FZH04). Figure 5.8 shows the cross power spectrum between ionization and density (bottom panel) as well as the cross-correlation coefficient between the two fields. The radiative transfer simulation results (solid lines) nicely mirror the analytic model predictions (dotted lines). In our radiative transfer simulation and hybrid scheme, reionization proceeds inside-out with the overdense regions reionized before underdense regions, as emphasized by FZH04 and Sokasian et al. (2003, 2004). Recombinations, underestimated in our present simulations, could potentially weaken this correlation or, in an extreme case, reverse the correlation with voids ionized first [42]. We intend to explore this in future work.

5.5 Improved numerical scheme

Although the agreement between our radiative transfer simulation and the hybrid scheme is already quite good, we present here a modified numerical scheme that improves upon the one presented in Section 5.3 and [163]. Specifically, we aim to fix two short-comings of the analytic calculation. First, as mentioned previously, the analytic calculation is based on the Press-Schechter formula for the collapse fraction. This formula is derived assuming sharp k-space filtering, while our scheme filters the initial density field with a top-hat in real space, which is slightly inconsistent ([54], the Appendix). Second, the mass function in our radiative transfer simulation (Figure 5.1) is closer to the [154] mass function than the [52] mass function. Finally, the analytic calculation assumes a one-to-one correspondence between initial over-density and halo abundance. As we discussed in Section 5.4.2, the halo bias in our N-body simulation is *stochastic* on small scales.

Each of these shortcomings can be remedied by directly using the simulated halos in our numerical scheme, rather than the Press-Schechter formula for the collapse fraction. More specifically, we place the halo distribution from our N-body simulation on a grid and compare, at each grid cell, the halo mass to the total mass enclosed by a spherical top-hat. We then use a condition analogous to Equation (5.2) to determine whether a region is ionized by the sources within it. In other words, the calculation proceeds exactly as in Section 5.3, except that we use the halo distribution directly from the simulation, rather than Press-Schechter theory. Note further that we now consider the evolved, non-linear density field rather than the initial, linear density field to determine if a region can self-ionize. We will call this improved numerical implementation the 'halo-smoothing' scheme in what follows. The CPU intensity of this scheme is again dominated by the number of FFT's necessary to achieve convergence in the bubble size statistic. As with the analytic scheme, this is roughly 12 minutes on a 3GHz Intel Xeon desktop computer.

The results of this new scheme are shown in comparison with radiative transfer and analytic calculation in Figure 5.11, where we show 21 cm brightness temperature fluctuations (see Section 5.6) for a thin slice through the simulation volume. This is analogous to Figure 5.4, except the ionized regions are now dark, the neutral regions now bright, and fluctuations in the gas density are now visible in the neutral regions. The *left column* shows results from our radiative transfer simulation, the *right column* shows the

---

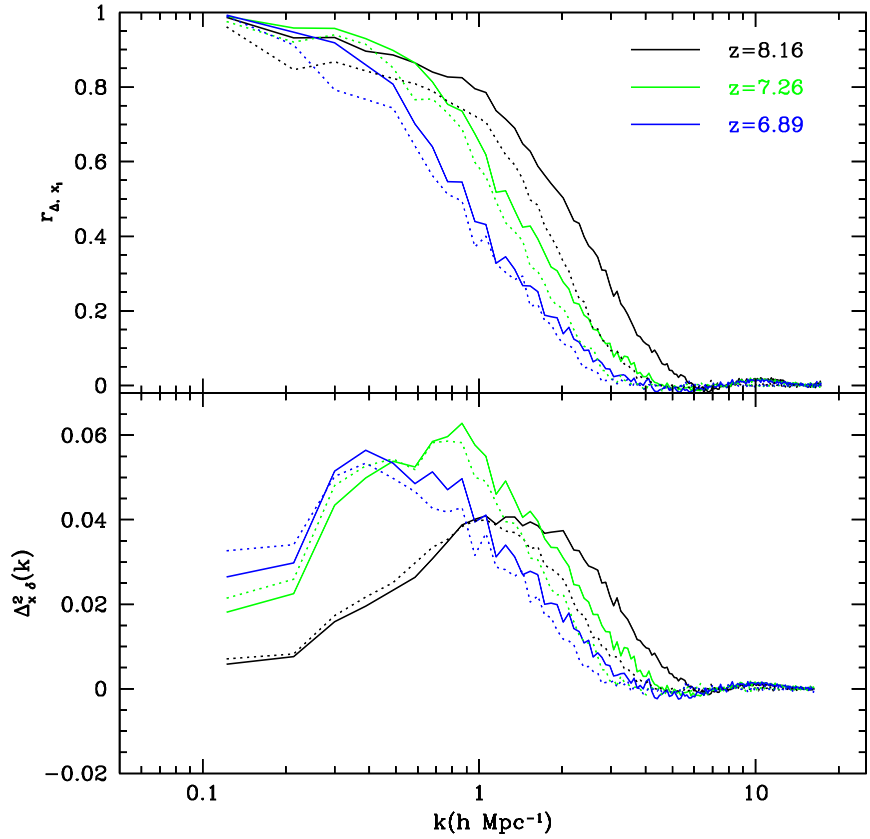

Figure 5.8 *Top panel:* Cross correlation coefficient between the ionization and density field. The solid (dotted) lines show the cross correlation coefficient between the ionization and density fields in the radiative transfer simulation (hybrid scheme) at several redshifts. *Bottom panel:* Cross-power spectrum between the ionization and density field. Solid lines are calculations from the radiative transfer simulation, while dotted lines are from the hybrid scheme.

standard FZH04-type implementation, while the *center column* shows our improved halo-smoothing scheme. The blue dots in the left and center column show the ionizing sources contained in the thin simulation slice. The new scheme clearly resembles the full simulation more closely, with more disconnected ionized regions, owing to the presence of Poisson fluctuations in the source distribution.

Figure 5.6 quantitatively illustrates improved agreement with the radiative transfer calculation, with our improved scheme showing more small scale power than the hybrid simulation scheme. Figure 5.7 additionally shows the cross correlation between the radiative transfer ionization field and the ionization field in the improved numerical scheme (thick lines). The halo-smoothing ionization field traces the ionization field simulated through radiative transfer more closely, and down to smaller scales, than in our initial calculation. We attribute the improved agreement largely to our incorporation, in the improved scheme, of Poisson scatter in the halo abundance.

If the ionizing sources are even less abundant than we assume presently, the Poisson scatter naturally becomes more important. Indeed for sufficiently rare sources, Poisson fluctuations dominate over source clustering on the scale of a typical bubble, and bubble growth is less ‘collective’ than in our fiducial model. In this regime, the morphology of HII regions during reionization may be qualitatively different. To examine this, we repeat our halo-smoothing calculation at $z = 7.26$ including only halos with $m \geq 4 \times 10^{10} M_\odot$ as sources. We adjust the ionizing efficiency of these rarer sources upward to match our usual ionized fraction at this redshift, $x_{\mathrm{i,v}} = 0.35$, in order to compare maps at fixed ionization fraction. The result of this calculation is shown in the left panel of Figure 5.9. One can see that the bubbles are considerably more spherical than in our usual source prescription (middle panel), and that the HII regions have a more sharply defined scale. The left panel further illustrates that for this source prescription there are very few sources in each bubble. Note that this is a thin slice, and some sources contributing to bubble growth lie above or below it.

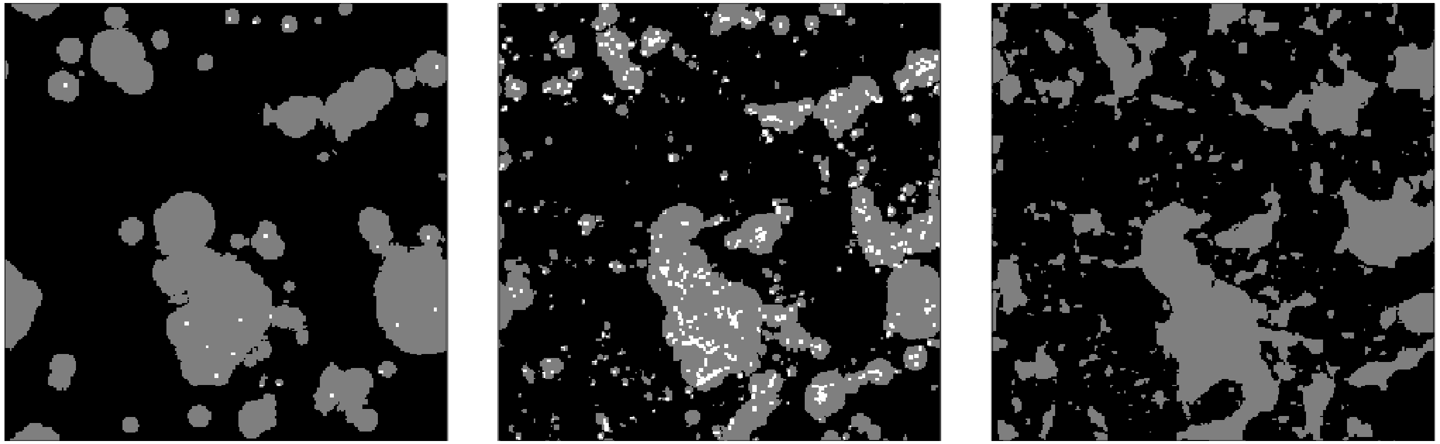

Figure 5.9 Dependence of reionization morphology on source density. In the *left panel* we show the ionization field from our halo-smoothing procedure using only sources (white points) with mass larger than $M \geq 4 \times 10^{10} M_{\odot}$ (note that some sources contributing to the ionized regions lie in front or behind the thin slice shown). With this choice, the number density of sources roughly matches that of $M \geq 2 \times 10^{9} M_{\odot}$ sources at $z \sim 14$ (as in [35]). The *center panel* shows the result with our usual source prescription, indicating a significantly more complex morphology. Finally the *right panel* shows, for comparison, the analytic model with $M_{\rm min} = 10^{8} M_{\odot}$. Each panel is at $z = 7.26$, and in each case the source efficiencies are adjusted to match $x_{\rm i,v} = 0.35$.

Furthermore, the left panel qualitatively resembles the morphology seen in the reionization simulations of [35] (see their Figure 8[3]). Their simulations are done at higher redshift, but have a similar source number density as our present, extreme choice of $m \geq 4 \times 10^{10} M_{\odot}$ (with this choice our simulation volume contains roughly 5,000 sources at z=7.26). We regard the morphology seen in [35] as artificial and unlikely to represent the true morphology of HII regions during reionization. Their choice of minimum source mass ($M_{\rm min} = 2.5 \times 10^9 M_{\odot}$) is driven by the low mass resolution of their simulations, and the efficiency of their ionizing sources is boosted extremely high in order to match first-year WMAP constraints [6]. In other words, their simulation represents a very extreme case of reionization by rare, bright sources. Our simulation is also missing plausible ionizing sources, given our comparable minimum source mass. However, owing to the different assumptions about the ionizing efficiency in our simulation, reionization occurs later and so our sources are much more abundant (265,000 sources in the simulation volume at z=7.26). We are hence still in the regime where HII regions grow collectively, and we expect only small modifications to the morphology and size distribution of HII regions when we include still smaller mass sources. This is illustrated in the right panel of Figure 5.9 where we show predictions for our original hybrid scheme (Section 5.3), with the minimum source mass extended down to the cooling mass, $M_{\rm min} \sim 10^8 M_{\rm sun}$. While there are some differences with the results from our usual source prescription (center panel), the differences are clearly far smaller than in comparison to the Poisson-dominated case (left panel). The differences with [35] highlight the utility of our fast numerical schemes for quickly examining many different prescriptions for the ionizing sources and for understanding the robustness of the results.

5.6 21 cm signal and power spectra

The statistics discussed in Section 5.4 are largely diagnostic, aimed at describing the size distribution of HII regions in the simulation, and characterizing the agreement between the radiative transfer simulation and analytic calculations. In this section we make a more observationally relevant comparison, contrasting radiative transfer and analytic 21 cm power spectra.

We reviewed the theory of 21 cm fluctuations in Chapter 2. At the redshifts we consider presently, the 21 cm excitation temperature is likely coupled to the gas temperature, and much larger than the temperature of the CMB (e.g. [67, 164, 73]), $T_S >> T_{\rm CMB}$, implying $\delta T \propto (1 + \delta_s) x_H$. We then

---

[3] Note for comparison with these authors' figure: their simulation box has a side length of $L = 100$ Mpc/h, while ours has $L = 65.6$ Mpc/h.

model the 21 cm brightness temperature using the simulated density and peculiar velocity fields, in conjunction with radiative transfer/analytic calculation simulated ionization fields. We incorporate here the effect of redshift space distortions, taking into account the simulated peculiar velocity field. On large scales, linear infall boosts the spherically averaged 21 cm redshift power spectrum relative to its real space analogue, analogous to the ‘Kaiser effect’ in galaxy surveys [165, 78, 80, 76].

The result of our power spectrum calculation is shown in Figure 5.10 for three different redshifts during reionization. The results are qualitatively similar to those of Figure 5.6, and can be roughly understood by decomposing the 21 cm power spectrum into three constituent pieces (FZH04):

$$\Delta^2_{21}(k) \quad = \quad \overline{T}_b[\Delta^2_{\rm xx}(k) - \frac{10}{3}\bar{x}_H\Delta^2_{{\rm x}\delta}(k) + \frac{28}{15}\bar{x}_H^2\Delta^2_{\delta\delta}(k)]\,. \tag{5.3}$$

Here $\Delta^2_{\rm xx}$ refers to the ionization power spectrum, $\Delta^2_{{\rm x}\delta}$ refers to the ionization-density cross power spectrum, and $\Delta^2_{\delta\delta}$ refers to the density power spectrum. Note that, for illustrative purposes we ignore higher order terms [54, 57], although their effects are included in our calculations. The numerical coefficients in this decomposition come from angle-averaging the redshift space power spectrum. On scales much larger than the size of the ionized bubbles, each term in this decomposition is directly proportional to the density power spectrum, and so the 21 cm power spectrum is directly proportional to the density power spectrum. On the other hand, on very small scales one would expect that the 21 cm power spectrum approaches the density power spectrum multiplied by the neutral fraction squared (and a constant factor $\simeq 1.87$ for the spherically averaged redshift space case). The latter is shown in the thin dashed curves in the Figure. The discrepancy see is due to the significance of higher order terms that were neglected in Equation 5.3, that in reality amount to corrections of order one.

These qualitative trends can be seen in Figure 5.10. For further illustration, we extrapolate our predictions to large scales using an analytic model hybrid simulation (green long-dashed lines) which we based on a Gaussian random field with sidelength 300 Mpc/h.

At high redshift, where the ionized regions are small, the 21 cm power spectrum has the shape of the density power spectrum. It is evident that the power spectrum does not trace the density power spectrum (or its rescaled version $P_\delta x_H^2 1.87$) exactly, as we would have naively expected. The reason for this departure (in fact it is between 50% and 100% in the Figure shown) lies in the importance of the higher order terms in Equation 2.26. The three point terms are negative in the case of inside-out reionization, which explains

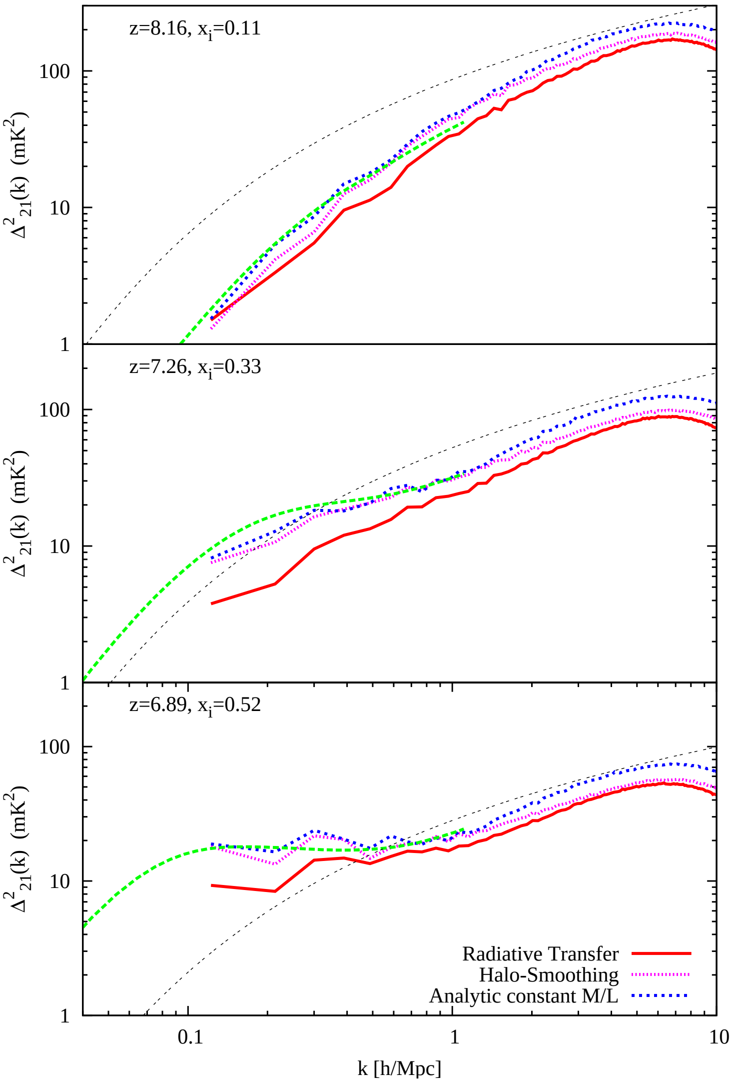

Figure 5.10 The 21 cm brightness temperature power spectra in redshift space. The solid red, short-dashed blue and dotted purple lines show the radiative transfer, analytic, and halo-smoothing power spectra, respectively. The green long-dashed lines show extrapolations of the analytic predictions to large scales. Some of the differences in the predictions on large scales may be attributable to our limited simulation volume. The redshift space 21 cm power spectrum approaches $P_\delta x_H^2 1.87$ (shown in the thin dashed curve) on small scales. The differences seen are due to the relevance of higher order contributions to the 21 cm power spectrum (see upcoming work).

the discrepancy. We discuss this topic in a separate work not presented in this thesis [77].

At lower redshifts, the 21 cm power spectrum begins to flatten on large scales owing to the presence of ionized regions, before following the shape of the density power spectrum again on small scales. This flattening moves to progressively larger scales as reionization proceeds, and the bubbles grow larger. Our first observational handle on the characteristic sizes of HII regions at different stages of reionization will likely come from measuring the 21 cm power spectrum, and observing this flattening. In other work, we will explore the extent to which the size distribution of HII regions can be extracted from future measurements of the 21 cm power spectrum (Zahn et al., in prep.).

Notice that the agreement between the analytic and radiative transfer 21 cm power spectra is even better than the agreement between the ionization power spectra. While the ionization field in the radiative transfer simulation has more small scale power than the analytic model ionization field, the different approaches show similar amounts of small scale 21 cm power. This owes to the small-scale dominance of the $\Delta^2_{\delta\delta}(k)$ term in the 21 cm power spectrum, which overwhelms the difference in small scale ionization power (see Figure 5.6). The 21 cm power spectrum in each analytic scheme seems to provide a very good approximation to the results of our full radiative transfer simulations. Some of the difference on large scales may be attributable to our limited simulation volume, and a convergence test with increasing boxsize would be informative, but we leave this to future work.

5.7 Conclusions and Outlook

In this final chapter, we have presented results from a large volume radiative transfer simulation and our fast numerical scheme based on analytic considerations, as well as an improved scheme which is based on the dark matter halos found in the simulation. We have given a detailed comparison of the three different reionization modeling schemes. Our basic conclusion is that the approximate schemes agree remarkably well with the radiative transfer simulation.

Future work should investigate the effect of recombinations which, we anticipate, will lead to two primary modifications [55]. First, recombinations will slow down reionization by requiring more ionizing photons to achieve a given ionization fraction. This should mainly act to modify the redshift evolution of the ionization fraction, and not the size distribution of HII regions at a given ionization fraction, our main focus in the present work. Second, ionization fronts may be halted upon impacting dense clumps, where the re-

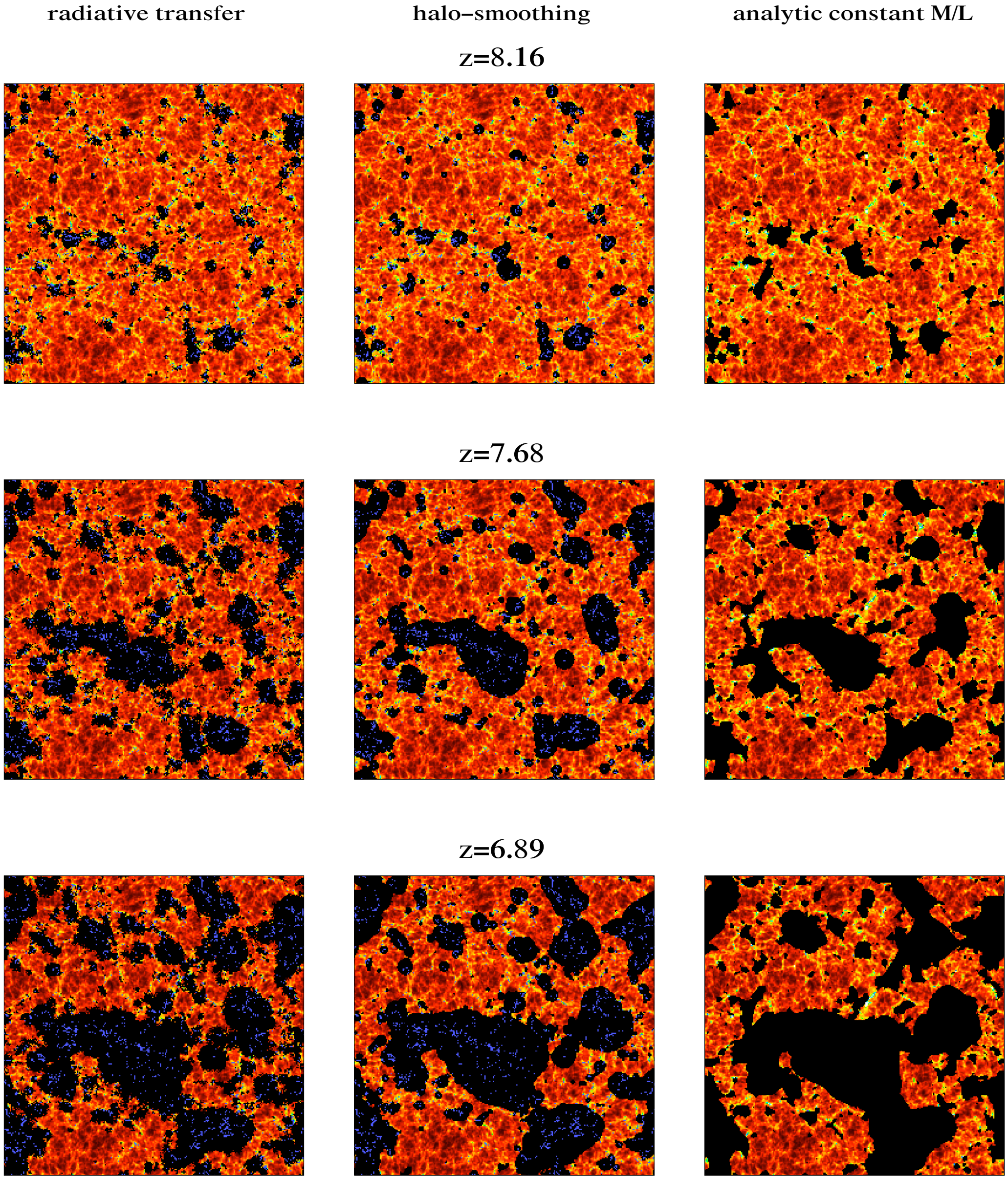

Figure 5.11 21 cm brightness temperature fluctuations. We compare 21 cm maps from the radiative transfer simulation and numerical scheme at three different redshifts. Each map is 65.6 Mpc/h on a side, and 0.25 Mpc/h deep, comparable to the frequency resolution of planned experiments, and shows a different cut then Figure 5.4. The ionized fractions are $x_{\rm i,V} = 0.13, 0.35$ and 0.55 for $z = 8.16, 7.26$ and 6.89 respectively. *Left column:* Radiative transfer calculation with ionizing sources (blue dots). *Middle column:* Halo-smoothing procedure (see text) with sources/halos from the N-body simulation. *Right column:* Constant mass-to-light ratio version of FZH04, based purely on the initial, linear dark matter overdensity.

combination rate is very high (e.g. [42, 147, 55]). This latter effect might, indeed, modify the size distribution of HII regions at a given ionization fraction. However, as long as mini-halos are destroyed by pre-heating prior to reionization (e.g. [20]), estimates show this effect is important only at the tail end of reionization, when $x_{\rm i,v} \gtrsim 0.85$ [55], which we do not presently simulate.

In the future we will address these issues explicitly, along with other refinements to our radiative transfer simulations. We intend to consider a more sophisticated prescription for the ionizing sources [166, 32], and extend the mass range of our sources down to the cooling mass. It will be interesting to examine how sensitive the 21 cm predictions are to the assumed properties of the ionizing sources [57]. In particular, in Section 5.5 we found that the morphology and size distribution of HII regions differs dramatically from our fiducial model when extremely rare, bright sources dominate. This warrants further quantitative investigation. Finally, we intend to examine the effect of feedback on reionization, incorporating Jeans mass suppression (e.g. [43, 109, 167]) in reionized regions of the IGM.

In spite of these refinements, we contend that the agreement demonstrated illustrates that the analytic models are on the right track, and provide a useful complementary tool to radiative transfer simulations. The approximate schemes described here are very fast, allowing quick coverage of a large parameter space, convenient for forecasting constraints from upcoming 21 cm surveys (Zahn et al. in prep). Even full radiative transfer simulations currently have a large number of free parameters related to the efficiency of the ionizing sources, the escape fraction of ionizing photons, and sub-grid clumping. Our numerical schemes allow one to gauge how the expected signal depends on these numerous, unconstrained parameters. It can also be used to investigate non-Gaussianities in the 21 cm signal, as advocated by [168], and to construct mock 21 cm survey volumes, providing a useful test of data analysis procedures, which are presently still under development. This is particularly relevant given that surveys like the MWA will be done in large volumes of several co-moving cubic Gigaparsecs, prohibitive for current radiative transfer simulations, but manageable with analytic calculations. Finally, it might be interesting to couple the fast analytic model schemes with a gas-dynamical calculation to investigate the impact of reionization on galaxy formation.

5.8 Appendix: Photon Conservation in our approximate simulation schemes

The objective of this Appendix is to show that the pure FZH04 model conserves photons, but that our numerical schemes do not precisely conserve photons. We then discuss the implications of this finding. In the pure FZH04 model, we can prove that the global ionization fraction is given by $\bar{x} = \zeta \times f_{\rm coll.}$. This is just a reflection of photon conservation: as we sum up the total ionized mass from individual HII regions, no photons are lost or gained in our accounting of the net ionized mass.

A rigorous proof proceeds as follows. For simplicity, we outline this proof using the pure FZH04 barrier, but the proof can be easily generalized to the barrier of Equation (5.2). Let us consider random walks in the (δ, σ^2) plane (e.g. Bond et al. 1991), generated using top-hat smoothing in k-space. We consider the first up-crossing distributions for two types of barriers. First, we examine the probability that a random walk crosses the 'bubble barrier', representing the critical density threshold for a region to self-ionize (see Figure 1 of FZH04). We denote the differential probability that a random walk crosses this barrier, at a resolution between σ^2 and $\sigma^2 + d\sigma^2$, by $dP_b/d\sigma^2$. Next, we consider the ordinary Press-Schechter barrier, representing the critical overdensity for a region to collapse and form a halo. The differential probability distribution for a random walk to cross the 'collapse barrier', at a resolution between σ'^2 and $\sigma'^2 + d\sigma'^2$, is denoted by $dP_c/d\sigma'^2$. Similarly, the probability distribution for collapse in a region with large-scale overdensity δ_b, on smoothing scale σ^2, is denoted by $dP_c(\sigma'^2|\delta_b, \sigma^2)/d\sigma'^2$. The total ionized mass in a region of large scale overdensity δ_b, at a smoothing scale σ^2, is then given by

$$\int dM_h \, \zeta \, M_h \, \frac{d\sigma'^2}{dM_h} \frac{dP_c(\sigma'^2|\delta_b, \sigma^2)}{d\sigma'^2} \, . \tag{5.4}$$

Note that the conditional probability distribution in this formula is calculated by considering the fraction of random walks, originating at (δ_b, σ^2), that cross the collapse barrier at higher resolution (Lacey & Cole 1993). The mass calculated using Equation (5.4) is precisely the ionized mass in an HII region that crosses the 'bubble barrier' at the point (δ_b, σ^2). In order to find the total ionized mass in all HII regions, we merely need to integrate over all such crossings, i.e., we integrate Equation (5.4) over σ^2 weighted by the probability of crossing the bubble barrier. Symbolically, the total ionized mass in the IGM is then given by

$$\int d\,\sigma^2 \, \frac{dP_b(\sigma^2)}{d\sigma^2} \int dM_h \, \zeta \, M_h \, \frac{d\sigma'^2}{dM_h} \frac{dP_c(\sigma'^2|\delta_b, \sigma^2)}{d\sigma'^2} \, . \tag{5.5}$$

This is one expression for the total ionized mass in the IGM, obtained by summing the ionized mass in all individual HII regions. Our proof of photon conservation is completed by showing that this 'local' expression matches a separate expression, proportional to the global collapse fraction. The total mass in halos is simply

$$\int dM_h \, M_h \, \frac{d\sigma'^2}{dM_h} \frac{dP_c(\sigma'^2)}{d\sigma'^2} \, , \tag{5.6}$$

and the total, photon-conserving, ionized mass is just ζ times this expression. Now, this expression, proportional to the global collapse fraction follows by considering the crossing distribution of the collapse barrier, *irrespective* of when each random walk crosses the bubble barrier. This result clearly must match that of Equation (5.4) since for two random variables, x and y with probability distributions $P(x)$ and $P(y)$, $\int dyP(y) \int dxxP(x|y) = \int dxxP(x)$, i.e. in one case we are integrating ('marginalizing') over 'bubble crossings', and in the other case we are not. This proves that the pure FZH04 model conserves photons, and our numerical implementation of the FZH04 model with a sharp k-space filter indeed conserves photons.

In practice, however the hybrid scheme of Section 5.3 smoothes the density field with a top-hat in real space, rather than a sharp k-space filter. In this case photon conservation is not guaranteed. Specifically, the expression in Equation (**??**) of Section5.3 is rigorously equal to the collapse fraction only for sharp k-space filtering, and not for real-space smoothing (see also [54]). One option would be to simply apply our algorithm with a sharp k-space filter, but we find that this produces artificial features in our ionization maps (ringing in configuration space). For this reason, we prefer to apply our algorithm using a top-hat in real space. In practice this leads to photon non-conservation at the 20% level, with our algorithm systematically under-shooting the expected ionization, $\bar{x} = \zeta \times f_{\rm coll.}$. To compare with the radiative transfer simulation, we simply boost the ionizing efficiency to make up for this photon loss, matching the (volume-weighted) ionization fraction in the radiative transfer simulation.

Is photon-conservation fulfilled in our improved 'halo-smoothing' scheme? We consider a simple toy problem to illustrate that our improved scheme also does not quite conserve photons. Imagine two equal luminosity sources in a uniform density field. When the ionized regions surrounding these sources begin to overlap, the spherical top-hat criterion can lead to somewhat unphysical features. This is sketched in the left panel of Figure 5.12. Our algorithm does not allow for flux from one source to expand the HII region surrounding the second source. Instead of both HII spheres (with initial radius r_1) growing further during overlap, a new ionized region arises between them, the overlap of two spheres with radius $r_2 = 2^{1/3} r_1$. In Figure 5.12 we plot the ratio of the ionized volume in our scheme, to the expected, photon-conserving ionized volume. The figure clearly illustrates that our scheme generally loses photons as two bubbles 'merge'. The precise level of photon loss in our 'halo-smoothing' scheme will depend on the ionized fraction, the size distribution of the HII regions, the luminosity and bias of the sources interior to merging bubbles, and the rate of merging bubbles. In practice, the level of photon non-conservation in our halo-smoothing scheme is also at the 20% level. Again our solution is to uniformly boost the ionizing efficiency of our sources to match the (volume-weighted) ionization fraction in the radiative transfer simulation. Ideally, we would only boost the efficiency in recently merged bubbles where we expect photon loss. In practice, any error associated with this approximation appears small, although the higher frequency of bubble mergers at late stages of reionization makes our scheme slightly less reliable in this regime (see Figure 5.7).

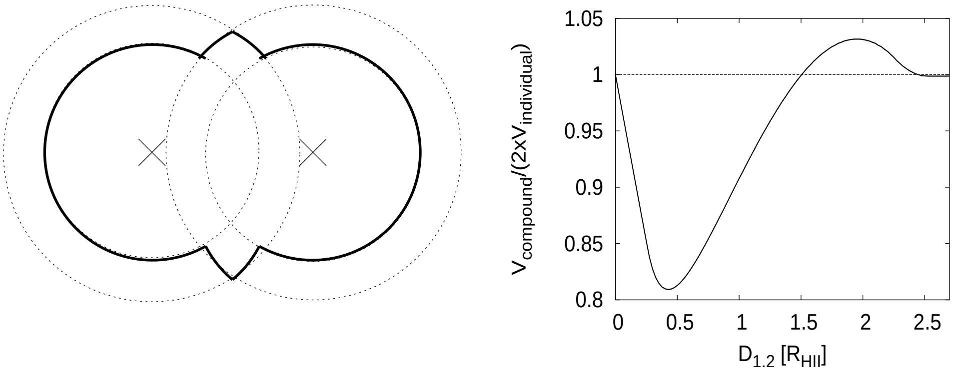

Figure 5.12 An illustration of photon non-conservation in our 'halo-smoothing' simulations. The *left panel* shows the ionized region from our numerical scheme for the toy problem of two equal-luminosity sources. Our scheme leads to the HII region denoted by the thick solid boundary. In reality, one expects an oblong HII region, as photons from each source stream to the edge of the HII region created by the other source, and expand its volume. For this toy problem, our procedure initially over-estimates the ionized volume by a few percent at moderate source separations, then under-estimates the ionized volume at smaller separations. In the limit of non-overlapping HII regions (very large source separations), and in the limit of very small source separations, we recover the expected ionized volume. This is illustrated in the *right panel* which shows the fractional photon loss/gain as a function of source separation. The x-axis is the source separation in units of the radius of an individual HII region.

Bibliography

[1] G. F. Smoot *et al.*, "Structure in the COBE differential microwave radiometer first year maps," *Astrophys. J.*, vol. 396, pp. L1–L5, 1992.

[2] A. E. Lange *et al.*, "Cosmological parameters from the first results of BOOMERANG," *Phys. Rev.*, vol. D63, p. 042001, 2001.

[3] D. N. Spergel *et al.*, "First-Year Wilkinson Microwave Anisotropy Probe (WMAP) Observations: Determination of Cosmological Parameters," *Astrophys. J. Supp.* , vol. 148, pp. 175–194, Sept. 2003.

[4] A. H. Guth, "The inflationary universe: A possible solution to the horizon and flatness problems," *Phys. Rev.*, vol. D23, pp. 347–356, 1981.

[5] A. D. Linde, "A new inflationary universe scenario: A possible solution of the horizon, flatness, homogeneity, isotropy and primordial monopole problems," *Phys. Lett.*, vol. B108, pp. 389–393, 1982.

[6] A. Kogut *et al.*, "First-Year Wilkinson Microwave Anisotropy Probe (WMAP) Observations: Temperature-Polarization Correlation," *Astrophys. J. Supp.* , vol. 148, pp. 161–173, Sept. 2003.

[7] L. e. a. Page, "Three Year Wilkinson Microwave Anisotropy Probe (WMAP) Observations: Polarization Analysis," *ArXiv Astrophysics e-prints astro-ph/0603450*, Mar. 2006.

[8] X. Fan *et al.*, "Constraining the Evolution of the Ionizing Background and the Epoch of Reionization with z˜6 Quasars. II. A Sample of 19 Quasars," *Astron. J.* , vol. 132, pp. 117–136, July 2006.

[9] A. G. Riess *et al.*, "Observational Evidence from Supernovae for an Accelerating Universe and a Cosmological Constant," *Astron. J.*, vol. 116, pp. 1009–1038, 1998.

[10] S. Perlmutter *et al.*, “Measurements of Omega and Lambda from 42 High-Redshift Supernovae,” *Astrophys. J.*, vol. 517, pp. 565–586, 1999.

[11] M. J. Geller and J. P. Huchra, “Mapping the universe,” *Science*, vol. 246, pp. 897–903, 1989.

[12] M. Tegmark *et al.*, “Cosmological parameters from SDSS and WMAP,” *Phys. Rev.*, vol. D69, p. 103501, 2004.

[13] S. Malhotra and J. E. Rhoads, “The Volume Fraction of Ionized Intergalactic Gas at Redshift z=6.5,” *Ap. J. L.*, vol. 647, pp. L95–L98, Aug. 2006.

[14] D. N. Spergel *et al.*, “Wilkinson Microwave Anisotropy Probe (WMAP) three year results: Implications for cosmology,” *astro-ph/0603449*, 2006.

[15] J. S. B. Wyithe and A. Loeb, “A large neutral fraction of cosmic hydrogen a billion years after the Big Bang,” *Nature*, vol. 427, pp. 815–817, Feb. 2004.

[16] T. Theuns *et al.*, “Constraints on Reionization from the Thermal History of the Intergalactic Medium,” *Ap. J. L.*, vol. 567, pp. L103–L106, Mar. 2002.

[17] L. Hui and Z. Haiman, “The Thermal Memory of Reionization History,” *Ap. J.* , vol. 596, pp. 9–18, Oct. 2003.

[18] A. Sokasian, T. Abel, and L. Hernquist, “The epoch of helium reionization,” *MNRAS* , vol. 332, pp. 601–616, May 2002.

[19] S. R. Furlanetto, M. Zaldarriaga, and L. Hernquist, “The Effects of Reionization on Lyman-alpha Galaxy Survey,” *Mon. Not. Roy. Astron. Soc.*, vol. 365, pp. 1012–1020, 2006.

[20] S. P. Oh and K. J. Mack, “Foregrounds for 21-cm observations of neutral gas at high redshift,” *MNRAS* , vol. 346, pp. 871–877, Dec. 2003.

[21] P. Madau, A. Meiksin, and M. J. Rees, “21-cm Tomography of the Intergalactic Medium at High Redshift,” *Astrophys. J.*, vol. 475, p. 429, 1997.

[22] M. Zaldarriaga, S. R. Furlanetto, and L. Hernquist, “21 centimeter fluctuations from cosmic gas at high redshifts,” *Astrophys. J.*, vol. 608, pp. 622–635, 2004.

[23] M. Tegmark *et al.*, “Cosmological Constraints from the SDSS Luminous Red Galaxies,” *astro-ph/0608632*, 2006.

[24] G. D. Becker, W. L. W. Sargent, M. Rauch, and R. A. Simcoe, “Discovery of excess O I absorption towards the z = 6.42 QSO SDSS J1148+5251,” *Astrophys. J.*, vol. 640, pp. 69–80, 2006.

[25] R. Barkana and A. Loeb, “GRBs versus Quasars: Lyman-alpha Signatures of Reionization versus Cosmological Infall,” *Astrophys. J.*, vol. 601, pp. 64–77, 2004.

[26] T. Totani, N. Kawai, G. Kosugi, K. Aoki, T. Yamada, M. Iye, K. Ohta, and T. Hattori, “Implications for Cosmic Reionization from the Optical Afterglow Spectrum of the Gamma-Ray Burst 050904 at z = 6.3,” *Ap. J.* , vol. 58, pp. 485–498, June 2006.

[27] J.-P. Kneib, R. S. Ellis, M. R. Santos, and J. Richard, “A probable z 7 galaxy strongly lensed by the rich cluster abell 2218: Exploring the dark ages,” *Astrophys. J.*, vol. 607, pp. 697–703, 2004.

[28] N. Y. Gnedin and J. P. Ostriker, “Reionization of the Universe and the Early Production of Metals,” *Ap. J.* , vol. 486, Sept. 1997.

[29] N. Y. Gnedin, “Cosmological reionization by stellar sources,” *Ap. J.* , vol. 535, pp. 530–554, 2000.

[30] A. O. Razoumov, M. L. Norman, T. Abel, and D. Scott, “Cosmological Hydrogen Reionization with Three-dimensional Radiative Transfer,” *Ap. J.* , vol. 572, pp. 695–704, June 2002.

[31] B. Ciardi, F. Stoehr, and S. D. M. White, “Simulating intergalactic medium reionization,” *MNRAS* , vol. 343, pp. 1101–1109, Aug. 2003.

[32] A. Sokasian, T. Abel, L. Hernquist, and V. Springel, “Cosmic reionization by stellar sources: Population II stars,” *MNRAS* , vol. 344, pp. 607–624, Sept. 2003.

[33] A. Sokasian, N. Yoshida, T. Abel, L. Hernquist, and V. Springel, “Cosmic reionization by stellar sources: population III stars,” *MNRAS* , vol. 350, pp. 47–65, May 2004.

[34] K. Kohler, N. Y. Gnedin, and A. J. S. Hamilton, “Large-Scale Simulations of Reionization,” *astro-ph/0511627*, 2005.

[35] I. T. Iliev, G. Mellema, U.-L. Pen, H. Merz, P. R. Shapiro, and M. A. Alvarez, “Simulating cosmic reionization at large scales - I. The geometry of reionization,” *MNRAS* , vol. 369, pp. 1625–1638, July 2006.

[36] O. Zahn *et al.*, “Simulations and Analytic Calculations of Bubble Growth During Hydrogen Reionization,” *astro-ph/0604177*, 2006.

[37] R. Cen, “Implications of WMAP Observations On the Population III Star Formation Processes,” *Astrophys. J.*, vol. 591, pp. L5–L8, 2003.

[38] M. Zaldarriaga, “Polarization of the microwave background in reionized models,” *Phys. Rev.*, vol. D55, pp. 1822–1829, 1997.

[39] P. Madau and M. J. Rees, “The Earliest Luminous Sources and the Damping Wing of the Gunn-Peterson Trough,” *Ap. J. L.*, vol. 542, pp. L69–L73, Oct. 2000.

[40] X. Fan, V. K. Narayanan, M. A. Strauss, R. L. White, R. H. Becker, L. Pentericci, and H.-W. Rix, “Evolution of the Ionizing Background and the Epoch of Reionization from the Spectra of z˜6 Quasars,” *Astron. J.* , vol. 123, pp. 1247–1257, Mar. 2002.

[41] M. Dijkstra, Z. Haiman, and A. Loeb, “A Limit from the X-ray Background on the Contribution of Quasars to Reionization,” *Astrophys. J.*, vol. 613, pp. 646–654, 2004.

[42] J. Miralda-Escudé, M. Haehnelt, and M. J. Rees, “Reionization of the Inhomogeneous Universe,” *Ap. J.* , vol. 530, pp. 1–16, Feb. 2000.

[43] R. Barkana and A. Loeb, “In the beginning: the first sources of light and the reionization of the universe,” *Phys. Rep.* , vol. 349, pp. 125–238, July 2001.

[44] S. Furlanetto, A. Sokasian, and L. Hernquist, “Observing the Reionization Epoch Through 21 Centimeter Radiation,” *Mon. Not. Roy. Astron. Soc.*, vol. 347, p. 187, 2004.

[45] R. Barkana and A. Loeb, “Unusually large fluctuations in the statistics of galaxy formation at high redshift,” *Astrophys. J.*, vol. 609, pp. 474–481, 2004.

[46] P. R. Shapiro, M. L. Giroux, and A. Babul, “Reionization in a cold dark matter universe: The Feedback of galaxy formation on the intergalactic medium,” *Astrophys. J.*, vol. 427, p. 25, 1994.

[47] X. Wang, M. Tegmark, M. Santos, and L. Knox, “Twenty-one centimeter tomography with foregrounds,” *Submitted to PRD (astro-ph/0501081)*, 2005.

[48] A. Cooray and R. Sheth, “Halo models of large scale structure,” *Phys. Rep.* , vol. 372, pp. 1–129, Dec. 2002.

[49] J. R. Bond, S. Cole, G. Efstathiou, and N. Kaiser, “Excursion set mass functions for hierarchical Gaussian fluctuations,” *Ap. J.* , vol. 379, pp. 440–460, Oct. 1991.

[50] S. R. Furlanetto, M. Zaldarriaga, and L. Hernquist, “The Growth of H II Regions During Reionization,” *Ap. J.* , vol. 613, pp. 1–15, Sept. 2004.

[51] C. Lacey and S. Cole, “Merger rates in hierarchical models of galaxy formation,” *MNRAS* , vol. 262, pp. 627–649, June 1993.

[52] W. H. Press and P. Schechter, “Formation of Galaxies and Clusters of Galaxies by Self-Similar Gravitational Condensation,” *Ap. J.* , vol. 187, pp. 425–438, Feb. 1974.

[53] R. K. Sheth, “An excursion set model for the distribution of dark matter and dark matter haloes,” *MNRAS* , vol. 300, pp. 1057–1070, Nov. 1998.

[54] M. McQuinn, S. R. Furlanetto, L. Hernquist, O. Zahn, and M. Zaldarriaga, “The Kinetic Sunyaev-Zel’dovich Effect from Reionization,” *Ap. J.* , vol. 630, pp. 643–656, Sept. 2005.

[55] S. R. Furlanetto and S. P. Oh, “Taxing the rich: recombinations and bubble growth during reionization,” *MNRAS* , vol. 363, pp. 1031–1048, Nov. 2005.

[56] U. Seljak and M. Zaldarriaga, “A Line of Sight Approach to Cosmic Microwave Background Anisotropies,” *Astrophys. J.*, vol. 469, pp. 437–444, 1996.

[57] S. R. Furlanetto, M. McQuinn, and L. Hernquist, “Characteristic scales during reionization,” *MNRAS* , pp. 1043–+, Nov. 2005.

[58] J. R. Pritchard and S. R. Furlanetto, “Descending from on high: Lyman series cascades and spin- kinetic temperature coupling in the 21 cm line,” *Mon. Not. Roy. Astron. Soc.*, vol. 367, pp. 1057–1066, 2006.

[59] G. B. Field *Proc. IRE*, vol. 46, p. 240, 1958.

[60] A. Loeb and M. Zaldarriagga, “Measuring the Small-Scale Power Spectrum of Cosmic Density Fluctuations Through 21 cm Tomography Prior to the Epoch of Structure Formation,” *Phys. Rev. Lett. , Submitted, (astro-ph/0312134)*, 2003.

[61] P. J. E. Peebles, “Principles of physical cosmology,” *Princeton University Press*, 1994. Princeton, USA: Univ. Pr. (1993) 718 p.

[62] S. Seager, D. D. Sasselov, and D. Scott, “How exactly did the Universe become neutral?,” *Astrophys. J. Suppl.*, vol. 128, pp. 407–430, 2000.

[63] S. Furlanetto, S. P. Oh, and F. Briggs, “Cosmology at Low Frequencies: The 21 cm Transition and the High-Redshift Universe,” *Phys. Rept.*, vol. 433, pp. 181–301, 2006.

[64] S. P. Oh, “Reionization by Hard Photons. I. X-Rays from the First Star Clusters,” *Ap. J.* , vol. 553, pp. 499–512, June 2001.

[65] H. J. Grimm, M. Gilfanov, and R. Sunyaev, “High Mass X-ray Binaries as a Star Formation Rate Indicator in Distant Galaxies,” *Mon. Not. Roy. Astron. Soc.*, vol. 339, p. 793, 2003.

[66] P. Ranalli, A. Comastri, and G. Setti, “The 2-10 keV luminosity as a Star Formation Rate indicator,” *Astron. Astrophys.*, vol. 399, pp. 39–50, 2003.

[67] S. Furlanetto, “The Global 21 Centimeter Background from High Redshifts,” *astro-ph/0604040*, 2006.

[68] J. M. Shull and S. Beckwith, “Interstellar molecular hydrogen,” *Ann. Rev. Astron. Astrophys.*, vol. 20, pp. 163–190, 1982.

[69] S. A. Wouthuysen, “On the excitation mechanism of the 21-cm (radio-frequency) interstellar hydrogen emission line.,” *Astron. J.* , vol. 57, pp. 31–+, 1952.

[70] C. M. Hirata, “Wouthuysen-Field coupling strength and application to high- redshift 21 cm radiation,” *Mon. Not. Roy. Astron. Soc.*, vol. 367, pp. 259–274, 2006.

[71] J. E. Gunn and B. A. Peterson, “On the Density of Neutral Hydrogen in Intergalactic Space.,” *Ap. J.* , vol. 142, pp. 1633–1636, Nov. 1965.

[72] G. B. Field, “An Attempt to Observe Neutral Hydrogen Between the Galaxies.,” *Ap. J.* , vol. 129, pp. 525–+, May 1959.

[73] B. Ciardi and P. Madau, “Probing beyond the epoch of hydrogen reionization with 21 centimeter radiation,” *Ap. J.* , vol. 596, p. 1, 2003.

[74] J. R. Pritchard and S. R. Furlanetto, “21 cm fluctuations from inhomogeneous X-ray heating before reionization,” *astro-ph/0607234*, 2006.

[75] M. Zaldarriaga, S. R. Furlanetto, and L. Hernquist, “21 Centimeter Fluctuations from Cosmic Gas at High Redshifts,” *Ap. J.* , vol. 608, pp. 622–635, June 2004.

[76] R. Barkana and A. Loeb, “A Method for Separating the Physics from the Astrophysics of High-Redshift 21 Centimeter Fluctuations,” *Ap. J. L.*, vol. 624, pp. L65–L68, May 2005.

[77] A. Lidz *et al.*, “Higher Order Contributions to the 21 cm Power Spectrum,” *astro-ph/0610054, submitted to ApJ*, 2006.

[78] S. Bharadwaj and S. S. Ali, “The cosmic microwave background radiation fluctuations from HI perturbations prior to reionization,” *MNRAS* , vol. 352, pp. 142–146, July 2004.

[79] X. Wang and W. Hu, “Redshift space 21 cm power spectra from reionization,” *Astrophys. J.*, vol. 643, pp. 585–597, 2006.

[80] M. McQuinn, O. Zahn, M. Zaldarriaga, L. Hernquist, and S. R. Furlanetto, “Cosmological Parameter Estimation Using 21 cm Radiation from the Epoch of Reionization,” *ApJ, in press (astro-ph/0512263)*, 2005.

[81] R. Barkana and A. Loeb, “Detecting the Earliest Galaxies through Two New Sources of 21 Centimeter Fluctuations,” *Ap. J.* , vol. 626, pp. 1–11, June 2005.

[82] S. Naoz and R. Barkana, “Growth of linear perturbations before the era of the first galaxies,” *Mon. Not. Roy. Astron. Soc.*, vol. 362, pp. 1047–1053, 2005.

[83] J. D. Bowman, M. F. Morales, and J. N. Hewitt, “The sensitivity of first generation epoch of reionization observatories and their potential for differentiating theoretical power spectra,” *Astrophys. J.*, vol. 638, pp. 20–26, 2006.

[84] M. de Vos, “Lofar Phase 1 Baseline Specification,” *http://www.lofar.org/PDF/LOFAR-P1-Baseline2.0.pdf*, 2004.

[85] C. L. Carilli and S. Rawlings, “Science with the Square Kilometer Array: Motivation, Key Science Projects, Standards and Assumptions,” *astro-ph/0409274*, 2004.

[86] M. Tegmark, D. J. Eisenstein, W. Hu, and A. de Oliveira-Costa, “Foregrounds and Forecasts for the Cosmic Microwave Background,” *Ap. J.* , vol. 530, pp. 133–165, Feb. 2000.

[87] J. Silk, “Cosmic black body radiation and galaxy formation,” *Astrophys. J.*, vol. 151, pp. 459–471, 1968.

[88] A. Kosowsky, “The Atacama Cosmology Telescope,” *New Astron. Rev.*, vol. 47, pp. 939–943, 2003.

[89] J. E. Ruhl *et al.*, “The South Pole Telescope,” *astro-ph/0411122*, 2004.

[90] C. M. Hirata and U. Seljak, “Analyzing weak lensing of the cosmic microwave background using the likelihood function,” *Phys. Rev.*, vol. D67, p. 043001, 2003.

[91] A. R. Cooray, “Lensing studies with diffuse backgrounds,” *New Astron.*, vol. 9, pp. 173–187, 2004.

[92] K. Sigurdson and A. Cooray, “Cosmic 21-cm delensing of microwave background polarization and the minimum detectable energy scale of inflation,” *Phys. Rev. Lett.*, vol. 95, p. 211303, 2005.

[93] U.-L. Pen, “Gravitational Lensing of Pre-reionization Gas,” *New Astron.*, vol. 9, pp. 417–424, 2004.

[94] W. Hu, “Mapping the Dark Matter through the CMB Damping Tail,” *Astrophys. J.*, vol. 557, pp. L79–L83, 2001.

[95] W. Hu, “Angular trispectrum of the cosmic microwave background,” *Phys. Rev.*, vol. D64, p. 083005, 2001.

[96] W. Hu and T. Okamoto, “Mass Reconstruction with CMB Polarization,” *Astrophys. J.*, vol. 574, pp. 566–574, 2002.

[97] K. S. Mandel and M. Zaldarriaga, “Weak Gravitational Lensing of High-Redshift 21 cm Power Spectra,” *Astrophys. J.*, vol. 647, p. 719, 2006.

[98] R. E. Smith *et al.*, “Stable clustering, the halo model and nonlinear cosmological power spectra,” *Mon. Not. Roy. Astron. Soc.*, vol. 341, p. 1311, 2003.

[99] M. J. White, J. E. Carlstrom, and M. Dragovan, “Interferometric Observation of Cosmic Microwave Background Anisotropies,” *Astrophys. J.*, vol. 514, p. 12, 1999.

[100] M. F. Morales and J. Hewitt, “Toward Epoch of Re-ionization Measurements with Wide-Field LOFAR Observations,” *Ap. J. , Submitted, (astro-ph/0312437)*, 2003.

[101] U. L. Pen, X. P. Wu, and J. Peterson, “Forecast for Epoch-of-Reionization as viewable by the PrimevAl Structure Telescope (PAST),” *Submitted to CJAA (astro-ph/0404083)*, 2005.

[102] P. Zhang and U.-L. Pen, “Mapping dark matter with cosmic magnification,” *Phys. Rev. Lett.*, vol. 95, p. 241302, 2005.

[103] W. Hu, “Dark Synergy: Gravitational Lensing and the CMB,” *Phys. Rev.*, vol. D65, p. 023003, 2002.

[104] A. Amblard, C. Vale, and M. J. White, “Weak Lensing of the CMB by Large-Scale Structure,” *New Astron.*, vol. 9, pp. 687–704, 2004.

[105] R. A. Sunyaev and Y. B. Zeldovich, “Microwave background radiation as a probe of the contemporary structure and history of the universe,” *Ann. Rev. Astron. Astrophys.*, vol. 18, pp. 537–560, 1980.

[106] U. Seljak and C. M. Hirata, “Gravitational lensing as a contaminant of the gravity wave signal in CMB,” *Phys. Rev.*, vol. D69, p. 043005, 2004.

[107] L. Knox, “Cosmic microwave background anisotropy observing strategy assessment,” *astro-ph/9606066*, 1996.

[108] M. F. Morales, “Power Spectrum Sensitivity and the Design of Epoch of Reionization Observatories,” *Ap. J.* , vol. 619, pp. 678–683, Feb. 2005.

[109] D. Babich and A. Loeb, “Polarization of 21cm Radiation from the Epoch of Reionization,” *submitted to MNRAS (astro-ph/0505358)*, 2005.

[110] A. C. S. Readhead *et al.*, “Extended Mosaic Observations with the Cosmic Background Imager,” *Astrophys. J.*, vol. 609, pp. 498–512, 2004.

[111] W. L. Holzapfel, J. E. Carlstrom, L. Grego, G. Holder, M. Joy, and E. D. Reese, “Limits on Arcminute-Scale Cosmic Microwave Background Anisotropy at 28.5 GHZ,” *Ap. J.* , vol. 539, pp. 57–66, Aug. 2000.

[112] M. Bartelmann and P. Schneider, “Weak gravitational lensing,” *Phys. Rept.*, vol. 340, pp. 291–472, 2001.

[113] R. B. Metcalf and J. Silk, “On Breaking Cosmic Degeneracy,” *Ap. J. L.*, vol. 492, pp. L1+, Jan. 1998.

[114] R. Stompor and G. Efstathiou, “Gravitational lensing of cosmic microwave background anisotropies and cosmological parameter estimation,” *Mon. Not. Roy. Astron. Soc.*, vol. 302, p. 735, 1999.

[115] M. Zaldarriaga and U. Seljak, “Reconstructing projected matter density from cosmic microwave background,” *Phys. Rev.*, vol. D59, p. 123507, 1999.

[116] L. V. van Waerbeke, F. Bernardeau, and K. Benabed, “Lensing effect on the relative orientation between the Cosmic Microwave Background ellipticities and the distant galaxies,” *astro-ph/9910366*, 1999.

[117] M. Kaplinghat, L. Knox, and Y.-S. Song, “Determining neutrino mass from the CMB alone,” *Phys. Rev. Lett.*, vol. 91, p. 241301, 2003.

[118] Y. B. Zeldovich and R. A. Sunyaev, “The interaction of matter and radiation in a hot-model universe,” *Astrophys. Space Sci.*, vol. 4, p. 301, 1969.

[119] M. Birkinshaw, “The Sunyaev-Zel’dovich Effect,” *Phys. Rept.*, vol. 310, pp. 97–195, 1999.

[120] J. E. Carlstrom *et al.*, “Imaging the Sunyaev-Zel’dovich Effect,” *astro-ph/9905255*, 1999.

[121] M. Tegmark *et al.*, “Cosmological parameters from SDSS and WMAP,” *Phys. Rev.*, vol. D69, p. 103501, 2004.

[122] L. Knox, R. Scoccimarro, and S. Dodelson, “The Impact of Inhomogeneous Reionization on Cosmic Microwave Background Anisotropy,” *Phys. Rev. Lett.*, vol. 81, pp. 2004–2007, 1998.

[123] M. G. Santos *et al.*, “Small-Scale Cosmic Microwave Background Temperature and Polarization Anisotropies Due to Patchy Reionization,” *Ap. J.* , vol. 598, pp. 756–766, Dec. 2003.

[124] A. Gruzinov and W. Hu, “Secondary CMB anisotropies in a universe reionized in patches,” *Astrophys. J.*, vol. 508, pp. 435–439, 1998.

[125] V. Springel, N. Yoshida, and S. D. M. White, “GADGET: A code for collisionless and gasdynamical cosmological simulations,” *New Astron.*, vol. 6, p. 79, 2001.

[126] V. Springel and L. Hernquist, “Cosmological SPH simulations: A hybrid multi-phase model for star formation,” *Mon. Not. Roy. Astron. Soc.*, vol. 339, p. 289, 2003.

[127] V. Springel and L. Hernquist, “Cosmological SPH simulations: A hybrid multi-phase model for star formation,” *Mon. Not. Roy. Astron. Soc.*, vol. 339, p. 289, 2003.

[128] V. Springel, M. White, and L. Hernquist, “Hydrodynamic Simulations of the Sunyaev-Zeldovich Effect(s),” *Ap. J.* , vol. 549, pp. 681–687, Mar. 2001.

[129] J. P. Ostriker and E. T. Vishniac, “Generation of microwave background fluctuations from nonlinear perturbations at the ERA of galaxy formation,” *Ap. J. L.*, vol. 306, pp. L51–L54, July 1986.

[130] A. Lewis, A. Challinor, and A. Lasenby, “Efficient Computation of CMB anisotropies in closed FRW models,” *Astrophys. J.*, vol. 538, pp. 473–476, 2000.

[131] D. Schaerer, “The transition from Population III to normal galaxies: Ly-a and HeII 1640 emission and the ionising properties of high redshift starburst galaxies,” *Astron. Astrophys.*, vol. 397, pp. 527–538, 2003.

[132] V. Bromm, P. S. Coppi, and R. B. Larson, “From Darkness to Light: The First Stars in the Universe,” in *Lighthouses of the Universe: The Most Luminous Celestial Objects and Their Use for Cosmology: Proceedings of the MPA/ESO/MPE/USM Joint Astronomy Conference Held in Garching, Germany, 6-10 August 2001, ESO ASTROPHYSICS SYMPOSIA. ISBN 3-540-43769-X. Edited by M. Gilfanov, R. Sunyaev, and E. Churazov. Springer-Verlag, 2002, p. 316* (M. Gilfanov, R. Sunyeav, and E. Churazov, eds.), pp. 316–+, 2002.

[133] R. S. Somerville and M. Livio, “Star Formation at the Twilight of the Dark Ages: Which Stars Reionized the Universe?,” *Astrophys. J.*, vol. 593, pp. 611–615, 2003.

[134] J. Mackey, V. Bromm, and L. Hernquist, “Three Epochs of Star Formation in the High Redshift Universe,” *Astrophys. J.*, vol. 586, pp. 1–11, 2003.

[135] N. Yoshida, V. Bromm, and L. Hernquist, “The Era of Massive Population III Stars: Cosmological Implications and Self-Termination,” *Astrophys. J.*, vol. 605, pp. 579–590, 2004.

[136] M. Tegmark, “Cmb mapping experiments: a designer’s guide,” *Phys. Rev.*, vol. D56, pp. 4514–4529, 1997.

[137] K. M. Huffenberger and U. Seljak, “Prospects for ACT: simulations, power spectrum, and non- Gaussian analysis,” *New Astron.*, vol. 10, pp. 491–515, 2005.

[138] W. Hu, “Reionization Revisited: Secondary CMB Anisotropies and Polarization,” *Astrophys. J.*, vol. 529, p. 12, 2000.

[139] R. A. Sunyaev and Y. B. Zeldovich, “The interaction of matter and radiation in the hot model of the universe,” *Astrophys. Space Sci.*, vol. 7, pp. 20–30, 1970.

[140] G. P. Holder and J. E. Carlstrom, “The Sunyaev-Zeldovich Effect as Microwave Foreground and Probe of Cosmology,” *astro-ph/9904220*, 1999.

[141] P.-J. Zhang and U.-L. Pen, “Deprojecting Sunyaev-Zeldovich statistics,” *astro-ph/0007462*, 2000.

[142] U. Seljak, J. Burwell, and U.-L. Pen, “Sunyaev-Zeldovich effect from hydrodynamical simulations: Maps and low order statistics,” *Phys. Rev.*, vol. D63, p. 063001, 2001.

[143] A. Cooray, W. Hu, and M. Tegmark, “Large-Scale Sunyaev-Zel’dovich Effect: Measuring Statistical Properties with Multifrequency Maps,” *Astrophys. J.*, vol. 540, pp. 1–13, 2000.

[144] E. Komatsu and U. Seljak, “The Sunyaev-Zel’dovich angular power spectrum as a probe of cosmological parameters,” *Mon. Not. Roy. Astron. Soc.*, vol. 336, p. 1256, 2002.

[145] Z. Haiman, T. Abel, and P. Madau, "Photon Consumption in Minihalos during Cosmological Reionization," *Ap. J.* , vol. 551, pp. 599–607, Apr. 2001.

[146] R. Barkana and A. Loeb, "Effective Screening Due to Minihalos during the Epoch of Reionization," *Ap. J.* , vol. 578, pp. 1–11, Oct. 2002.

[147] P. R. Shapiro, I. T. Iliev, and A. C. Raga, "Photoevaporation of cosmological minihaloes during reionization," *MNRAS* , vol. 348, pp. 753–782, Mar. 2004.

[148] A. Lewis, "Observational constraints and cosmological parameters," *astro-ph/0603753*, 2006.

[149] U. Seljak, A. Slosar, and P. McDonald, "Cosmological parameters from combining the Lyman-alpha forest with CMB, galaxy clustering and SN constraints," *JCAP*, vol. 0610, p. 014, 2006.

[150] Z. Haiman, M. J. Rees, and A. Loeb, "Destruction of Molecular Hydrogen during Cosmological Reionization," *Ap. J.* , vol. 476, pp. 458–+, Feb. 1997.

[151] V. Springel, "The cosmological simulation code GADGET-2," *MNRAS* , vol. 364, p. 1105, 2005.

[152] D. J. Eisenstein and W. Hu, "Baryonic Features in the Matter Transfer Function," *Ap. J.* , vol. 496, pp. 605–+, Mar. 1998.

[153] M. Davis, G. Efstathiou, C. S. Frenk, and S. D. M. White, "The evolution of large-scale structure in a universe dominated by cold dark matter," *Astrophys. J.*, vol. 292, pp. 371–394, 1985.

[154] R. K. Sheth and G. Lemson, "The forest of merger history trees associated with the formation of dark matter haloes," *MNRAS* , vol. 305, pp. 946–956, May 1999.

[155] D. Reed *et al.*, "Evolution of the Density Profiles of Dark Matter Haloes," *Mon. Not. Roy. Astron. Soc.*, vol. 357, pp. 82–96, 2005.

[156] K. Heitmann, Z. Lukić, S. Habib, and P. M. Ricker, "Capturing Halos at High Redshifts," *Ap. J. L.*, vol. 642, pp. L85–L88, May 2006.

[157] A. Loeb, R. Barkana, and L. Hernquist, "Was the Universe Reionized at Redshift 10?," *Astrophys. J.*, vol. 620, pp. 553–558, 2005.

[158] T. Abel and B. D. Wandelt, “Adaptive ray tracing for radiative transfer around point sources,” *MNRAS* , vol. 330, pp. L53–L56, Mar. 2002.

[159] A. Sokasian, T. Abel, and L. E. Hernquist, “Simulating reionization in numerical cosmology,” *New Astronomy*, vol. 6, pp. 359–379, Sept. 2001.

[160] T. Abel, M. L. Norman, and P. Madau, “Photon-conserving Radiative Transfer around Point Sources in Multidimensional Numerical Cosmology,” *Ap. J.* , vol. 523, pp. 66–71, Sept. 1999.

[161] G. Mellema, I. Iliev, M. Alvarez, and P. Shapiro, “C2-ray: A new method for photon-conserving transport of ionizing radiation,” *astro-ph/0508416*, 2005.

[162] J. D. Cohn and T.-C. Chang, “Source Mergers and Bubble Growth During Reionization,” *astro-ph/0603753*, 2006.

[163] O. Zahn, M. Zaldarriaga, L. Hernquist, and M. McQuinn, “The influence of non-uniform reionization on the CMB,” *Astrophys. J.*, vol. 630, pp. 657–666, 2005.

[164] X. Chen and J. Miralda-Escudé, “The Spin-Kinetic Temperature Coupling and the Heating Rate due to Lyα Scattering before Reionization: Predictions for 21 Centimeter Emission and Absorption,” *Ap. J.* , vol. 602, pp. 1–11, Feb. 2004.

[165] N. Kaiser, “Clustering in real space and in redshift space,” *MNRAS* , vol. 227, pp. 1–21, July 1987.

[166] V. Springel and L. Hernquist, “The history of star formation in a Λ cold dark matter universe,” *MNRAS* , vol. 339, pp. 312–334, Feb. 2003.

[167] R. H. Kramer, Z. Haiman, and S. P. Oh, “Feedback from Clustered Sources During Reionization,” *astro-ph/0604218*, 2006.

[168] S. R. Furlanetto, M. Zaldarriaga, and L. Hernquist, “Statistical Probes of Reionization with 21 Centimeter Tomography,” *Ap. J.* , vol. 613, pp. 16–22, Sept. 2004.